

Colloidal Interfaces in Confinement

Elizabeth Jamie

Christ Church

University of Oxford

Supervisor: Dr Dirk Aarts

A thesis submitted for the degree of

Doctor of Philosophy

Hilary Term 2011

Abstract

A fluid-fluid demixing colloid-polymer system provides us with an opportunity to study interfacial phenomena that cannot be observed in molecular systems due to unfavourable length and timescales. We develop such a system compatible with cells of varying dimensions, allowing us to investigate confined interfacial behaviour in real space using Confocal Scanning Laser Microscopy.

The degree to which a system is affected by the sedimentation-diffusion gradient is dependent on the ratio of the suspension height to the gravitational length of the colloids. We illustrate that we may control the distance of our interface to the critical point by altering the suspension height, determining the importance of the gravitational field. Furthermore, the timescale on which the sedimentation- diffusion gradient is established is considerably longer than that of initial fluid-fluid demixing. We show that after the formation of the macroscopic interface, the system passes through a series of local mechanical equilibria on the way to achieving full equilibrium. Should the system be of sufficient height, it will pass through the gas-liquid critical point opening up new ways to study critical phenomena.

The time and length scales of the fluid-fluid demixing of our system may be manipulated by altering the density and viscosity of our solvent. We exploit a slowed phase separation process to study the interplay between demixing and wetting phenomena of systems in the vicinity of a single wetting surface, and confined between two parallel plates. We demonstrate that the presence of a surface strongly affects the morphology of phase separation. The growth of the wetting layer is determined by the demixing regime of the system, and may be accelerated by hydrodynamics. The additional restriction by a second surface limits the lengthscale of coarsening domains and may further alter the mechanism of wetting layer growth.

Declaration

This thesis is submitted for the degree of Doctor of Philosophy in Physical and Theoretical Chemistry at the University of Oxford. No part of this thesis has been accepted or is currently being submitted for any degree, diploma, certificate or other qualification in this University or elsewhere. This thesis is wholly my own work, except where indicated.

Contents

Abstract **i**

Declaration **ii**

1 Introduction **1**

1.1 Colloidal systems 2

1.2 Phase behaviour 3

1.3 Interfacial behaviour 4

1.4 Scope of thesis 6

2 Systems, techniques and analysis **8**

2.1 Introduction 8

2.2 Experimental technique 10

2.2.1 Confocal microscopy 10

2.2.2 Fabrication of confinement cells 12

2.3 System details 13

2.4 Thermal capillary waves of PMMA-xanthan-water system 16

2.5 Conclusion 21

3 Probing the critical behaviour of colloidal interfaces by gravity. **22**

3.1 Introduction 22

3.2 Density functional theory 24

3.3 Experimental system and method 27

3.4 Results and discussion 29

3.5 Conclusion 33

4 Sedimentation-diffusion dynamics in colloid-polymer mixtures 35

4.1 Introduction 35

4.2 Theoretical background 36

4.3 Experimental system and method 39

4.4 Results and discussion 40

4.5 Conclusion 48

5 Tuning the demixing of colloid-polymer systems through the dispersing solvent 50

5.1 Introduction 50

5.2 Theory 52

5.3 Experimental system and method 54

5.4 Results and discussion 55

5.5 Conclusion 61

6 Surface effects on the demixing of colloid-polymer systems 64

6.1 Introduction 64

6.2 Background 65

6.3 Experimental system and image analysis 69

6.3.1 Sample preparation 69

6.3.2 Image analysis 70

6.4 Results 72

6.4.1 Bulk phase separation 72

6.4.2 Surface directed spinodal decomposition 73

6.5 Discussion 79

6.6 Conclusion 83

7 Demixing of colloid-polymer systems confined between two parallel plates 85

7.1 Introduction 85

7.2 Background 87

7.3 Experimental details and analysis 92
7.3.1 Experimental details 92
7.3.2 Analysis 94
7.4 Bulk phase separations 95
7.5 Confined systems 97
7.5.1 Metastable systems 97
7.5.2 Spinodal decomposition 105
7.6 Wetting layer growth 115
7.7 Conclusion 116

Overview **120**

Bibliography **123**

List of publications **134**

Acknowledgments **136**

Chapter 1

Introduction

> 'Thus, as we might have supposed, an emulsion is actually a miniature ponderable atmosphere; or, rather, it is an atmosphere of colossal molecules, which are actually visible.' Perrin, 1916 [1]

The use of colloidal systems as models to investigate the phase behaviour of atomic and molecular systems has brought colloid science to the forefront of statistical mechanical research [2]. Colloidal systems have larger lengthscales and slower timescales than their molecular equivalent, allowing the tracking of individual particles [3] in addition to the observation of macroscopic phenomena [4]. These model systems have already proved extremely useful for example in the study of interface fluctuations [5] and liquid-gas demixing [6,7], where the capillary waves and domain structures are too small and quickly changing for observation in molecular systems. They have also been utilised in the study of crystalline [8,9], glass [10], and gel states [11] and their associated phase behaviour [12–15]. In this thesis we shall only explore fluid-fluid systems and liquid-gas phase behaviour. There are many other examples of molecular phase phenomena that can be studied using a suitable colloidal analogue, for example wetting [16–18] and capillary condensation [19,20]. The colloidal model also offers an opportunity to study fluids in confined geometries [21], where preparation of suitable confining cells for small molecules is extremely difficult due to variations in wall potential caused by even atomic corrugations [22]. Thus, as was noted by Perrin, a colloidal system offers the opportunity to explore the statistical mechanics of fluids using an alternative visible system.

1.1 Colloidal systems

In 1827 Robert Brown observed the erratic movements of pollen grains in water - the consequence of random collisions of water molecules with the pollen grain. This phenomenon became known as Brownian motion, where we are able to observe the molecular nature of the solvent through the random motion of the colloidal particles [23, 24]. This movement can be compared to the thermal motion of molecules, but only the Brownian motion of the colloids is visible using light microscopy techniques due to the lengthscales involved. This behaviour sets the size range for a colloidal particle - it must be small enough that it still displays a significant amount of Brownian motion, but sufficiently large that many of the solvent molecules interact with the colloidal particle simultaneously and the colloid-solvent interaction may be expressed as a macroscopic average [25, 26]. In practice, colloids are generally specified as particles with at least one dimension in the range of around 1 nm to 1 μm [26].

A colloid exhibiting Brownian motion will constantly move with a random zigzagging motion, which will cause diffusion as the particles explore their entire container. Einstein linked the mobility of Brownian particles to a diffusion coefficient [27, 28]:

$$D = \frac{k_B T}{\xi_f} = \frac{k_B T}{6\pi\eta r}, \tag{1.1}$$

where k_B is Boltzmann's constant, T is the temperature, and ξ_f is the friction factor. The friction factor is determined by the Stokes relation for spherical particles of radius r in a solvent of viscosity η. The diffusion coefficient of a colloidal particle will be much smaller than that of a molecule due to its large size. The slower dynamics of the colloidal particle, in addition to their size being comparable to the wavelength of visible light makes it easy to observe them using optical microscopy, and ideal for experiment. This was utilised in the celebrated work of Perrin to determine Avogadro's constant, and his exploration of the sedimentation gradient.

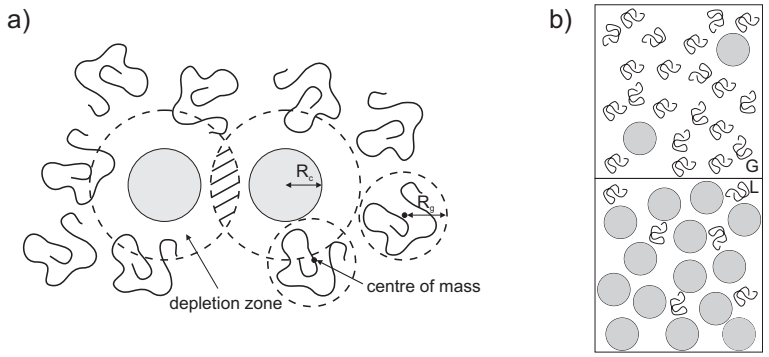


Figure 1.1: (a) Schematic diagram showing colloidal particles and the depletion zone. (b) The phase separated colloid-polymer system. The upper phase is the colloidal gas, the lower phase the colloidal liquid.

1.2 Phase behaviour

The phase behaviour of a system is determined by the interactions between its constituent particles, therefore for the colloidal system to be a useful model, the interaction between two colloids must be comparable to that in a molecular system. The interaction potential between molecules in a simple monatomic liquid separated by distance r can be described by the Lennard-Jones potential:

$$V_{LJ} = 4\epsilon \left[\left(\frac{\delta}{r} \right)^{12} - \left(\frac{\delta}{r} \right)^{6} \right], \tag{1.2}$$

where ϵ is the depth of the potential well, and δ is the separation at which $V_{LJ} = 0$. The first term represents a short range repulsion due to the overlap of electronic orbitals, and the second a longer range attraction due to dispersion interactions [29]. The interaction between colloidal particles can be described by the Derjaguin, Landau, Verwey and Overbeek (DLVO) potential [30,31]. The long range attraction is also due to van der Waals interactions, whereas at shorter lengthscales, there is a repulsion due to overlapping electrical double layers [26]. To achieve a fluid-fluid phase separation the depth of the attraction should be of the order of the thermal energy k_BT and the interaction range should be around the colloidal diameter R_c. This criterion can be difficult to achieve in experiments, and alterations to the potential are difficult, thus we look for an alternative method of controlling the potential between the colloids in our system.

The addition of a third component to our colloidal dispersion offers us a flexible, tunable method of controlling the interactions between our colloids. To do this, we add polymer coils with radius of gyration R_g to our colloids (radius R_c). Surrounding the surface of each of the colloids is an area from which centres of mass of the polymer coils will be entropically excluded, known as the depletion zone. If two colloids move close together and these zones overlap then there is an osmotic imbalance creating an attraction between the colloids (figure 1.1 (a)). This attraction is known as the depletion interaction and was first illustrated by Asakura and Oosawa [32] and later by Vrij [33]. Should the concentrations of each component be sufficient we can induce a phase separation into a colloid-rich polymer-poor 'liquid' phase and a polymer-rich colloid-poor 'gas' phase (figure 1.1 (b)), comparable to the gas-liquid phase separation found in molecular liquids [4].

The phase behaviour of such a system has been explored in experiment, simulation and theory [8, 34–37] and it is found that the phase diagram is dependent on the polymer size ratio $q = R_g/R_c$. In this work we shall only consider the separation into a colloidal liquid-gas system, however dependent on the value of q, colloidal crystal [38] and more exotic phases are possible [39,40]. The work of Lekkerkerker *et al.* [38,41] explored the consequences of polymer partitioning between the phases and a treatment known as 'free volume theory' has been established. This has led to an accurate prediction of phase diagrams in some cases [8,42,43], however the non-ideality of polymers in real experiments remains challenging (see [44] for a review).

1.3 Interfacial behaviour

Should we allow a phase separating colloid-polymer system to demix and equilibrate into two phases, a sharp interface will be formed. For a molecular system the tension associated with this interface will scale as [45]:

$$\gamma \sim \frac{\epsilon}{d^2}, \tag{1.3}$$

where ϵ is the depth of the interaction potential and d is the diameter of the molecules. When we consider our colloid-polymer system, the depth of the potential well is around

k_BT and the particle diameter of the order 10^{-7} m. This results in an 'ultra-low' interfacial tension on the order of 10^{-8} Nm^{-1} for the colloid polymer system, which is several orders of magnitude smaller than that of the air-water interface, which is of the order of 10^{-1} Nm^{-1}. This has the consequence of altering the time and lengthscales of interfacial fluctuations in several ways.

As predicted by Smoluchowski [46], the surface of an interface shall be rough as thermal motion leads to statistical fluctuations of the local interface position. These ripples are known as capillary waves. The amplitude of these fluctuations, the thermal roughness, is given by [47]:

$$L_T = \sqrt{\frac{k_BT}{\gamma}}. \tag{1.4}$$

By moving to a system with an ultralow interfacial tension, the size of the interfacial fluctuations becomes of the order of microns, thus we are able to observe these using optical microscopy [5]. The analysis of these waves allows us to characterise our colloid-polymer system [5, 47] obtaining useful interfacial properties, such as a numerical value for the interfacial tension, the characteristic parallel in plane lengthscale of the fluctuations, the capillary length,

$$L_c = \sqrt{\frac{\gamma}{g\Delta\rho}}, \tag{1.5}$$

and the typical decay time of the waves, the capillary time:

$$\tau = \frac{L_c\eta}{\gamma}, \tag{1.6}$$

where g is the Earth's acceleration due to gravity, $\Delta\rho$ is the density difference between the two phases, and η is the sum of the viscosity of each phase.

The ultra-low interfacial tension in our colloid polymer system means that its capillary length is significantly reduced in comparison to its molecular counterpart. As well as characterising the lengthscale of interfacial fluctuations, the capillary length determines the radius of curvature of the meniscus when such an interface is in contact with a wall. It is also crucial in determining the lengthscales of the crossovers between regimes in demixing. The capillary time is significantly increased, which allows us to follow the fluctuations of the interface whilst they still show correlation.

The ultra-low interfacial tension additionally has the effect of lowering the Reynolds number (Re) in the system, meaning that inertial forces are insignificant. This number quantifies the relative importance of the inertial and viscous forces, and is given by [48]:

$$Re = \frac{\text{Inertial Forces}}{\text{Viscous Forces}} = \frac{Lu_c\rho}{\eta} = \frac{\gamma L\rho}{\eta^2}, \tag{1.7}$$

where L is a lengthscale, η the viscosity, and the speed at which the interface is moving is proportional to the capillary velocity $u_c \equiv \gamma/\eta$. The dynamics of our system are dominated by diffusion and viscous hydrodynamics, which has important consequences when we consider the evolution of phase separation morphologies later in this work.

1.4 Scope of thesis

In this thesis we shall study interfacial phenomena in a colloid-polymer system subjected to varying confining geometries and external fields. Creating a model system with suitable interfacial properties to explore such effects can be a challenging process as there are many different criteria to be taken into account. In chapter 2 we shall detail the colloid-polymer mixture studied in this work, and explain the technique of confocal microscopy which we use to obtain real space images of the system. We outline the process to fabricate microfluidic confinement cells, and explain the necessity to create a new colloid-polymer system in an aqueous rather than organic solvent. We shall investigate the phase behaviour of this new system and illustrate that the thermal fluctuations of its interface can be analysed using capillary wave theory.

In chapters 3 and 4 we shall explore the effect of the sedimentation-diffusion gradient on our fluid-fluid interface. The significance of the sedimentation gradient in a colloidal suspension is dependent on the ratio of the suspension height to the gravitational length of the colloids. In chapter 3 we shall demonstrate that the gravitational field may be used to control the distance of the interface to the critical point. Increasing the height of a phase separated colloid-polymer suspension leads to a systematic roughening of the interface as if approaching criticality. In chapter 4 we shall explore the path the system takes to achieve full sedimentation-diffusion equilibrium after the macroscopic interface is formed.

In the following three chapters we shall study the demixing of a colloid-polymer system. Although the phase separation dynamics of colloidal systems are considerably slower than in their molecular counterpart, early-time coarsening regimes may still progress in a matter of seconds. In chapter 5 we shall illustrate that we may slow down the demixing of a colloid-polymer system by increasing the viscosity of the solvent. We shall also demonstrate that by density matching the colloids and the solvent, we can increase the capillary length in the system, and postpone the gravity driven regime. In chapter 6 we exploit our decelerated demixing process to study the phase separation of such a system in the vicinity of a solid wall which is preferentially wet one of the phases. We shall investigate the alteration to the phase separation morphology caused by the competition between the wetting and demixing processes, and consider the rate of growth of the wetting layer that forms upon this surface. In chapter 7 we shall provide a similar treatment for the more complex case of a mixture phase separating between two parallel plates. We shall conclude with an overview of our findings.

Chapter 2

Systems, techniques and analysis

ABSTRACT

In this chapter we explain how confocal microscopy can be used as a powerful technique to study the behaviour of colloid-polymer systems, by creating real space images in two and three dimensions. We also detail how to fabricate PDMS microfluidic cells of suitable dimension to confine such systems, and explore their wetting, demixing and interfacial phenomena. Previous experimental work on colloid-polymer mixtures has generally been performed on systems in decalin or other organic solvents, and although there are well characterised systems with excellent optical properties available, they are incompatible with the microfluidic confinement cells. We therefore detail the development of a new system based in a water solvent. We investigate its phase behaviour and illustrate how to obtain interfacial parameters by studying the capillary waves at the fluid-fluid interface. Finally we shall demonstrate that the new colloid-polymer system is compatible with microfluidics.

2.1 Introduction

Within this thesis we aim to study the interfacial behaviour of colloid-polymer systems. By staining our colloids with fluorescent dye we are able to directly observe our system using confocal microscopy. The beauty of the colloid-polymer model is that we are able to tune the interactions between colloidal particles to construct a system with the desired interfacial

properties. However there are many factors to consider in finding a good colloid-polymer system, and meeting these criteria is not necessarily a simple task.

To begin, both our colloidal and polymer dispersions must separately be stable in the same solvent. As the interaction between the colloids is governed by the depletion interaction, when we mix our stock dispersions together the polymers must not adsorb on the surface of the colloid. The strength of the depletion interaction is dependent on the value of $q = R_g/R_c$, and to drive a fluid-fluid phase separation as we wish to study here we require a polymer to colloid size ratio of at least 1/3 [38]. We screen the van der Waals attractions between the colloids by matching the refractive indices of the colloids and the solvent [49], which also minimises the unwanted scattering of light as it passes through the sample. The densities of the colloids and the solvent should also be reasonably well matched to ensure that sedimentation effects are not too prominent, and the chemical potential should not be significantly be changed by gravity over a distance of one particle diameter.

Here we focus on the study of the thermal fluctuations of our interface. To ensure these capillary waves are resolvable by our microscope, the thermal roughness L_T (eqn. (1.4)) of the fluctuations must be at least 0.2 μm. This requires that the interfacial tension in the system is of the order of 10^{-7} Nm^{-1}. The interfacial tension scales with the inverse square of the particle diameter (eqn. (1.3)), thus the colloidal diameter is also set to around 0.2 μm. To study our interfaces in a confined geometry we must also ensure that neither our colloids nor polymers stick to the walls of our confining cell.

Previous experimental work on colloid-polymer mixtures has been performed on systems in organic solvents, for example a system of Poly(methyl methacrylate) (PMMA) colloids and polystyrene polymer dispersed in decalin has proved extremely useful [8, 43, 50–52], and has been used to study interfacial fluctuations and demixing in the bulk [5,7]. To study these phenomena in confinement we fabricated small microfluidic channels in poly(dimethylsiloxane) (PDMS) elastomer [53] using soft lithography. Unfortunately the system in a decalin solvent is incompatible with these devices, as organic solvents flow through the PDMS. It is possible to make confinement cells using other methods [54, 55], however the PDMS cells are extremely cheap and their manufacture simple for a variety of geometries. Therefore we developed a new colloid-polymer system dispersed in a water solvent [56, 57], which is

compatible with these devices.

We structure this chapter as follows. To begin we shall introduce the technique of confocal microscopy, and explain the method to fabricate the PDMS confinement cells. We will then detail the development of the colloid polymer system used in this thesis, a new system based in water. We will explore the phase behaviour of our novel system, and observe its fluid-fluid phase separation. We study the interfacial fluctuations of the macroscopic interface and take this opportunity to introduce the use of capillary wave analysis to determine interfacial properties.

2.2 Experimental technique

2.2.1 Confocal microscopy

Optical microscopy is a commonly used technique to provide real space images of samples where the specimen size is of the order of the wavelength of visible light. The imaging of an optically dense sample such as a colloidal suspension can be made difficult as light is scattered by multiple particles as it passes through the suspension, causing the image to blur. Confocal microscopy, a technique first pioneered by Marvin Minsky in the 1950s whilst studying nerve cells at Harvard University [58], offers improved contrast and resolution over transmission light microscopy. In figure 2.1 we see a schematic diagram of the optics of the confocal microscope [59]. Light from a point source, of appropriate wavelength to excite the fluorescent sample, passes through the beam splitter and lens and is directed onto the sample in the focal plane. The light from that spot on the sample of the emitted wavelength then passes through the lens and is directed to the photomultiplier. The pinhole in front of the detector prevents any light from out of the plane of focus being detected. The laser scans across the focal plane and allowing us to build up a complete 2 dimensional image. We can construct an image in 3 dimensions by also scanning different focal depths [60].

The quality of the image is determined by its contrast and resolution [61]. Similar to optical microscopy, resolution is limited by the diffraction of light. When a point source illuminates a point on the sample, it is slightly blurred, and appears as an Airy disk, the size of which is determined by the wavelength of the incident light and the numerical aperture of

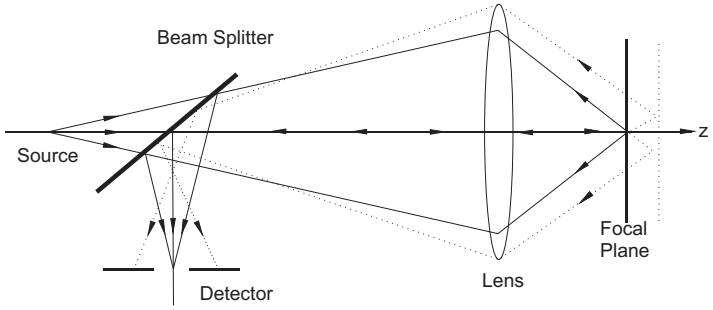


Figure 2.1: Schematic diagram of the optics of a confocal microscope. [59]

the lens. The Rayleigh criterion sets the resolution of the microscope and states that for two points to be resolved, they must be separated by at least the radius of one Airy disk [62]. For the optical setup of most commercially available microscopes the maximum resolution is around 200 nm [63]. The contrast represents the difference in intensity between the Airy disk peaks that we need to differentiate - if this is too small, then we shall be unable to distinguish the two peaks even if they are sufficiently far apart. If we introduce noise as is present in real images, this shall limit our ability to use all of the available resolution [64]. We can reduce the effects of noise by firstly ensuring that there is a sufficient illumination level initially, and then ensuring the efficiency of the optics by removing the unwanted background light. With the use of fluorescence microscopy, the light traveling from our image is of a shifted frequency to the incident light, therefore we can improve the contrast of our image by removing background light of the incorrect wavelength using filters [65].

To study the dynamic process of phase separation and the surface of a fluctuating interface, our ability to observe our samples shall also be affected by the scanning speed of the microscope. Most commonly, internal mirrors mounted upon a galvanometer are used to scan the laser back and forth over the sample [61], although faster scanning and therefore faster imaging may be obtained using moving pinhole scanning techniques such as the Nipkow spinning disk [63].

Confocal microscopy has become established as a popular method to study the structure of colloidal systems in real space, see for example the topical reviews [61,63]. To explore the behavior of our colloid-polymer systems we use a Zeiss Exciter LSM 5 Confocal Scanning Laser Microscope (CSLM). Our instrument was placed on a rolling table allowing the samples

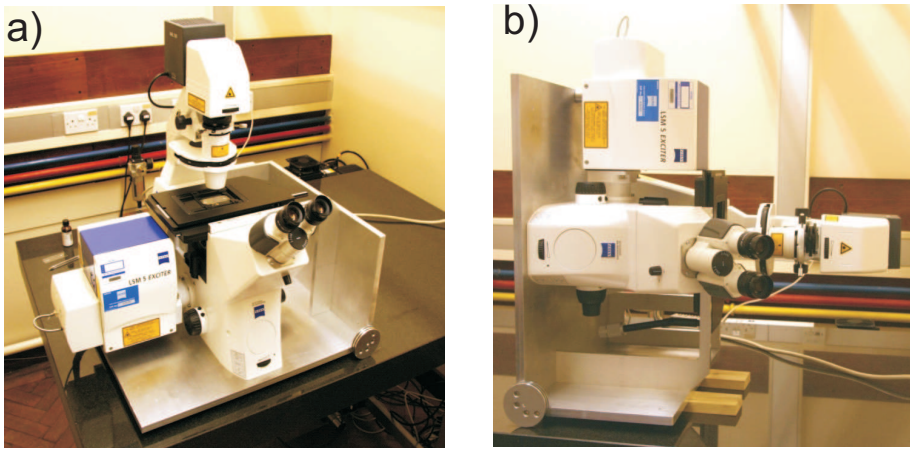


Figure 2.2: Zeiss Confocal Microscope in the position to view the sample in the plane (a) perpendicular and (b) parallel to gravity.

to be viewed in the plane parallel or perpendicular to gravity (figure 2.2).

2.2.2 Fabrication of confinement cells

In the chapters which follow, a variety of setups have been used to hold our samples whilst they are imaged with the confocal microscope, e.g. glass capillaries, Helma cuvettes, and home made devices constructed using partially cut vials and glass slides. To confine our samples to smaller dimensions or in more exotic shapes, we use soft lithography to create small microfluidic channels in PDMS elastomer [53, 66] which are sealed with a glass microscope slide. This is an inexpensive, simple and flexible technique to produce a variety of channel patterns with dimensions on the scale of microns [67].

A schematic diagram of the process used to fabricate PDMS channels can be seen in figure 2.3. First we use photolithography to construct a raised pattern of SU-8 photoresist upon a silicon wafer. SU-8 of the desired thickness is spincoated onto the wafer, followed by a baking step. The wafer is irradiated by UV light through a photomask to polymerise the SU-8 in the desired pattern. After a second baking step, the excess unpolymerised SU-8 is removed with a developing solvent, and the construction of the wafer is completed with a final hard baking step. The exact baking, UV irradiation and development times are dependent on the thickness and dimensions of the SU-8 pattern [66, 68]. The wafer mould is used as an

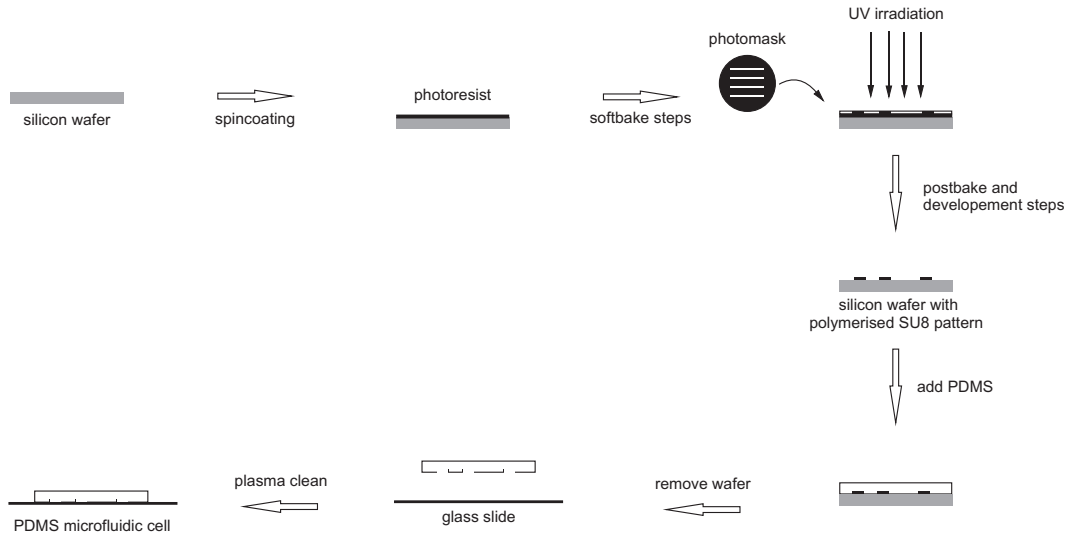


Figure 2.3: Schematic diagram of the manufacture of a microfluidic cell.

imprint for the PDMS elastomer, creating a polymer slab with the channel design indented. Holes can be made in the elastomer to allow the cell to be filled by a needle or tubing, or alternatively the channels can be cut so they remain open and may be filled by capillary action. Finally the cell is sealed with a glass slide by treating both the surfaces of the PDMS and glass with oxygen plasma, allowing them to be permanently bonded together. This enables us to confine our colloid-polymer system to the desired dimensions, and view its behaviour through the glass window.

2.3 System details

We developed a new aqueous system consisting of PMMA colloids and xanthan polymer dispersed in a water solvent. The fluorescently labeled PMMA particles were prepared using the first part of the emulsion polymerisation method described by Kumacheva *et al.* [69]. Approximately 0.4 g of potassium persulfate was dissolved in 140 g of water in a round-bottomed flask and heated to 80°C in a nitrogen atmosphere. The mixture was vigorously stirred at this temperature for 30 minutes to allow the initiator to fully dissociate, then 6 g of MMA quickly added. The emulsion was allowed to polymerise for 30 minutes, then a small amount of rhodamine dye dissolved in MMA (as prepared in [70]) was added. The mixture

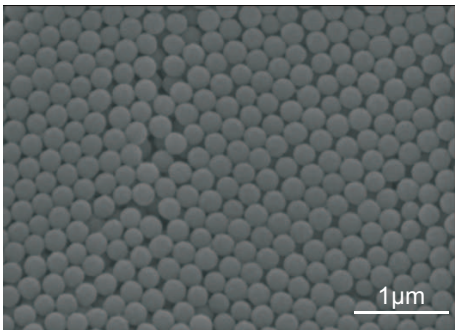


Figure 2.4: Scanning Electron Microscopy image of the PMMA colloids.

was allowed to stir for a further 30 minutes then the flask was removed from the heat source. The particles were characterised by Scanning Electron Microscopy and found to be around 210 nm in diameter with a low polydispersity (see figure 2.4). This was substantiated by the fact that the particles spontaneously crystalise upon sedimentation.

Xanthan solution was prepared as described in [57, 71, 72]. Using an identical batch of the polymer, originally provided by Dr R H Tromp (Nizo, Ede, The Netherlands), an aqueous solution of xanthan (SKW Biosystems, M_w = 4 x 10^6 gmol^{-1}) was prepared at a concentration of 2 mgml^{-1}. The polymer was dissolved in 0.1 M NaCl to screen double layer repulsions, and 2 mM NaN_3 was added to prevent the growth of bacteria. The radius of gyration of the polymer was calculated to be 264 nm [71] and its persistence length 120 nm, implying that the xanthan molecule is semi-flexible.

The colloid-polymer system was prepared by mixing the stock components together in appropriate concentrations, and was then homogenised either by shaking by hand, or using a vortex mixer. There is a small refractive index mismatch between the colloids and solvent ($n_{PMMA} = 1.49, n_{water} = 1.33$), therefore multiple scattering effects are more significant here than in the decalin system. The difference in refractive indices also means that the Van der Waals interactions between the colloids are not fully screened, however the colloids are stabilised by charge and no irreversible particle aggregation has been observed. The underlying DLVO potential will modify the depletion interaction at short lengthscales. A rough comparison using the depletion interaction for ideal polymers and typical numbers for the DLVO potential shows a significant difference in the potential only at distances shorter than 15 nm, less than 3% of the range of the depletion interaction.

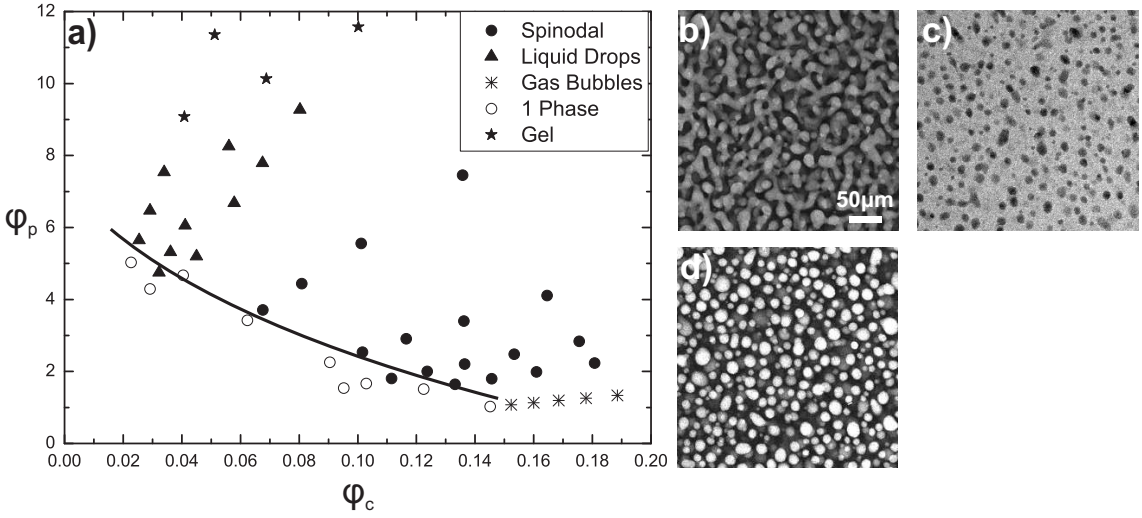


Figure 2.5: (a) Phase diagram of the PMMA - xanthan - water system. The thick black line represents the approximate position of the binodal. (b) Phase separation via spinodal decomposition. (c) Phase separation via Nucleation and Growth Mechanism (Gas Bubbles). (d) Phase separation via Nucleation and Growth Mechanism (Liquid Droplets).

We construct an experimental phase diagram by visual inspection (figure 2.5 (a)). The colloid and polymer concentrations are given in terms of their volume fraction ($\phi_c = 4/3\pi R_c^3 n_c$, $\phi_p = 4/3\pi R_g^3 n_p$), where the polymer is considered as a solution of interpenetrable spheres of radius equal to R_g, and n_c and n_p are the number densities of the colloids and polymers respectively. At low colloid and polymer concentrations no phase separation is observed; when these concentrations are increased we observe a two phase region in our phase diagram. We estimate the position of the binodal separating the one and two phase regions with a full black line. Should the concentrations become too high, the system will gel. No evidence of polymer adsorption was observed at any of the statepoints explored. Xanthan proves to be a very efficient depletion agent as only low concentrations of the polymer are required to induce a phase separation. Similar observations with a different colloidal molecule were observed in [56, 71].

Within the two phase region of the phase diagram, we observe demixing via spinodal decomposition from the unstable region of the phase diagram (figure 2.5 (b)), and demixing via the nucleation and growth mechanism from the metastable region (figure 2.5 (c) and (d)).

We observe that the minority phase forms liquid drops or gas bubbles depending on which side of the critical isochore the metastable region lies. It is interesting to note from inspection of the phase separation movies that the samples of this system separating via the nucleation and growth mechanism coarsen through the coalescence of diffusing droplets as suggested in [73], and seemingly not by Ostwald ripening as theoretically described in [74, 75]. The metastable region on the left hand side of the phase diagram is larger than expected. The spinodal network may break up into droplets at very small lengthscales, giving the system a nucleation and growth-like appearance [76, 77]. This could be related to a viscosity effect (unusually in this system the gas phase is more viscous than the liquid phase). For both demixing mechanisms, when the phase separating structures grow to a size comparable to the capillary length in the system, they are destroyed by buoyancy forces [78]. After a few hours, clean macroscopic interfaces are formed, and the thermal capillary waves fluctuating on the surface of the interface may clearly be observed.

2.4 Thermal capillary waves of PMMA-xanthan-water system

The capillary wave fluctuations of a fluid-fluid phase separated colloid-polymer mixture in a decalin solvent have been observed and analysed using capillary wave theory [5]. Here we shall provide a similar treatment for our water based system. Such an analysis of capillary waves provides a method of determining the various interfacial parameters in the system, for example the capillary length L_c, the interfacial tension γ and the capillary time τ. This technique is used repeatedly throughout this thesis.

A phase separating sample of the PMMA colloids and xanthan polymer was prepared at a state point of $\phi_c = 0.055$ and $\phi_p = 4.95$. The sample was homogenised, and sealed into a glass capillary of sufficient dimensions such that the system is not confined. The system was allowed to phase separate and equilibrate, and the capillary waves at the interface were recorded using CSLM.

An image of the interface between the colloidal liquid and gas phases is shown in figure 2.6 (a). The lower bright phase is the colloid rich liquid phase, and the upper, darker phase

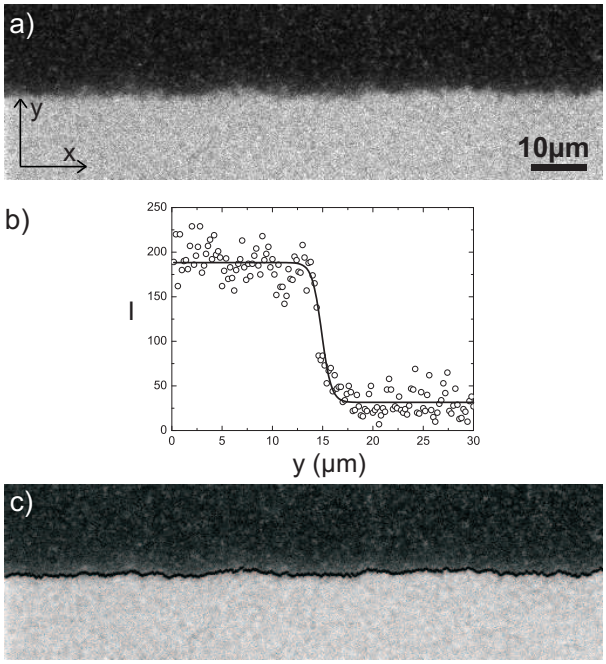


Figure 2.6: (a) Example image of capillary waves at the interface in the PMMA-xanthan-water system. (b) Fitting the intensity profile of a column of pixels with a tanh function. (c) The position of interface located upon a processed image.

is the colloid poor gas phase. The thermal fluctuations of the interface were recorded for a time totaling around 25 minutes and 5000 frames. To analyse the fluctuations we first locate the position of the interface in each image by fitting the intensity profile along a column of pixels with a tangent hyperbolic function [79] (see figure 2.6 (b)). This can be repeated for each of the columns to find the interface position across the whole image (see figure 2.6 (c)). We can then quantify our observations by studying the height distribution function, and constructing correlation functions of the fluctuations in both space and time. In figure 2.7 (a) we plot the height distribution of our fluctuations relative to the average interface position in each image (open circles). We observe the height distribution is of Gaussian form as expected [5, 80]- the full black line represents a Gaussian fit to our data.

In general the height correlation function g_h may be defined as:

$$g_h(x,t) = \langle [h(x',t') - \bar{h}(t')][h(x'+x,t'+t) - \bar{h}(t)] \rangle, \tag{2.1}$$

where x denotes the coordinate along the interface, t the time, and averages are over primed quantities. The height h at time t is defined with respect to the average height at that time

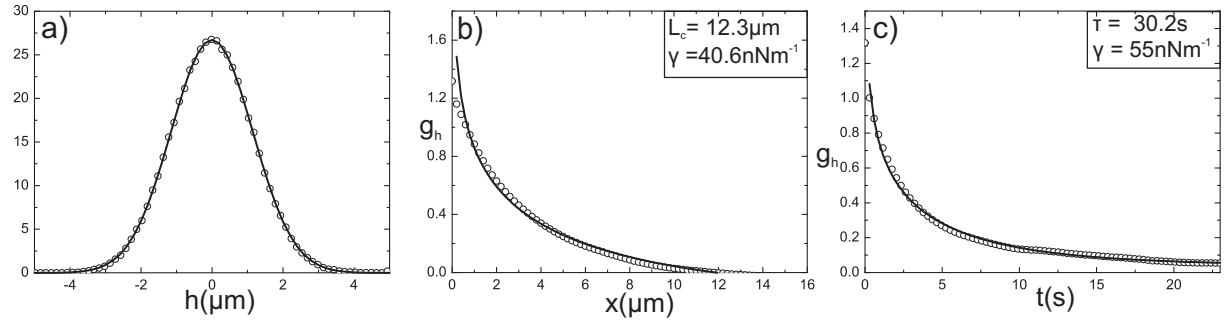


Figure 2.7: Height distributions (a), static (b) and dynamic (c) correlation functions of the interface fluctuations of the PMMA water system. The circles represent experimental data. The full lines in (a) represent a Gaussian fit and (b) and (c) are fits using capillary wave data. The insets show fitting parameters.

$\bar{h}(t)$. This is a slightly different method to the one used in [5] where heights were taken with respect to an average over both space and time, but similar to the method followed in [81]. The reason for this alternative analysis is to eliminate any systematic drift in the sample positioning, although one may lose the longest fluctuations in this case. In general, the total image width is much longer than the parallel correlation (capillary) length, so provided any systematic drifts are small, this should have a minimal effect on results.

From the capillary wave theory originally derived by Mandelstam [47] (for a review of this derivation see [82]) we know that in the capillary wave spectrum, each Fourier component $\mathbf{q}$ of the interface has a mean square amplitude given by:

$$\langle \mid h_{\mathbf{q}} \mid^2 \rangle = \frac{k_B T}{\gamma L^2} \frac{1}{q^2 + L_c^{-2}}. \tag{2.2}$$

The brackets on the left hand side of the equation represent a thermal average, and L_c is the capillary length. From this equation we can further derive expressions for the static and dynamic correlation functions [5, 47]:

$$g_h(x) = \frac{k_B T}{2\pi\gamma} K_o(\frac{x}{L_c}), \tag{2.3}$$

$$g_h(t) = \frac{k_B T}{2\pi\gamma} \int_0^{\bar{k}_{max}} d\bar{k} \frac{\bar{k}}{1+\bar{k}^2} exp(-(\bar{k} + \bar{k}^{-1})t/2\tau). \tag{2.4}$$

Figure 2.7 (b) shows the experimental static correlation function $g_h(x, t = 0)$ (open circles). The full line represents the fit from capillary wave theory (eqn. (2.3)) where we use γ and L_c as physical fitting parameters with an additional constant parameter included to account for any baseline offset (a term which is usually small) [5]. From this data we obtain a capillary length of 12.3 μm and an interfacial tension of 4.06 x 10^{-8} Nm^{-1} - values of similar order of magnitude in comparison to previous experiments on systems in organic solvents [5, 83]. The thermal roughness $L_T = \sqrt{g_h(x = 0, t = 0)}$ is calculated to be 1.1 μm, again comparable to that observed in previous experiment, and of suitable value such that the interface position may easily be located and tracked.

Examining our data more closely, at short lengthscales (below 1 μm) we observe that the experimental correlation function is no longer accurately described by the theoretical prediction. Here, one expects to find the largest deviations from standard capillary wave theory: taking only the interfacial tension and density difference into account leads to a logarithmically diverging interfacial width, where as the experimental width remains finite. Therefore to gain a better overall description of the function, the first three data points were left out of the fit. In previous experiments [5] this deviation from theory was not so prominent. Current observations may have various origins and a possible explanation may be found in the fact that the polymers are much larger than the colloids with a diameter of $2R_g \sim 530$ nm, which is slightly smaller than three pixels, but larger than the in plane confocal resolution. One may therefore speculate about the leading interfacial lengthscale, whether it would originate from the polymer rather than the colloid particle. Furthermore, making the problem more complicated, a third natural lengthscale would be the polymer persistence length, which is comparable to the colloid radius.

The dynamic correlation function $g_h(x = 0, t)$ is shown in figure 2.7 (c). Once again, the experimental data is represented by open circles, and the full line represents a fit from the theoretical function (eqn. (2.4)). Theoretically each mode is exponentially damped by $\exp[-t/2\tau_q]$ with

$$\tau_q = \tau \frac{qL_c}{1 + q^2 L_c^2}, \tag{2.5}$$

where τ is the capillary time and η is the sum of viscosities of both phases [84, 85]. The density of the phases does not appear since we are in the over damped low Reynolds number

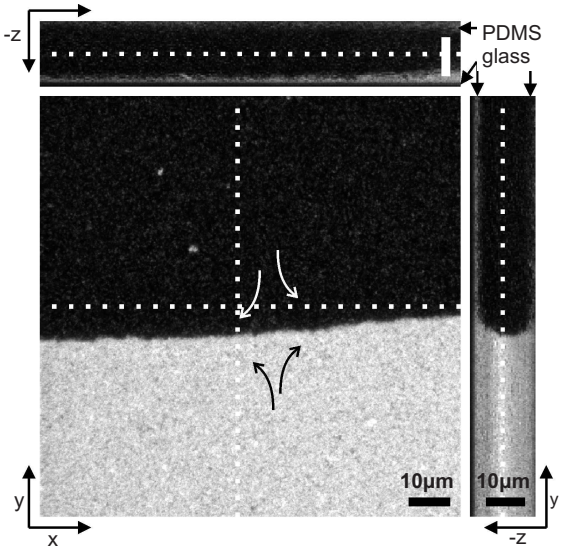


Figure 2.8: 3 dimensional CSLM image of the demixed water based system in a microfluidic cell.

limit. Similar to the static case, we use γ and τ as physical fitting parameters, with an additional constant parameter to compensate for any baseline offset. From this fitting we obtain an interfacial tension of γ = 55 x 10^{-9} Nm^{-1} and a capillary time of τ = 30.2s, again comparable to those obtained in previous experiment [5, 83]. The interfacial tensions obtained from the static and dynamic functions are in reasonable agreement, especially given the less accurate fit in the static case. The discrepancy between fit and experiment for the static function may not be so prominent in the dynamic case, as the waves are very effectively damped at short lengthscales.

Finally, we illustrate that our new colloid polymer system is compatible with PDMS cells. In figure 2.8 we show a three dimensional CSLM image of our system at a stagnation point of a cross channel. The white dashed lines indicate the positions of the x,y and z images, for example the yz slice is taken along the vertical line in the xy image. Gravity points along the negative z-axis, and the flow lines are roughly indicated by the arrows. We see that both the fluctuations of the interface and the wetting effects are clearly visible. We see bright layers of the liquid phase coating both the the glass and PDMS walls in the xz and yz images, indicating that both surfaces are wet by the colloid-rich phase.

2.5 Conclusion

We have outlined the use of confocal microscopy to image colloid-polymer systems, and a simple method to fabricate microfluidic cells which we may use to confine the sample. After highlighting the experimental issue of combining the cells with the systems in organic solvents, we outline the development of a new colloid-polymer system dispersed in water to circumvent this problem. We explore the phase behaviour of this new system, and show that we are able to induce fluid-fluid demixing from both the unstable and metastable regions of the phase diagram. Once the phase separation is complete, we observe the thermal capillary wave fluctuations on the surface of the macroscopic interface. We demonstrate the application of capillary wave analysis to this system and obtain very reasonable interfacial properties, although the capillary wave model could be extended to improve the fit of experimental data at small lengthscales. It is proposed that the origin of this discrepancy lies in the competing microscopic lengthscales within the system. In addition we demonstrate that our new system is compatible with microfluidics, the driving feature of its development.

We conclude that we possess a colloid polymer system compatible with a range of cells that are cheap and simple to produce, allowing us to study interfacial phenomena within a variety of dimensions. In combination with the technique of confocal microscopy, we are able to produce clear real space images of colloid-polymer systems in differing confinement geometries, giving us a flexible platform to perform a detailed analysis of interfacial, demixing and wetting phenomena.

Chapter 3

Probing the critical behaviour of colloidal interfaces by gravity.

ABSTRACT

We present a study of the interface between fluid-fluid phase separated colloid-polymer mixtures of identical composition but with varying suspension height. The significance of the sedimentation gradient present in the suspension is controlled by the ratio between the suspension height and the gravitational length of the colloids. We demonstrate that increasing the suspension height, and thus the importance of gravity leads to a systematic roughening of the gas-liquid interface as if one approaches the critical point. By carefully tuning the system height, the suspension can be brought arbitrarily close to criticality, irrespective of the overall composition of colloid and polymer. Our findings are based on measurements of the interfacial tension and capillary wave properties and supported by predictions from a simple density functional theory.

3.1 Introduction

Sedimentation has been a phenomenon of particular interest to colloid scientists since the pioneering work of J. B. Perrin in the early 1900s [1]. In his book, *Atoms*, he begins with a treatment of the density variation in a vertical column of gas molecules, and subsequently extends his arguments to describe such a profile in a colloidal suspension. The length scale controlling the sedimentation gradient is known as the gravitational length $\xi_c = k_B T/(m^* g)$,

where k_B is Boltzmann's constant, T the temperature, m^* the buoyant mass and g Earth's acceleration. Due to the increased size of the suspended particles, the gravitational length of a colloid is of $\mathcal{O}(10^{-3})$ m rather than $\mathcal{O}(10^3)$ m for a gas molecule. This allowed Perrin to study the sedimentation gradient in the laboratory. Through simple experiments he was able to demonstrate the exponential variation of colloid concentration with height in an ideally dilute suspension, obtaining accurate numbers for Boltzmann's constant and thus Avogadro's number.

The effect of a uniform gravity field is still being employed in colloid science, for example in obtaining the equation of state in suspensions of charged colloids at densities ranging from the dilute to the dense limit from careful measurements of the sedimentation gradient [86,87]. It has also been used to probe the phase behaviour of various suspensions of colloidal platelets [88, 89]. When we consider a two component system such as a colloid-polymer mixture, the situation gets more complicated, as shown by theoretical studies in [88, 90]. In such systems, should phase separation take place a colloid rich, polymer poor 'liquid' phase and a colloid poor, polymer rich 'gas' phase shall be formed [32, 33] (see also chapter 1). In the presence of a gravitational field, the distribution of the colloids will be controlled by the gravitational length of the colloids ξ_c with respect to the container height H. Owing to their small buoyant mass, the gravitational length of the polymer is extremely large and the polymer component can be considered unperturbed by the external gravitational field.

Since the overall concentrations of colloid are fixed, sedimentation leads to a repartitioning of the colloids along the vertical direction of the container. The resulting non-uniform colloid density distribution is accompanied by a similar non-uniform polymer distribution since the densities of the two species are coupled via the local free volume [38]. In reference [90] it has been shown that for such a closed system gravity has a profound effect on the gas-liquid interface. For an open (bulk) system, free-volume theory predicts that the gas-liquid coexistence densities and interfacial tension are solely dependent upon the polymer chemical potential μ_p, proportional to the amount of added polymer. This quantity directly measures the strength (i.e. depth) of the attractive depletion interactions between the colloids which can be interpreted as an effective temperature locating the position in the gas-liquid phase diagram. Upon lowering the polymer chemical potential the system moves toward the critical

point and eventually moves out of the gas-liquid region into the fluid state upon further reduction. For a *closed container* with height H and fixed overall colloid and polymer concentration, μ_p is found to be strongly dependent on H, such that μ_p is a monotonically decreasing function of H [90], irrespective of the overall species concentration. This implies that by increasing H the interfacial properties of a colloid-polymer mixture will resemble those of a (zero-gravity) bulk system at an effective temperature moving toward the critical point. Consequently, there is a critical container height at which the gas-liquid interface vanishes and the system behaves as a single-phase fluid (subjected to a gravitational field).

In this chapter we present an experimental study of the effect of gravity upon interfacial behaviour in colloid-polymer mixtures. The focus will be on the properties of the interface, which turn out to be a very sensitive probe. In the preceding chapter and reference [5], it has been shown that thermal fluctuations of the interface can be directly observed and by performing a capillary wave analysis on these waves, we can determine the values of the interfacial properties. The key parameters are identified as: the mean square roughness of the interface $\sqrt{\langle h^2 \rangle} \propto \sqrt{k_B T/\gamma}$, the in plane correlation or capillary length $L_c = \sqrt{\gamma/\Delta\rho g}$ and the typical decay time of the fluctuations $\tau = L_c \eta/\gamma$. Since the interfacial tension and the local density difference across the interface depend on the container height, the capillary fluctuations will be influenced by gravity as well.

We begin in section 3.2 with a brief discussion of the density functional theory to provide a theoretical setting of the experiment. This was performed by our collaborator Rik Wensink, then of Imperial College, London, now of Heinrich-Heine-Universität, Düsseldorf. The theory should be considered as a qualitative benchmark aimed at providing a simple theoretical underpinning for the characteristics of the interface as a function of container height. The two sections after that are devoted to a presentation and of discussion the experiments. We conclude in section 3.5 by considering the implications of this work.

3.2 Density functional theory

We here largely follow Schmidt *et al.* in their description of the problem [90]. Within density functional theory (DFT) the grand potential $\Omega[\rho_c]$ of a colloidal fluid in a container of height

H is a functional of the density distribution $\rho_c(z)$, which measures the local colloid density at the vertical coordinate z. The potential is minimised by the *equilibrium* density distribution at a given temperature T and container height [91]. For a mixture of colloids and ideal polymer the well-known free-volume theory [38] can be invoked. Within the local density approximation (LDA), valid if the local density varies slowly over distances comparable to the colloid size, the grand potential per unit volume V takes the following form [90]:

$$\begin{aligned}\frac{\beta\Omega[\phi_c]v_c}{V} &\simeq \frac{1}{H}\int_0^H dz\left\{\phi_c(z)\left(\ln\phi_c(z)-1\right)+\frac{\phi_p(z)}{q^3}\left(\ln\frac{\phi_p(z)}{\alpha[\phi_c(z)]}-1\right)\right.\\ &\left.+f_{HS}^{ex}[\phi_c(z)]-\beta\mu_c\phi_c(z)-\beta\mu_p\frac{\phi_p(z)}{q^3}+\frac{z}{\xi_c}\phi_c(z)\right\},\end{aligned} \tag{3.1}$$

with $\beta = 1/k_BT$ and $\phi_{c/p} = \rho_{c/p}v_{c/p}$ the packing fraction of the colloid (c) and polymer (p) with $v_{c/p}$ the particle volume of the corresponding species and $q = R_g/R_c$ the polymer-colloid size ratio in terms of the polymer radius of gyration R_g and the colloid radius R_c. The first two terms are the ideal contributions for the colloid and polymer. Locally, the polymer density ϕ_p is coupled to the colloid density via the *free-volume fraction* $\alpha(\phi_c)$ which expresses the average fraction of the system volume available for the (ideal) polymer at a given colloid packing fraction ϕ_c. The third term represents the excess free energy density $f_{HS}^{ex} = \beta F_{HS}v_c/V$ of the *homogeneous* hard sphere fluid, while the last term stems from the gravitational potential m^*gz acting on the colloids. The undetermined multipliers μ_c and μ_p are associated with the constraints of a *fixed* overall concentration of colloid and polymer:

$$\begin{aligned}\frac{1}{H}\int_0^H dz\phi_c(z) &= \phi_c^0,\\ \frac{1}{H}\int_0^H dz\phi_p(z) &= \phi_p^0.\end{aligned} \tag{3.2}$$

In case of an unbounded system μ_c represents the colloid chemical potential and μ_p the chemical potential of a hypothetical reservoir of ideal polymer in contact with the system. The density of polymer in the reservoir is then given by:

$$\phi_p^R = \exp[\beta\mu_p]. \tag{3.3}$$

A formal minimisation of the grand potential with respect to the species densities leads to a set of coupled self-consistency equations:

$$\begin{aligned}\phi_c(z) &= \exp\left\{\beta\mu_c - \beta\mu_{HS}^{ex}[\phi_c(z)] + \frac{\phi_p(z)}{q^3}\frac{\partial \ln\alpha[\phi_c(z)]}{\partial\phi_c(z)} - \frac{z}{\xi_c}\right\} \\ \phi_p(z) &= \phi_p^R\alpha[\phi_c(z)] \end{aligned} \tag{3.4}$$

which must be solved along with the conditions in eqn. (3.2). Explicit expression for the excess chemical potential $\beta\mu_{HS}^{ex} = \partial f_{HS}^{ex}/\partial\phi_c$ and free-volume fraction α of the hard-sphere reference fluid can be obtained from the Carnahan-Starling equation of state and Scaled Particle Theory, respectively (see [38] for details). With this, the equilibrium density profiles can be calculated for a given q, container height H/ξ_c and overall species volume fractions ϕ_c^0 and ϕ_p^0.

For a bulk system without gravity, the interfacial tension can be calculated from a simple square-gradient approach, as outlined in reference [92]. The result is:

$$\beta\gamma R_c^2 = \frac{3}{\pi}\int_{\phi_c^G}^{\phi_c^L} d\phi_c \sqrt{m\left(f_{HS}(\phi_c) - q^{-3}\phi_p^R\alpha(\phi_c) - \beta\mu_c^B\phi_c + p^B\right)}, \tag{3.5}$$

in terms of the bulk gas-liquid coexistence densities $\phi_c^{G/L}$, pressure $p^B = \beta P v_c$, colloid chemical potential μ_c and reservoir polymer density ϕ_c^R. The square-gradient coefficient m is linked to ϕ_p^R via $m = \phi_p^R\mathcal{F}(q)$, with $\mathcal{F}$ specified in [92]. Expression (3.5) can also be applied to the present case if we identify μ_p^B with $\mu_p(H)$, the polymer chemical potential of the sedimented system at a given H/ξ_c, and calculate the corresponding bulk coexistence quantities. The interfacial tension then follows from a simple integration according to eqn. (3.5) without having to recalculate the density profiles.

The results in figure 3.1 demonstrate the profound effect of the container height on the local gas-liquid interface for a system with fixed overall concentrations $\phi_c^0 = 0.02$ and $\phi_p^0 = 1.0$. The associated statepoint has been indicated in figure 3.1 (a) and its relative location to the critical point is qualitatively similar to the experimental system described in the next section. Within LDA, the gas-liquid interface is represented by a simple step profile. Upon increasing H/ξ_c, the density gap across the interface reduces and vanishes at a critical container height $H_{crit}/\xi_c \approx 75$ where the system locally reaches the critical point. The corresponding interfacial tension decreases rapidly upon approach of H_{crit}/ξ_c and strictly becomes zero at the

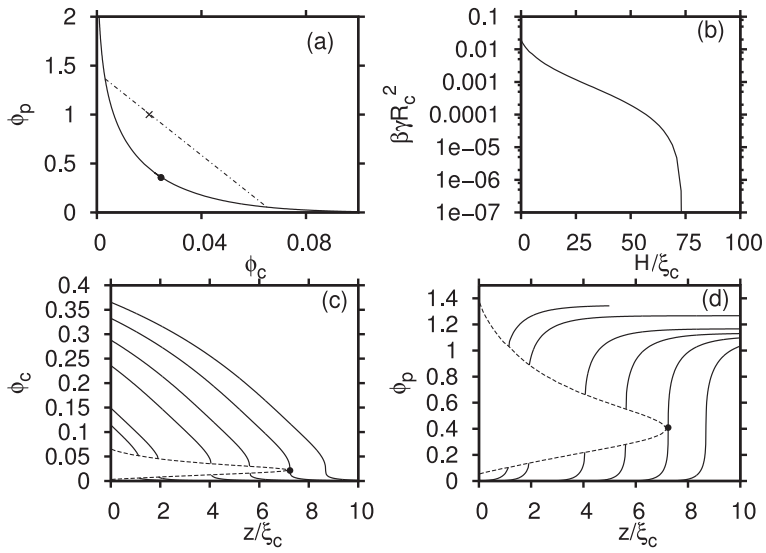


Figure 3.1: (a) Gas-liquid binodals at zero gravity of a colloid-polymer mixture with $q = 2.5$ from free-volume theory. The critical point is indicated by the dot. A tie line connects the coexisting phases for the statepoint $\phi_c^0 = 0.02$ and $\phi_p^0 = 1.0$, indicated by the cross. (b) Interfacial tension versus container height H/ξ_c for the state point indicated in (a). (c) Colloid density versus height for systems with various container heights, $H/\xi_c = 5$, 10, 30, 50, 75 and 100 (from left to right) for the same state point. (d) Same results for the polymer density.

critical point. In reality, bulk gradients due to the gravitational field (neglected in (3.5)) also contribute to the interfacial tension, albeit only marginally. Moreover, critical fluctuations are at play which are not incorporated in our mean-field theory. These factors will become manifest close to the critical point and change the qualitative behaviour of the interfacial tension with H/ξ_c close to H_{crit}/ξ_c. Nevertheless, the steep decrease of the interfacial tension (and related properties) upon increasing the container height is expected to be robust and should be clearly observable in experiment.

3.3 Experimental system and method

Using the system of PMMA colloids and xanthan polymer dispersed in water described in chapter 2, a sample at a statepoint of $\phi_c^0 = 0.055$ and $\phi_p^0 = 4.946$ was prepared. The phase

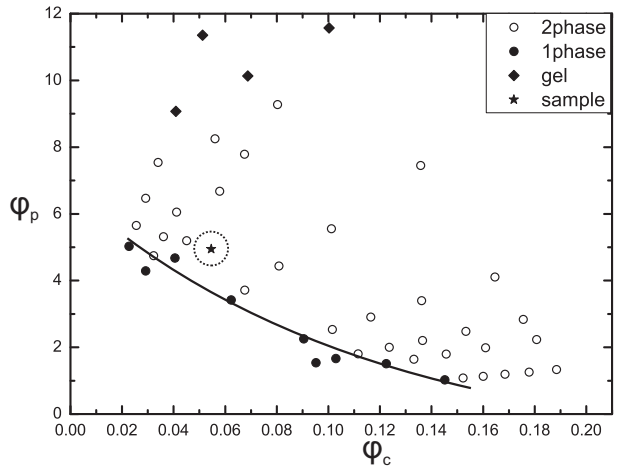


Figure 3.2: Phase diagram of the experimental colloid-polymer mixture. Plotted is the polymer density ϕ_p versus the colloid packing fraction ϕ_c. The line indicates the location of the binodal. The triangle denotes the estimated position of the critical point, and the star the sample statepoint.

diagram of this system is reproduced in figure 3.2, anotated to show the sample statepoint and the estimated position of the critical point. The gravitational length of the colloids was 0.5 mm. The stock solution of colloid-polymer mixture was homogenised by vigorous shaking, and sealed into tubes of dimensions 1 mm x 0.1 mm x H (Vitrotubes P/N 5010). The height H of the tubes varied from 10 mm to 25 mm, a range expected to clearly illustrate gravitational effects. Different statepoints were found to show this effect over various height ranges of tubes, which may be impractically small or large, but qualitatively similar behaviour was found. Furthermore a small change in statepoint can lead to a significant alteration in H_{crit}.

The sealed tubes were left undisturbed for 11 days. Additional measurements, where a sample was followed over time showed that after roughly a week the interface had reached a state which was no longer changing, thus 11 days should be sufficient for the samples to equilibrate fully. Equilibration times may again vary per statepoint and sample height. The interface between the colloidal liquid and gas phases in each tube was examined and the thermal fluctuations on its surface recorded using CSLM. The interface position on each image was located, and real space correlation functions constructed as described in chapter

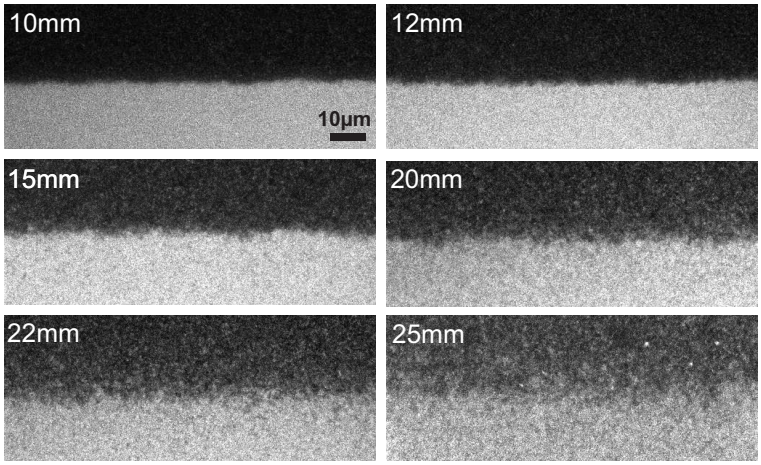


Figure 3.3: CSLM images of interfaces as a function of suspension height H (indicated in each image).

2. Theoretical correlation functions following from standard capillary wave theory (eqns. (2.3) and (2.4)) were fitted to the experimental data to obtain the physical parameters of the interface.

3.4 Results and discussion

The effect of gravity is most clearly illustrated in figure 3.3. As the suspension height is increased the interface becomes more diffuse and the magnitude of the fluctuations becomes larger. The density difference between the two phases, related to the intensity difference in the images, diminishes to the point at which the eye struggles to locate the interface at all. When the critical ratio of H/ξ_c is reached, the density profile is observed to move smoothly between the two phases. This has been exemplified in figure 3.4 where images have been taken of an alternative set of tubes with $\phi_c^0 = 0.053$ and $\phi_p^0 = 4.932$, with objectives of 10x and 63x magnification. At small suspension height the interface is very sharp, whilst at a larger height it is no longer possible to pinpoint the interface. The inset graphs show the average intensity per row as a function of height. The fluorescence intensity is an indirect measurement of the colloid concentration providing us with a representation of the density profile. The non-linear response of the detector means that we cannot directly compare the two density profiles, but for the 7 mm tube there is a sharp jump from gas to liquid density

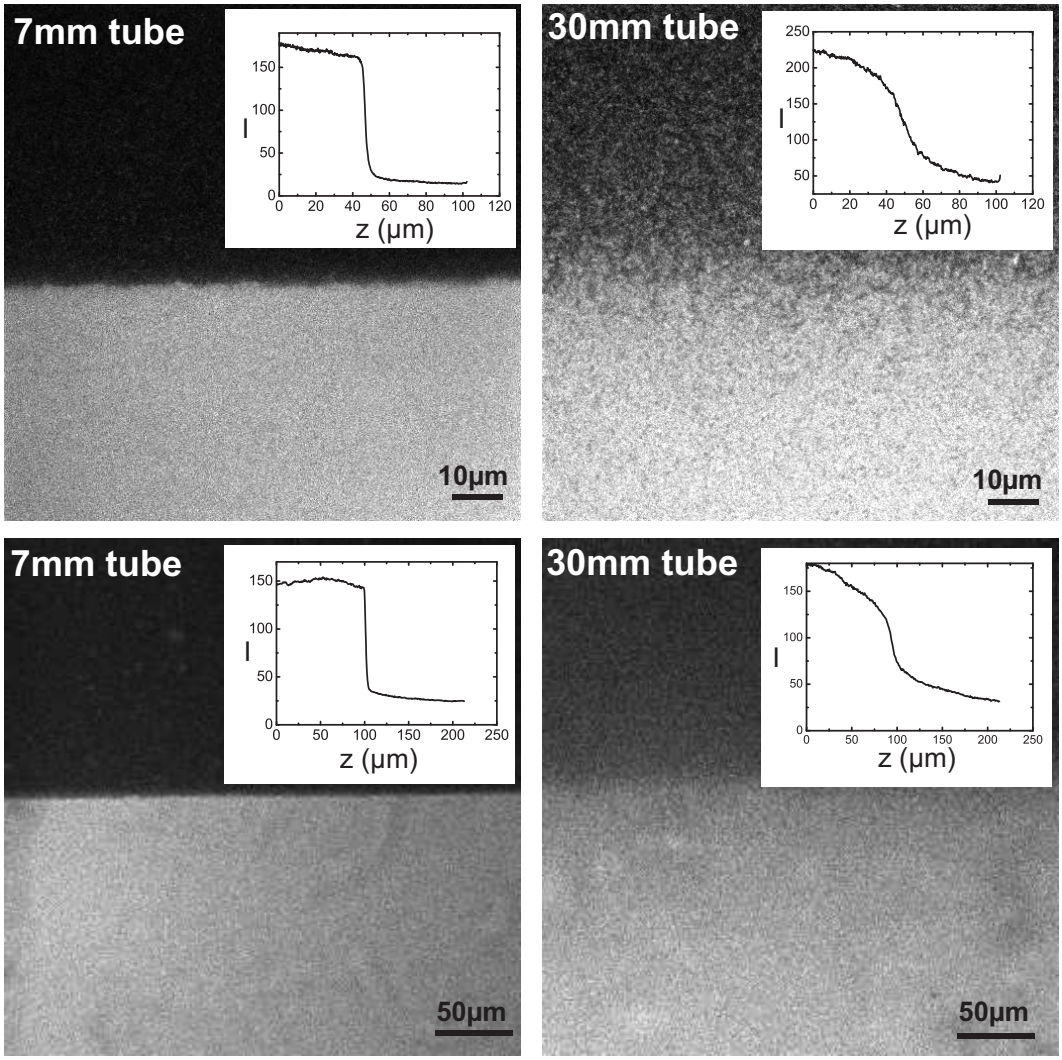


Figure 3.4: CSLM images of the interface in 7 mm and 30 mm tubes taken with a 63x (upper) and 10x (lower) objective. Insets show average intensity through the interface for the images shown.

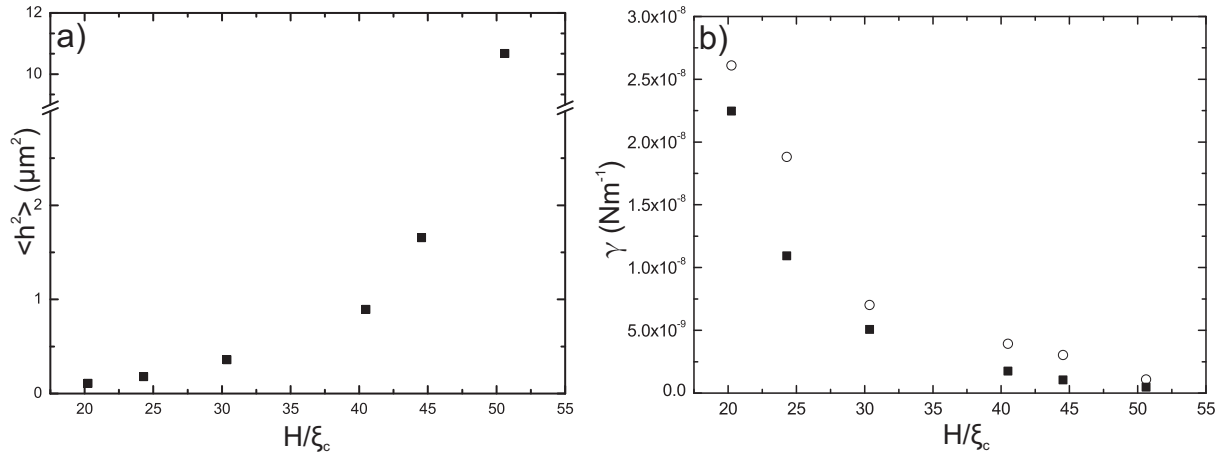


Figure 3.5: (a) Interfacial roughness as a function of the relative system height. (b) Interfacial tension with respect to the relative system height. The black squares denote the interfacial tension determined from the static correlation function, and the open circles from the dynamic correlation function.

in especially the 10x image, whereas there is a smooth transition from gas to liquid for the 30 mm tube even at low magnification.

These observations are in qualitative agreement with the theoretical predictions (see e.g. figure 3.1 (d)), whereby increasing H the effective temperature increases and moves towards and eventually beyond the critical point. We can quantify these observations by plotting the interfacial roughness $\langle h^2 \rangle$ as a function of suspension height (figure 3.5 (a)). Here, one observes that the roughness strongly increases as the suspension height is increased. It should be noted that as the interface becomes more diffuse, it becomes increasingly difficult to locate, and this uncertainty contributes to $\langle h^2 \rangle$. It is estimated from this data and the images in figure 3.4 that the interface effectively disappears at a critical height $H_{crit} = 30$ mm.

The fluctuations can be analyzed further to learn about the interfacial properties; to that end correlation functions are constructed and fitted to the theoretical expressions as in [5, 56]. As expected both the capillary length and interfacial tension of the system decrease as the suspension height increases (figures 3.5 (b) and 3.6). The capillary waves also yield information about the dynamics, see figure 3.7. Here it is observed that the capillary

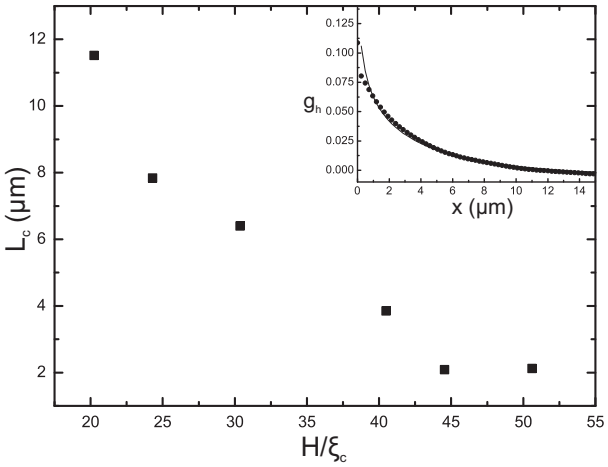


Figure 3.6: Capillary length as a function of the relative system height. Inset shows the static correlation function for the 10 mm tube from experiment (circles) and fitting following capillary wave theory (full lines).

time increases with the suspension height, but levels off as H_{crit} is approached. Previous experiments [5, 51] where samples were made along a a dilution line show the same trends as here. In this conventional situation, however, the state point of the system is determined by the relative weight fraction of the colloid and polymer components, and it is difficult to accurately control the properties of the interface in the vicinity of the critical point. Small uncertainties in weighing in the respective components make it experimentally very hard to get very close to the binodal, let alone the critical point. By increasing the height of the suspension and exploiting the influence of gravity, we are here able to move the interfacial state point arbitrarily close to criticality thus providing a much more sensitive and accurate way to explore the behaviour of the system in the critical region.

Clearly, the control parameter specifying the (relative) distance to the critical point is now no longer the relative amounts of colloids and polymers, but it has become a single parameter, namely the ratio of the suspension height over the gravitational length, H/ξ_c. There is, however, still an experimental challenge in pinpointing the critical height. Furthermore, the relation between suspension height and reservoir polymer concentration for interacting polymers needs to be established in order to compare to critical exponents (see also section 3.5). Qualitatively the experimental data displays the expected critical behaviour, except

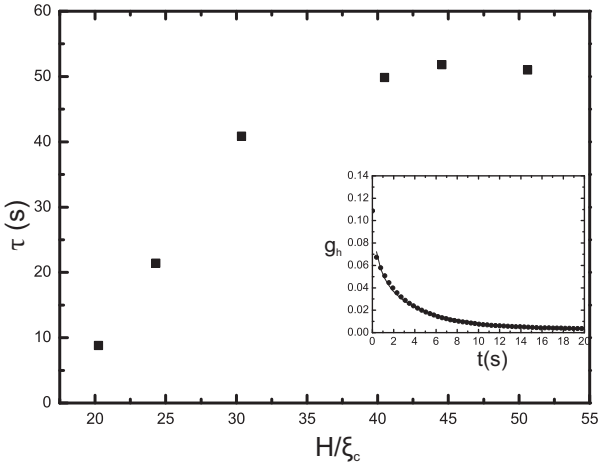


Figure 3.7: Capillary time as a function of the relative system height. Inset shows the dynamic correlation function for the 10 mm tube from experiment(circles) and fitting following capillary wave theory (full lines).

for the capillary time, which levels off unexpectedly as the critical point is approached, the reason for which is unclear. It could be related to the precise route through the phase diagram taken by the system as a function of H. Alternatively, it is possible that full equilibrium has not yet been attained for the longest tubes. The position of the interface was found to be dropping very slowly during measurement for the longest tubes, although the interfacial tension from both the static and dynamic correlation functions yielded similar results, suggesting that a reasonable equilibrium had been achieved. Such dynamical effects will be presented elsewhere [93], but from these experiments it is clear that in approaching equilibrium the system moves towards the critical point in line with the trends above.

3.5 Conclusion

We have shown both in theory and experiment that the height of the suspension relative to the gravitational length of the colloids affects the interfacial properties of a fluid-fluid phase separated colloid-polymer mixture. By increasing the height of a suspension beyond the gravitational length of the colloidal species, the colloidal particles rearrange into an inhomogeneous sedimentation profile. Although the overall concentration of colloids and polymers in the system is fixed, the hypothetical polymer reservoir concentration decreases

and the behaviour of the interface will adjust accordingly. For greatly increased heights the reservoir concentration will drop below its critical value, and there will no longer be an interface separating the two phases.

In the above view H is a measure of how close the interface is to the critical point, and it thus acts as the control parameter. It turns out that when treating the polymers as ideal, as done in the theory above, H is inversely proportional to ϕ_p^r such that it is clear how the critical point is approached upon varying the suspension height. For interacting polymers, which is the experimental situation, the relation is yet to be evaluated. But once this has been established theoretically, the presented approach opens up the possibility to measure a number of interface properties in light of their governing critical exponents. Previous experimental work focusing on critical exponents has shown different results [94–97], even in very similar systems (stearyl coated ludox particles, poly(dimethyl-siloxane) polymer, dispersed in cyclohexane) and applied techniques (spinning drop technique [95,96]). Recently, extensive simulations and theory have shown that the AOV model falls within the 3 dimensional Ising universality class [98], without exponent renormalization. Possible experimental difficulties lie in locating the critical point exactly and preparing systems very close to the critical point in a systematic manner (see also the discussion in [99]). The latter point is tackled by the presented approach, but determining the critical sample height, i.e. the height which corresponds to the critical point, remains a challenge and will be the subject of further investigations.

Acknowledgments It is a pleasure to thank Matthias Schmidt and Roel Dullens for stimulating discussions. We also thank Rik Wensink for his contribution to the theory section of this chapter.

Chapter 4

Sedimentation-diffusion dynamics in colloid-polymer mixtures

ABSTRACT

We show experimentally how a phase separated colloid-polymer mixture finds its sedimentation-diffusion equilibrium after initial fluid-fluid demixing. During this equilibration process we measure key parameters of the colloidal interface by assuming local mechanical equilibrium and we inspect the behaviour of the meniscus close to a vertical wall. It turns out that the kinetic pathway associated with the sedimentation process not only strongly depends on the overall colloid and polymer concentrations but also on the height of the suspension. Beyond a certain height the system locally passes through the gas-liquid critical point which opens new ways to study critical phenomena.

4.1 Introduction

A key experiment in colloid science is to study the behaviour of colloidal systems in Earth's gravitational field. The resulting sedimentation-diffusion equilibrium can be interpreted using statistical mechanical theory which has led to an accurate determination of Boltzmann's constant k_B [1]. In more recent years sedimentation experiments have been used to determine the equation of state of dense colloidal suspensions [86,87] and to probe the phase behaviour of colloidal platelets [89]. In computer simulations, a similar external gravitational field can

be imposed to determine equations of state [100]. The 'gravitational' forces acting on the colloids can be increased considerably by using an ultra-centrifuge. This technique has e.g. revealed the presence of a macroscopic electric field in sedimented suspensions of charged colloidal particles [101].

In the previous chapter we showed that the effective temperature (or state-point) of a colloid-polymer mixture in which only the colloidal particles are affected by gravity not only depends on the overall concentrations of the colloids and polymers but also on the height of the suspension [102], as predicted by Schmidt *et al.* [90]. The main issue addressed in this work is how the system reaches its sedimentation-diffusion equilibrium, starting from an initial state formed by two homogeneous, coexisting phases.

As the system approaches its equilibrium density distributions in the gravitational field the local effective temperature at the gas-liquid interface gradually increases and approaches its critical value. The effect of gravity is thus analogous to a change of the temperature in molecular systems as employed in several studies to measure the interfacial tension of a binary liquid mixture brought toward one-phase equilibrium by heating [103–106]. In our work the main control parameter is the suspension height rather than the temperature of the suspension. The effect of gravity allows us to simultaneously study the bulk and interfacial properties as well as the wetting behaviour at the container wall by direct, optical techniques. In this work we will analyse the thermal capillary waves of the interface and the meniscus at a vertical wall during the sedimentation process.

We organise this chapter as follows. In section 4.2, we first provide a brief theoretical background of the effect of gravity on the thermodynamic state of the suspension, in collaboration with Rik Wensink. This is followed by a description of the experimental methods and techniques. We then present and discuss our results before concluding.

4.2 Theoretical background

In the previous chapter we have showed that the equilibrium colloid density profiles and the resulting effective temperature of the mixture depends sensitively on the height of the suspension H [90, 102]. We will not repeat the theory here but merely explain how the

effective temperature or state-point of the system in a gravitational field is affected by the system height.

Let us consider a mixture of colloids (c) and polymers (p) in a continuum background solvent at fixed temperature T. The overall volume fractions ϕ_c^0 and ϕ_p^0 are chosen such that the system is in the two-phase region of the phase diagram. Without gravity, the phase behaviour can be qualitatively described by free volume theory [38], in which the polymers are treated as ideal freely interpenetrable spheres which experience a hard-core interaction with the colloids. The effective attractive force between the colloidal particles is induced by the depletion effect described in chapter 1 (see also [32, 33]). Due to steric repulsions the centres-of-mass of the polymers are excluded from a zone around each colloidal particle. If two colloids are sufficiently close so that the depletion zones overlap, the polymers will be entirely depleted from the space between the colloids resulting in an imbalance of osmotic pressures between the inner and outer zones which pushes the particles together. More refined polymer models may provide better (and sometimes quantitative) agreement with experimental phase diagrams [6,107], but here we will stick to the simple picture. The system under consideration will phase separate into colloidal liquid and colloidal gas phases; the main experimental control parameters are the overall concentrations of the colloid and polymer. In theory, however, one may consider the colloid-polymer mixture to be in osmotic equilibrium with a reservoir (r) containing a pure polymer solution kept at a chemical potential μ_p^r. The semi-permeable membrane separating the system from the reservoir only allows the polymers to pass through. Within free volume theory, the volume fraction of the polymers in the *system* ϕ_p is related to the polymer volume fraction in the reservoir ϕ_p^r via

$$\phi_p = \phi_p^r \alpha(\phi_c), \tag{4.1}$$

with α the free volume fraction, i.e. the fraction of the system volume which is available to the polymers. This quantity is a decreasing function of the colloid volume fraction $\phi_c = \rho_c v_c$, with ρ_c the colloid number density and v_c the volume of a single colloidal particle. An explicit expression for α for hard sphere systems can be found in [38]. Increasing the polymer concentration in the reservoir enhances the amplitude ε of the attractive depletion potential so that ϕ_p^r can be interpreted as an inverse effective temperature, i.e. $T_{eff} \equiv k_B T/\varepsilon \sim 1/\phi_p^r$ [102].

Let us now subject the system to a gravitational field. In practice, the gravitational length defined as $\xi = k_B T/m^* g$ with m^* the buoyant mass and g Earth's acceleration will be virtually infinite for a polymer molecule in a good solvent (due to its vanishing buoyant mass) but finite for a colloidal particle. The gravitational field will induce a new equilibrium state characterized by a smooth gradient in the colloid concentration in both liquid and gas phases. The equilibrium colloid density profile $\rho_c(z)$ (with z the position along the direction of gravity) in the sedimented state follows from mechanical equilibrium:

$$\frac{d\Pi[\rho_c(z)]}{dz} = -m^* g \rho_c(z), \tag{4.2}$$

with Π the osmotic pressure of the colloids [38]. Moreover, the overall volume fractions of colloids and polymers should be recovered when integrating the density profiles over the total suspension height H:

$$\phi_c^0 = \frac{1}{H}\int_0^H \phi_c(z)dz \quad \text{and} \quad \phi_p^0 = \frac{1}{H}\int_0^H \phi_p(z)dz. \tag{4.3}$$

Although the polymers are not directly affected by the gravitational field, they are redistributed along the gravity direction of the container since the local polymer concentration depends on the local colloid concentration via eqn. (4.1). By combining eqn. (4.1) with the conservation condition for the overall polymer concentration eqn. (4.3) one can write for the effective temperature:

$$T_{eff} \sim \frac{1}{\phi_p^r} = \frac{1}{H\phi_p^0}\int_0^H \alpha[\phi_c(z)]dz. \tag{4.4}$$

If gravity is absent the colloid concentration profile will be homogeneous along z so that $\phi_c(z) = \phi_c$ and $T_{eff} \sim \alpha(\phi_c)/\phi_p^0$, independently of H. In the presence of gravity the colloid concentration will vary along the z direction and the integral in eqn. (4.4) becomes, in principle, dependent upon the suspension height. At very low volume fractions, the colloids behave as an *ideal* gas and the free volume is a linearly decreasing function of the volume fraction $\alpha(\phi_c) \sim 1 - A\phi_c$ (with the constant $A > 0$ determined by the colloid-to-polymer size ratio). In this case T_{eff} will *not* depend on the suspension height as can be inferred from combining eqn. (4.3) and eqn. (4.4). At finite volume fractions, however, the colloid interactions are non-negligible and the free volume fraction becomes a strongly non-linear function of the colloid volume fraction [38]. The non-linear form of α dictates that T_{eff}

always increases with respect to H independent of the shape of the colloid sedimentation profile $\phi(z)$ or overall concentrations ϕ_c^0 and ϕ_p^0. Quantitative results from free volume theory have been presented and discussed in [90, 102], where it becomes evident that there always exists a critical suspension height H_{crit} at which the gas-liquid interface is at a critical point with an associated critical effective temperature T_{eff}^{crit}. In [102] we have shown experimentally that this is indeed the case. In this paper we will focus on the kinetic pathway along which sedimentation-diffusion equilibrium is reached.

4.3 Experimental system and method

Similar to the previous chapter, we use the system of PMMA colloids and xanthan polymer dispersed in water described in chapter 2. The gravitational length of the colloids ξ_c was 0.5 mm. We have had to work with two different batches of colloids (with a very similar absolute size and size distribution), since experiments have been conducted over the period of more than a year in order to fully probe the suspension height dependence.

A tube of dimensions 1 x 0.1 mm x H (Vitrotubes P/N 5010) was filled with homogenised colloid-polymer mixture, and was placed upright (with dimension H the suspension height) immediately after sealing. It was then imaged using CSLM as it moved towards equilibrium. The sample was kept in a temperature controlled room and disturbed as little as possible.

The interfacial properties and the position of the interface relative to the height at which it formed was measured over a period of days until all parameters had stabilised. Information about interfacial properties was procured from the analysis of capillary wave fluctuations as previously described in [5, 108] and chapter 2. The interface was imaged over a period of approximately 25 minutes in which 5000 frames were recorded, then the capillary waves were analysed using Mathematica. The interface was located in each column of pixels by fitting a hyperbolic-tangent function to the intensities of the pixels along the column [79] as demonstrated in figure 2.6. When the interface became very diffuse, the fitting procedure failed for some of the columns. In this case the interface for that column was located in the mean position between located points either side of it. When more than 3% of the interface location failed, the interface could no longer be located accurately enough to determine the

interfacial properties.

Real space correlation functions of the interfacial fluctuations were constructed as described by eqn. (2.1). Using the capillary wave theory detailed in chapter 2 [47], we fit the experimental static and dynamic correlation functions to obtain the physical parameters of the interface (L_c, γ, τ). The analysis differs slightly from that previously, (and in more detail in [5, 108]) as we attempt to quantify the uncertainty in our results. Here we split our recordings into 5 sections of 1000 frames, then calculated and analysed the correlation functions for each of these sections as described. We took the average value for each of the 5 fits and determined the associated error bars by calculating the standard deviation.

The average position of the interface was tracked over time by locating the position of the interface for a single frame and calculating its average height. The displacement of the interface was then recorded relative to the initial position of the interface, i.e. after it had first formed. For the sample with $H > H_{crit}$ the gas-liquid interface vanished and the 'interface' was then located by averaging the intensity across each of the rows in the image, and fitting a hyperbolic-tangent function to this averaged profile. This method produced almost identical results for the earlier less diffuse interfaces, and vastly improved the location at later times.

4.4 Results and discussion

In this section we will first discuss the qualitative aspects of the sedimentation dynamics in general, followed by a brief introduction to three specific cases. Next, we present quantitative results for these three cases.

Immediately after homogenisation, the sample starts to phase separate. The chosen state-points are in the spinodal region of the phase diagram, where the initial volume ratio of liquid to gas phase after phase separation is about 20:80. The phase separation process is in agreement with previous experiments on a different colloid-polymer mixture [7]. The typical lengthscale of the spinodal pattern increases, a process which is driven by interfacial tension, which tries to minimise the interfacial area [78]. This happens right after a diffusion-type regime, the timescale of which is too short to be recorded in our experiments [7, 25]. When the typical lengthscale has reached a certain size, gravity starts pulling the phases apart and

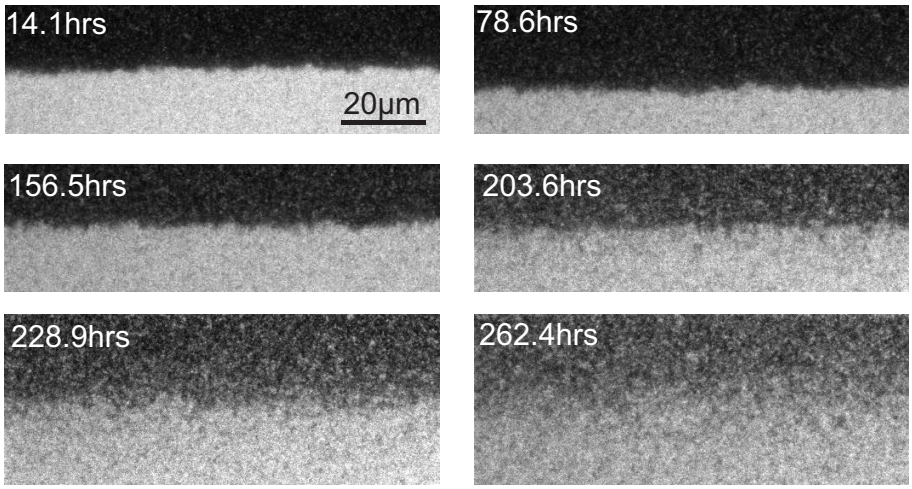


Figure 4.1: Images of the change in the interface with time in a sample with $H \approx H_{crit}$, case (i).

the liquid phase becomes discontinuous. A macroscopic interface between the two phases is formed at the bottom of the tube after about 10 minutes and rises upward as droplets of liquid sediment slowly towards the bottom. After a few hours a clean, macroscopic interface has been formed. At this timescale sedimentation gradients have not yet been established and the average colloid concentration is roughly homogeneous within the gas and liquid phase due to the relatively short demixing time and the considerable flow during this demixing, which would disturb any gradients in the concentration. Full thermal equilibrium will be established after the colloids and polymers have rearranged in the gravitational field, which takes days instead of hours.

We now monitor the macroscopic interface and study its properties from the initial formation until full sedimentation equilibrium has been reached. We will consider three separate cases: (i) the suspension height is close to the critical height $H \approx H_{crit}$, (ii) larger than the critical height $H > H_{crit}$, and (iii) smaller than the critical height $H < H_{crit}$.

(i) $\mathbf{H \approx H_{crit}}$

First we consider a tube of height $L = 25$ mm containing sample with overall colloid and polymer concentrations $\phi_c^0 = 0.052$ and $\phi_p^0 = 4.969$, observed over a period of 9 days - see figure 4.1. It is known from additional previous experiments that the suspension height is close to the critical height where the equilibrium density profile across the interface will

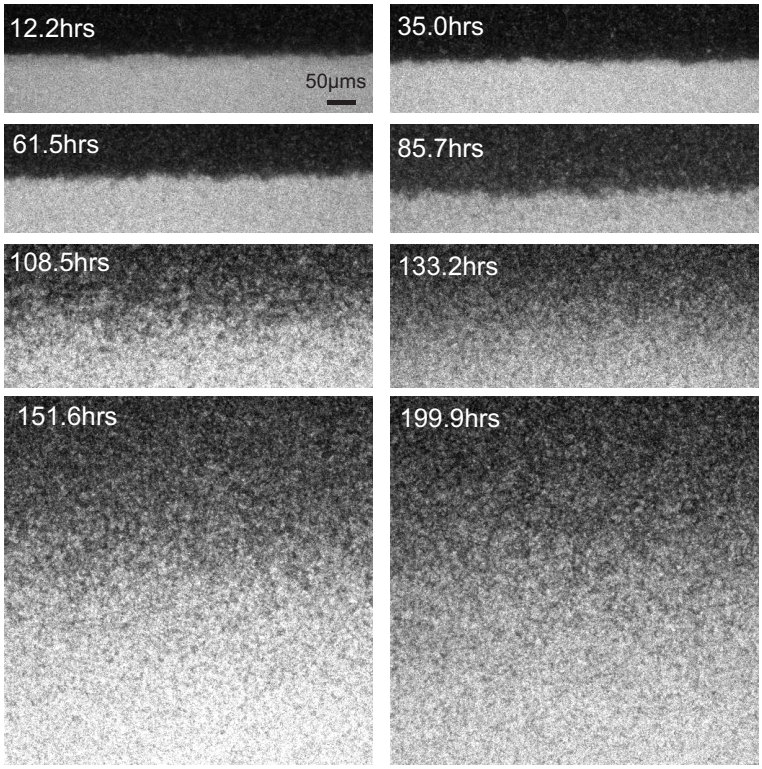


Figure 4.2: Images of the interface as it changes with time in a sample with $H > H_{crit}$, case (ii).

be continuous. Immediately after its formation, the interface is extremely sharp (figure 4.1, t=14.1hrs) and remains so as it slowly rises while all the liquid drops fall through the gas phase and coalesce with the bulk liquid. As time progresses and the sedimentation equilibrium settles in, the interface becomes increasingly diffuse and can barely be located. Note that the absolute height of the interface cannot be deduced from these images as the sample was carefully moved to follow the interface during equilibration. This applies to all the image sequences.

(ii) $\mathbf{H > H_{crit}}$

We now consider a sample with overall concentrations $\phi_c^0 = 0.052$ and $\phi_p^0 = 5.015$ sealed in a tube 18 mm high (figure 4.2). In this case the colloid concentration is a bit lower than in case (i) and the colloids have been synthesized in a different batch; it turns out that for this particular system the suspension height is greater than the critical height. Again we see that directly after its formation the interface is sharp and becomes increasingly diffuse during the

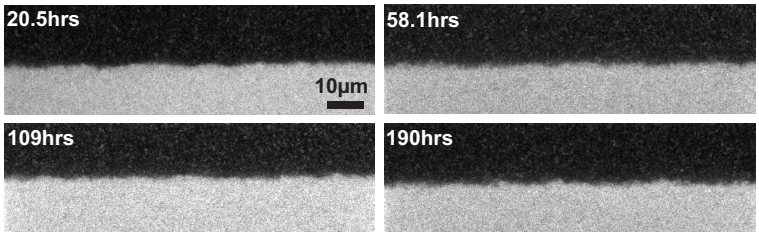


Figure 4.3: Images of the interface as it changes with time in a sample with $H < H_{crit}$, case (iii).

sedimentation process. After around 100 hrs it becomes very difficult to locate the position of the interface and after around 200 hours, at which equilibrium has been established, a smooth density gradient is clearly visible across the sample. No clear jump occurs across the interface.

(iii) H<$\mathbf{H_{crit}}$

Finally we consider a tube with height 10 mm containing sample with $\phi_c^0 = 0.055$ and $\phi_p^0 = 4.959$ (figure 4.3). Here the height of the tube is considerably smaller than the critical height and the interface is not appreciably affected. No changes are recorded over 200 hours.

The above picture is in qualitative agreement with our expectations - the system slowly reaches equilibrium, thereby following a pathway directed to the critical point whilst the interface is slowly sinking. Equilibrium is reached on a timescale of days, compared the initial phase separation process which takes place on a timescale of hours.

Let us now continue with a quantitative analysis of the observations. Figure 4.4 shows the change in the height of the interface (with respect to an arbitrarily defined starting point) during the final stages of phase separation and the subsequent sedimentation process. For all cases a similar behaviour is observed; the interface height initially rises as all of the liquid droplets coalesce with the bulk liquid phase and the interface appears sharp during this time. Subsequently, the interface drops as the colloids and the polymers rearrange under the influence of gravity, until a final position is gradually reached. For case (iii) there is no perceptible change in the interface roughness, but H is still considerably larger than ξ_c, and the interface position changes significantly but on a much smaller scale compared to the cases (i) and (ii). The extent of the displacement and kinetic pathway both depend sensitively on the overall concentrations and suspension height.

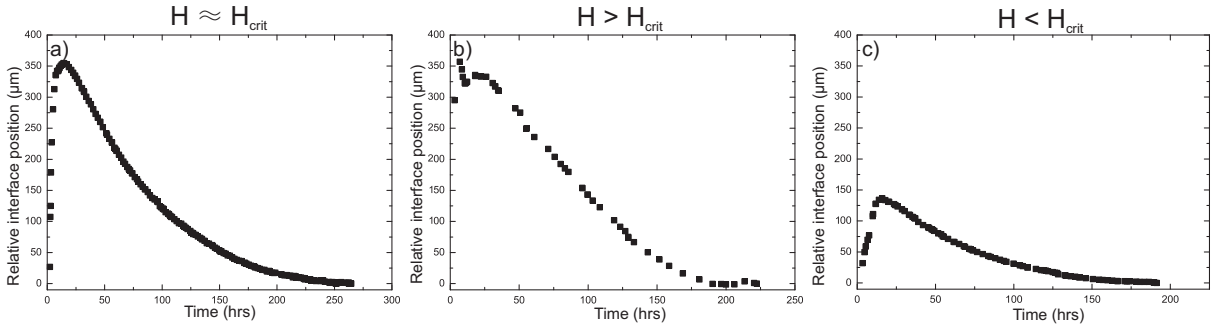


Figure 4.4: Interfacial height as a function of time relative to an arbitrary starting point for (a) case (i), (b) case (ii) and (c) case (iii).

The velocity with which the interface drops –obtained from the change in the interfacial height with time (figure 4.4), can be interpreted as follows; for case (i) the velocity around 50 hrs was measured to be 8.3 x $10^{-4}\mu$ms^{-1}, which is comparable to the sedimentation velocity of a single colloidal particle (with radius R_c), $u_s = m^*g/6\pi\eta R_c \sim 4$ x $10^{-4}\mu$ms^{-1}, where we set the viscosity η of either the liquid or gas phase to about 10 mPa s, in line with measurements on a nearby statepoint. Complicating factors due to the presence of the other colloids and polymers are ignored, but the sedimentation velocity seems to give a good indication of the interface displacement velocity. Note that the self-diffusion time of a colloid and polymer are expected to be of comparable magnitude due to their similar size, such that the polymers can easily respond to the sedimentation of the colloids.

We can further quantify the observations by analyzing the thermal capillary waves at the interface during sedimentation equilibration. The recording time takes around 25 minutes, during which the interface will sediment by about 1 μm, which is expected to have a small effect on the analysis. The interfacial width is obtained by fitting a hyperbolic tangent profile through an averaged intensity profile from a single confocal microscopy picture. Other methods, e.g. directly determining $\langle h^2 \rangle$, give qualitatively similar results but break down when fluctuations become considerable. For the cases (i) and (ii) (see figure 4.5 (a) and (b)), the interfacial width increases drastically, in agreement with the confocal laser scanning microscopy images. There is a strong increase in the amplitude of the fluctuations, which is consistent with the notion that the effective temperature of the system increases as the sed-

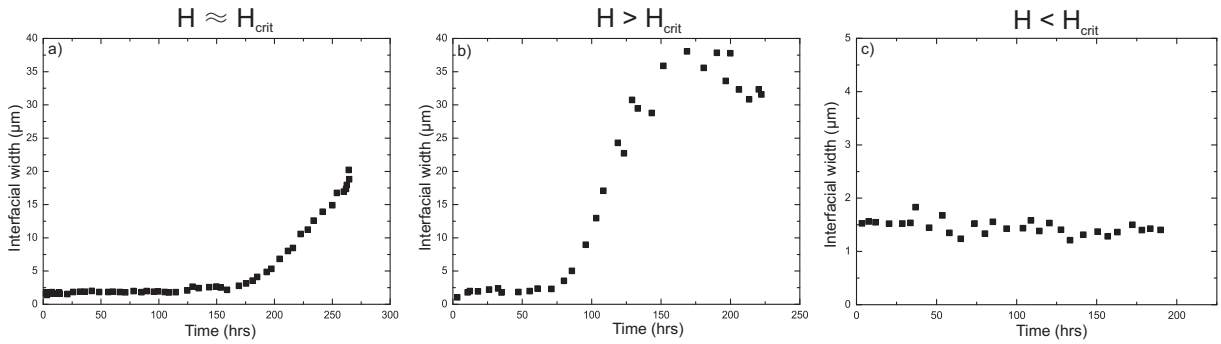


Figure 4.5: Interfacial roughness as a function of time for (a) case (i), (b) case (ii) and (c) case (iii).

imentation gradient is established. At the longest times the error in the roughness increases somewhat as the interface becomes very broad. For case (i) the data does not level off as in case (ii), indicating that the system has perhaps not reached full equilibrium, although the relative interface position seemed to have found its equilibrium value. For case (iii) we see that there is some scatter in the data, but no trend as a function of time.

We assume that during the sedimentation process the fluctuations can be described by capillary wave theory, i.e. the mean amplitude of each fluctuation is given by eqn. (2.2). We will discuss the assumption at a later stage. The changes of the interfacial parameters as a function of time are presented in figures 4.6, 4.7, and 4.8. We clearly see that for cases (i) and (ii) the interfacial tension decreases with time, in line with a slow increase of the effective temperature (or a decrease of the effective polymer volume fraction in the

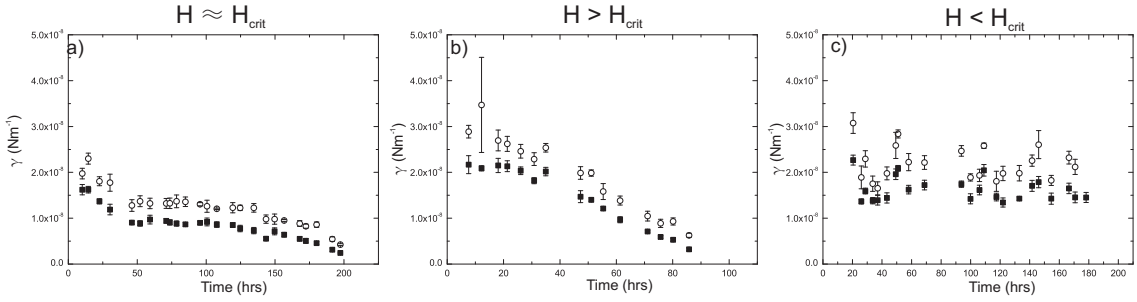


Figure 4.6: Interfacial tension as a function of time for (a) case (i), (b) case (ii) and (c) case (iii). The black squares denote the interfacial tension determined from the static correlation function, the open circles from the dynamic correlation function.

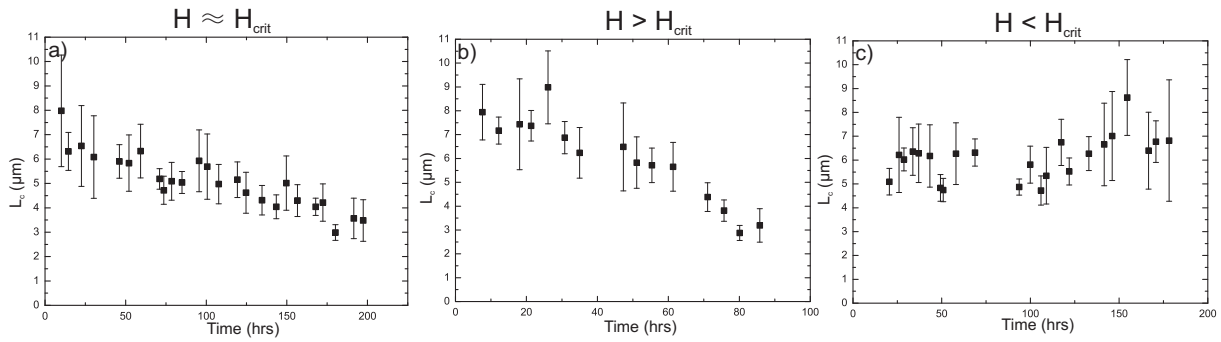


Figure 4.7: Capillary length as a function of time for (a) case (i), (b) case (ii) and (c) case (iii).

hypothetical reservoir). The interfacial tension derived from the dynamic correlation function yields systematically higher values than those derived from the static correlation function, although the overall trend is quite similar. The reason for the deviation is not entirely clear, but a similar effect has been observed in previous work [102]. Moreover, the dynamic analysis will be more sensitive to any slow time effects than the static one. We cannot follow the behaviour of the interfacial tension (either through the static or the dynamic route) all the way to full sedimentation-diffusion equilibrium; at some point in time the interfaces have become too broad and the fluctuation analysis is no longer reliable. For case (i) this happens close to the point where the interface finds its equilibrium position, for case (ii) this happens well before that. The situation, however, is different for case (iii). Here, the interfacial tension remains fairly constant over time (in line with the evolution of the interfacial roughness) although the displacement of the interface is clearly noticeable but small.

Both the capillary length (figure 4.7) and capillary time (figure 4.8) show behaviour consistent with an increase in effective temperature for the cases (i) and (ii), whereas not much is seen to happen in case (iii). The data sets for these parameters are noisier than those for the interfacial tension, especially at later times (cases (i) and (ii)), where the interfacial picture generally breaks down and the correlation functions are no longer adequately described by the theoretical expressions.

As mentioned above, we make the assumption that capillary wave theory can be applied during the sedimentation process. The key equation, eqn. (2.2) can be derived using me-

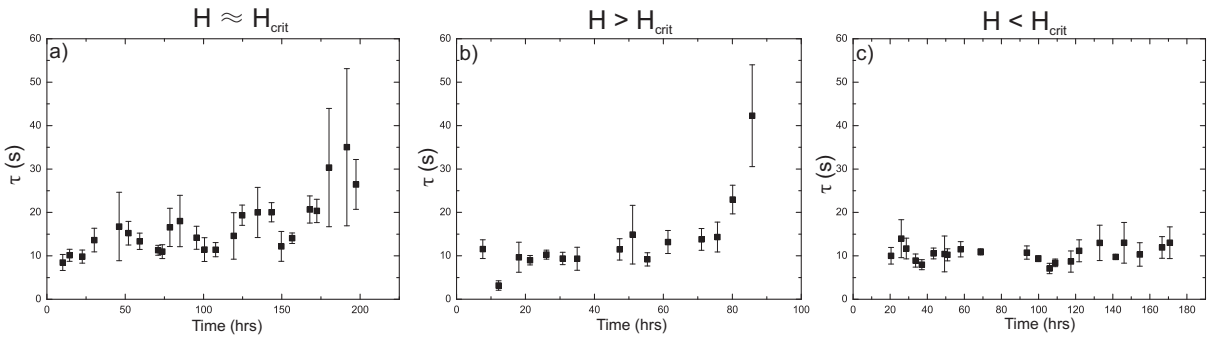


Figure 4.8: Capillary time as a function of time for (a) case (i), (b) case (ii) and (c) case (iii).

chanical and statistical mechanical arguments. Mechanically, the gravitational penalty for displacing matter against gravity and the interfacial penalty for increasing the interfacial area are taken into account for each fluctuation-mode. Statistically, one then invokes the equipartition theorem stating that the work needed to create each mode equals $k_BT/2$. This means that during the time of a single measurement the system should be in local equilibrium, both mechanically and thermally, for capillary wave theory to apply. Obviously, the effective temperature associated with the amplitude of the depletion attraction changes in the course of a measurement, however, the real temperature responsible and hence the thermal energy k_BT does not change. The assumption of mechanical equilibrium is supported by the fact that the theoretical expressions for the correlation functions describe the experimental correlation functions quite nicely, especially when fluctuations are not too large. This is in line with the very small changes expected during the relatively short recording time.

The idea of having a local, mechanical equilibrium (which only changes very slowly with time) is in agreement with observations of the gas-liquid meniscus close to the vertical front glass wall. Close to the wall the profile of the meniscus is defined by the balance between the Laplace and hydrostatic pressures, which again follows from mechanical equilibrium. The governing length-scale is the capillary length [109], which in principle can be measured from the exact shape of the profile as shown in experiments on a different set of colloid-polymer mixtures [16, 51]. Here, we observe that the capillary length indeed decreases as a function of time, although it is difficult to fit the profiles accurately, since the capillary length is quite small, the interface fluctuations are large and the microscope resolution in this direction is

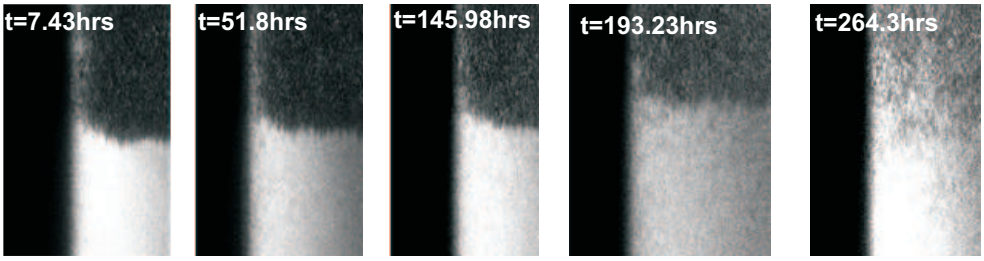


Figure 4.9: CSLM images of the gas-liquid meniscus close to the container wall, $H \approx H_{crit}$, case (i).

poor. But the mere presence of a curved meniscus and its slow change with time does point to the presence of local, mechanical equilibrium.

4.5 Conclusion

We have shown how an initially homogeneous gas-liquid phase separated colloid-polymer mixture finds its full sedimentation-diffusion equilibrium in Earth's gravitational field. Three different cases have been presented. In case (i) the suspension height H was close to the critical height $H_{\rm crit}$, such that in full equilibrium the colloidal gas-colloidal liquid interface would just disappear. In case (ii) H was well above $H_{\rm crit}$ and in equilibrium there would be a continuously varying density gradient. Finally, in case (iii) the suspension height was relatively small, such that gravity would only play a minor role. After phase separation had completed all three cases had a similar starting point: a colloidal liquid phase in coexistence with a colloidal gas phase, with density gradients yet to be established. We show that the sedimentation of the colloids in a colloid-polymer mixture always leads to an increase of the effective temperature of the mixture due to a reduction of the amplitude of the depletion potential between the colloids. In this study we have followed the kinetic pathway of the sedimentation process as the systems goes from low to high effective temperature.

The three cases showed that the interface remained in local mechanical and thermal equilibrium during the sedimentation process and we applied capillary wave theory to measure the interfacial parameters. For the cases (i) and (ii) the interfacial tension gradually decreased until the fluctuations could no longer be analysed. For case (iii) the effective temperature

change was rather small and no clear differences were seen for the interfacial tension. The other interfacial parameters were in agreement with this picture. Close to a vertical wall a similar pattern was observed and the height of the meniscus was seen to decrease during equilibration.

It thus seems that we effectively scan the phase diagram during sedimentation equilibration and that we can bring the system far into the one-phase region, but the system's response is very slow. Furthermore, the previously established connection between suspension height and the critical point [102] also affects the present observations. We are in the unique position where gravity drives the system towards criticality, although ultimately, it will also be limited by it, see for example the review by Moldover *et al.* [110] and the work specifically discussing capillary waves in a gravitational field by Sengers and Van Leeuwen [111].

The present approach may be of further use in studies dealing with the universality class of colloid-polymer mixtures. In both simulations and theory it has been shown that the system belongs to the 3 dimensional Ising universality class if the polymer reservoir concentration is taken as a control parameter [98,112–115]. In a range of experiments, renormalized exponents have been found when the colloid volume fraction was used as the control parameter [96,116]. Other behaviour has been found as well [94, 95, 97], and the extent of the critical region has recently been explored [99], possibly illustrating the need for further experiments, in which the presented approach may be useful. However, the precise determination of $H_{\rm crit}$, the dependency of $H_{\rm crit}$ on the exact starting concentrations, the sensitivity of the experiment to external noise and the long inherent times involved may be a limiting factor.

Finally, we qualitatively understand the system moves from a low effective temperature to a higher one through a series of local equilibria, and we observe the governing timescale for this process to be closely related to the sedimentation velocity of the colloids. However, a fully quantitative and microscopic theoretical description of the sedimentation process is still lacking. To this end, computer simulations or the recently developed dynamic density functional theory [117, 118] could be invoked in an attempt to provide a more in-depth description of the experimental observations.

Acknowledgments Once again we thank Rik Wensink for his contribution to the theory section of this chapter.

Chapter 5

Tuning the demixing of colloid-polymer systems through the dispersing solvent

ABSTRACT

We report measurements on fluid-fluid phase separation in a colloid-polymer mixture by means of confocal scanning laser microscopy and we show that we can access the various coarsening regimes by tuning the properties of the solvent. By increasing the viscosity of the solvent we are able to access the diffusive-hydrodynamic regime of spinodal decomposition. By matching the density of the solvent and colloids we are able to grow structures to large length scales before they are destroyed by buoyancy forces. Tuning the solvent's density furthermore gives control over which phase flows up and down, illustrating the flexibility of this particular system.

5.1 Introduction

Fluid-fluid demixing, which e.g. occurs when shaking a flask of balsamic oil and vinegar, displays a rich dynamics of patterns. The initial thermodynamic instability, taking place at the microscopic scale, is followed by what are essentially mechanical instabilities. These may lead to macroscopic patterns, and ultimately two (bulk) phases are formed separated by an interface. Here we will focus on spinodal decomposition, which occurs whenever the phase

separation starts from the unstable part of the phase diagram, as opposed to nucleation and growth, which starts from the metastable part [24,119]. The demixing is such a generic process that the phenomenology has been observed for example in binary fluid mixtures [120], metal alloys [121,122], complex plasmas [123], polymer-polymer mixtures [124–126], colloid-polymer mixtures [7,127], foods [128], etc.

In this chapter we shall study the phase separation process in our colloid-polymer mixture, where the depletion interaction may drive phase separation into the colloidal gas, liquid and crystal phases [32,33]. The phase behaviour was first calculated by Gast *et al.* [34,35] and Vincent *et al.* [36,37], who identified that the topology of the phase diagram depends on the polymer-to-colloid size ratio. However, the polymer partitioning between the phases was not taken into account. This was first realized by Lekkerkerker and colleagues [38,41] in what has become known as the free volume theory: a physically insightful, flexible and powerful approach that has been validated in extensive computer simulations and different theoretical methods, see for example the recent review by Tuinier and Fleer [129] and references therein.

We will focus on fluid-fluid phase separation into the colloidal liquid and colloidal gas phases. The different regimes in the demixing process will be introduced in more detail in the next section, but the demixing can roughly be divided in an early initial stage, where the most unstable wavelength develops without actually coarsening, the so-called linear Cahn-Hilliard regime (LCH) [130]. This is followed by a diffusive regime where the typical lengthscale L coarsens as time t^{α}, with the coarsening exponent $\alpha \sim 1/3$ followed by a viscous-hydrodynamic regime with $\alpha = 1$ [78] (this depends to some extent on the role of hydrodynamics [119]). This may finally be followed by an inertial regime [119,131], or it may be cut-off by gravity driven flow [78]. Note that the precise values of the growth exponent α may depend on the precise role of hydrodynamic interactions [25].

If one is not too close to the critical point one may expect that the lengthscale developing in the early initial stage is only a few particle diameters large [7]. A colloidal particle with radius $R_c = 100$ nm will only take a few milliseconds to diffuse over its own diameter in a low viscosity liquid such as water and very handwavingly one may expect that the linear Cahn-Hilliard regime is then rather short. Similarly, one may expect that for sharp interfaces to form colloids will have to diffuse over only a few times their particle diameters as well,

such that this regime may also be quite short. We have used this as a rationale for previous observations where we observed the viscous hydrodynamic regime in the phase separation process, but not the preceding regimes: the time between homogenization and start of the microscopy measurements was long enough for these regimes to have passed [7]. If this view is correct one should be able to tune the actual (not the physical) timescale of these regimes by increasing the viscosity of the dispersing liquid, which is the approach we will follow here. The physical timescale, which is related to the physical process taking place and which introduces a reduced or dimensionless time, remains unchanged (for example, the colloid self-diffusion time is $\sim R_c^2/6D$, irrespective of the absolute value of the viscosity).

We will furthermore focus on the onset of gravity driven flow [78], for which the governing lengthscale is the capillary length $L_c = \sqrt{\gamma/\Delta\rho g}$. This can be tuned either through the interfacial tension or the density difference, which are both a function of the statepoint. The density difference represents the difference in mass between the two phases, which also depends on the density of the solvent. We will show that varying the solvent density changes the onset of the gravity driven flow regime.

We structure this chapter as follows; in section 5.2 we will introduce the relevant length- and timescales behind the phase separation process. The next section (section 5.3), will describe the experimental system and method, followed by the results and discussion (section 5.4). We will conclude in section 5.5, where we compare our findings to related experiments.

5.2 Theory

When a colloid-polymer mixture is quenched into the unstable region of the phase diagram the initial phase behaviour is determined by the free energy landscape. At this early stage, the relative density changes and the gradients in the density across the system are small [25]. Density fluctuations with large wavelengths lead to a reduction in the free energy of the system and thus are thermodynamically more favorable, whereas those with smaller wavelengths are kinetically favorable as the particles only have to travel shorter distances. As predicted by Cahn [132] this leads to a fastest growing mode q_m within the system, where

the wavelength $L = 2\pi/q_m$ associated with this fluctuation is calculated to be a few times the colloidal diameter σ in a colloid-polymer mixture not too close to the critical point using a squared-gradient approach [7]. This initial stage is known as the 'Linear Cahn-Hilliard' (LCH) regime.

As the density fluctuations across the system become larger, the system continues to be driven by gradients in the chemical potential. The compositions of the two phases approach their equilibrium constituencies and the correlation length L grows in the diffusive regime as [78]:

$$L = \left(\frac{k_b T}{\eta} t\right)^{1/3}, \tag{5.1}$$

where η is the viscosity and $\alpha = 1/3$.

When sharp interfaces are formed, the phase separation becomes driven by interfacial tension γ. The minimisation of the interfacial area of the domains will drive internal viscous flow, and the dynamics are described by the Navier-Stokes equations. At low Reynold's number the balance between the Laplace pressure and viscous forces drives the system to coarsen in the linear regime ($\alpha = 1$) as [78]:

$$L \propto \frac{\gamma}{\eta} t. \tag{5.2}$$

When the lengthscale of the spinodal structures grow to a size comparable to the capillary length in the system, the domains will be destroyed by buoyancy forces and the separation crosses into the gravity driven regime [78]. The heavier phase will sediment to the bottom of the suspension in vertical lanes, the phase which breaks up depends on the relative volumes and viscosities of the phases, as shown by Onuki [76]. Dependant on the density difference between the phases, the appearance of the flow may bear similarity to the Rayleigh Taylor instability [7, 133, 134].

By tuning the properties of the solvent in the system, it is possible to change the time and lengthscales associated with each of the regimes in spinodal decomposition. If we increase the solvent viscosity we should be able to slow down the phase separation, allowing us to increase the time spent in the diffusive regime before a crossover to linear coarsening. If densities of the solvent and colloids are matched, we should be able to grow large spinodal structures before the domains are ripped apart by gravity. Below we will explore these ideas.

5.3 Experimental system and method

Stock solutions of PMMA colloids and xanthan polymer dispersed in water were prepared as described in chapter 2. This system based entirely in a water solvent was used to prepare sample 1 (see table 5.1), which is at a statepoint relatively close to the critical isochore. The solvent of the stock colloid solution was then converted to a solution of approximately 23% water and 77% glycerol by repeated centrifugation. Colloidal suspensions dispersed almost entirely in glycerol were found to be unstable at long times and high concentrations. We can tune the state point, solvent viscosity and relative densities in the system by mixing together stock colloids, xanthan, glycerol and water in different quantities. The radii of the colloids in the new solvent mixtures were remeasured using DLS as non-cross-linked PMMA particles are prone to swelling [136], however no significant changes were observed. An investigation into changes in the radius of gyration of the polymer proved inconclusive, but no large effect was expected. By increasing the ratio of glycerol to water in the solvent we altered the positions of both the spinodal and binodal of the phase diagram; full phase diagrams were not produced for these new systems due to the long timescales associated with their phase separation. We found that increasing the ratio of glycerol decreased the amount of liquid phase, generally lowered the interfacial tension in the system and moved the binodal towards the lower left hand corner of the phase diagram. The refractive index mismatch between the PMMA colloids and the solvent also was reduced, which changed the scattering properties of the colloids and thus the appearance of the system under the microscope. The following samples, summarized in the table above, were prepared and allowed to equilibrate for at least 3 days in their new solvents.

Sample	ϕ_c	ϕ_p	Glycerol:water ratio of solvent	Estimated $\Delta\rho_{colloid-solvent}$ (g/cm^3)	Estimated $\eta_{solvent}$ (cP) [135]
1	0.118	2.456	0:100	0.175	1
2	0.065	1.904	80:20	-0.027	60
3	0.079	3.005	69:31	0.008	22

Table 5.1: Sample details

The samples were homogenised by vortexing and the long-time phase separations were recorded in real space using CSLM in the direction parallel to gravity using a 10x magnification lens. The system was homogenised carefully in small volumes, and allowed to phase separate in glass containers of dimensions designed to minimise solvent flow but not confine the system. The homogenisation process could cause the formation of air bubbles in the solvent, particularly in systems of high glycerol content. These would rip apart the spinodal structure and break up the network into droplets. In addition, any flow of the solvent during phase separation will distort the domains, destroying the symmetry of the phase separation. The initial stages of the phase separations were also observed under 63x magnification perpendicular to gravity in a drop pipetted onto a glass coverslip.

The coarsening rate of the system was determined by performing 2-dimensional discrete Fourier transforms (FFT) on the CLSM images, as described in [125] and [7]. The Fourier transforms were radially averaged to obtain the structure factor $I(k,t)$, where I is the intensity of the image and k is the wavevector. The wavevector at the maximum intensity $I_{max} \equiv I(k_{max},t)$ was obtained fitting a Gaussian curve to the data. The correlation length in the system corresponds to $L = L_{image}/k_{max}$ where L_{image} is the image width and the coarsening rate in the system was obtained by plotting L against time.

5.4 Results and discussion

In figure 5.1 we show the phase separation of sample 1, a PMMA-xanthan-water system. We observe the distinctive bi-continuous spinodal structure (5s) which immediately coarsens (29s). Once the domains grow to a size comparable to the capillary length in the system

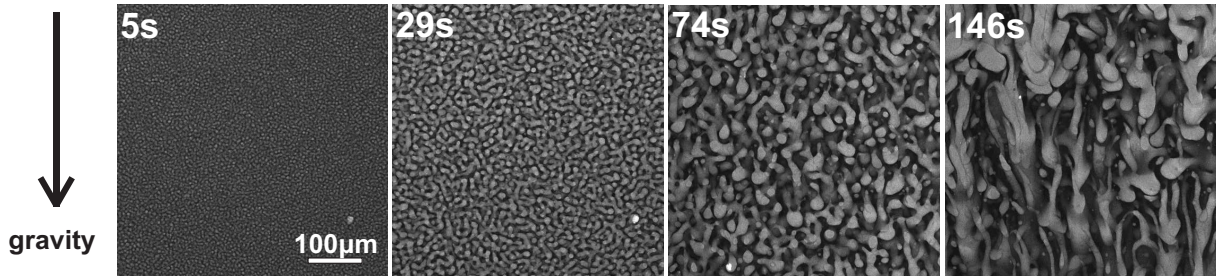


Figure 5.1: CSLM images of the phase separation of sample 1: lowest viscosity solvent.

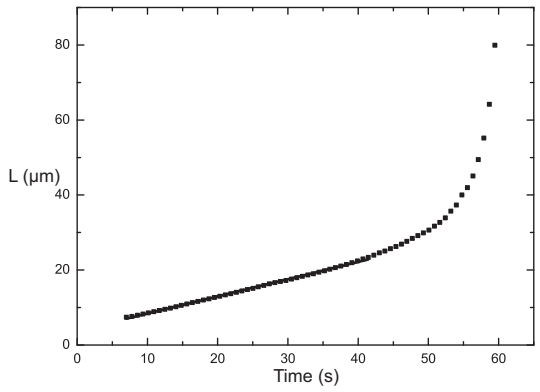


Figure 5.2: Characteristic lengthscale L vs time for sample 1. The full line represents a linear fit to the data between 7 and 42s.

the structure begins to collapse under its own weight (74s), and by the final image (146s) the system has entered the gravity driven regime. The heavier liquid phase sediments downwards and mushroom-like heads form as the density difference between the phases leads to a Rayleigh-Taylor like instability. The coarsening rate of the system (figure 5.2) is obtained from the CSLM images in figure 5.1. By the first image, the interfaces are already sharp and the spinodal network has formed. In a sample with a low-viscosity solvent, it can be calculated that the diffusive regime is completed within less than a second and is therefore not accessible in this instance. The system coarsens in the linear regime from the start of the data recording (corresponding to figure 5.1, 5s and 29s), and a linear fit is performed on the data. After around 40s the spinodal structure begins to collapse under gravity (figure 5.1, 74s and 146s) and the lengthscale diverges due to the break in symmetry. The prefactor of eqn. (5.2) is found to be of the order of 1, which is comparable to the value found in [7].

We now consider the second sample, where we raise the viscosity of the solvent to allow us to observe early time regimes - see figure 5.3. Growth in the diffusive regime is inversely proportional to $\eta^{1/3}$, thus we expect an increase in the viscosity to have a dramatic effect on the timescale of the phase separation. The change in the viscosity of the homogenised mixture may be quite substantial, since the viscosity of the solvent has already increased by a factor of 60. Again we see that the system decomposes with a spinodal morphology (5242s), although the interfaces are extremely diffuse, even at later times (43250s). The

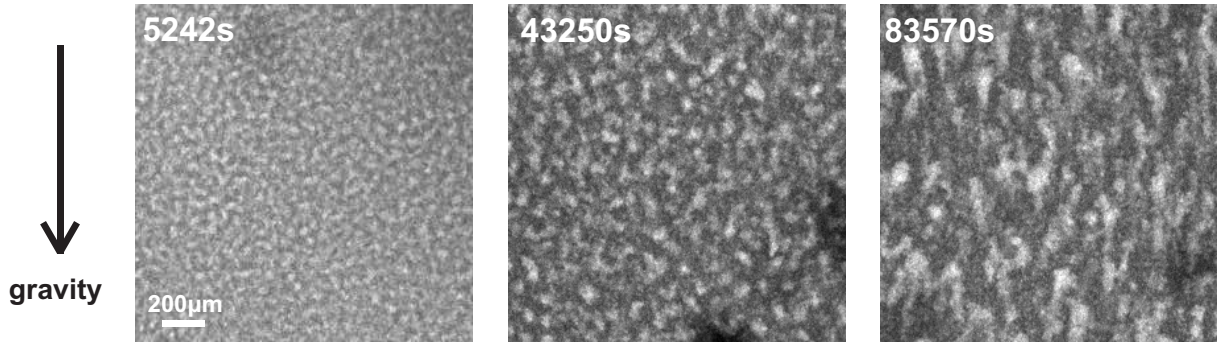


Figure 5.3: CSLM images of the phase separation of sample 2: highest viscosity solvent.

colloids are now less dense than the solvent, consequently during the gravity driven regime, the colloid rich liquid phase unusually sediments upwards (83570s). The liquid phase at this state point is very much in the minority so breaks up. The relative density between the phases is now smaller and there is not such a clear Rayleigh-Taylor effect.

A plot of L vs time for this sample clearly shows the existence of a non-linear regime at early times (figure 5.4 (a).) A plot of L vs $t^{1/3}$ (figure 5.4 (b)) yields a straight line for around 27000s indicating that coarsening progresses with the power law $L \propto t^{1/3}$. The gradient of this fitted line (6.3 x 10^{-7}) is very close to the prefactor predicted by eqn. 5.1, $(k_B T/\eta)^{1/3}$ = 4.1 x 10^{-7} ms$^{-1/3}$. Here we use the estimated solvent viscosity for the value of η, the correct choice of viscosity value is a subject currently under discussion. The system crosses over to the linear regime for a short time (around 10000s) however this is not clearly established before L diverges as gravity makes the spinodal structures collapse. The

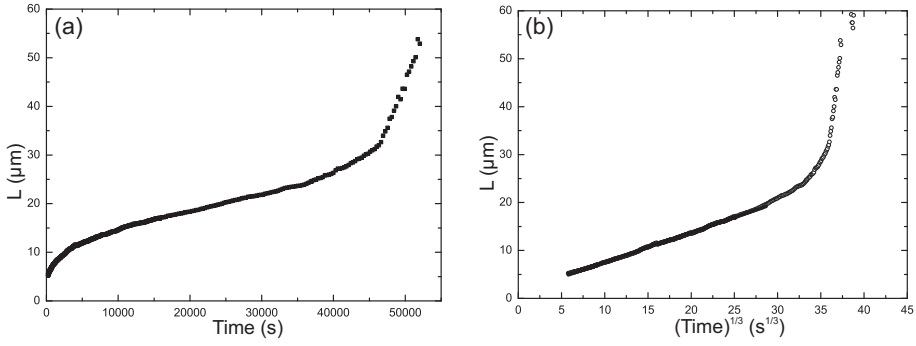


Figure 5.4: (a) Characteristic length scale L vs time for sample 2, (b) Characteristic length scale L vs $t^{1/3}$ for sample 2

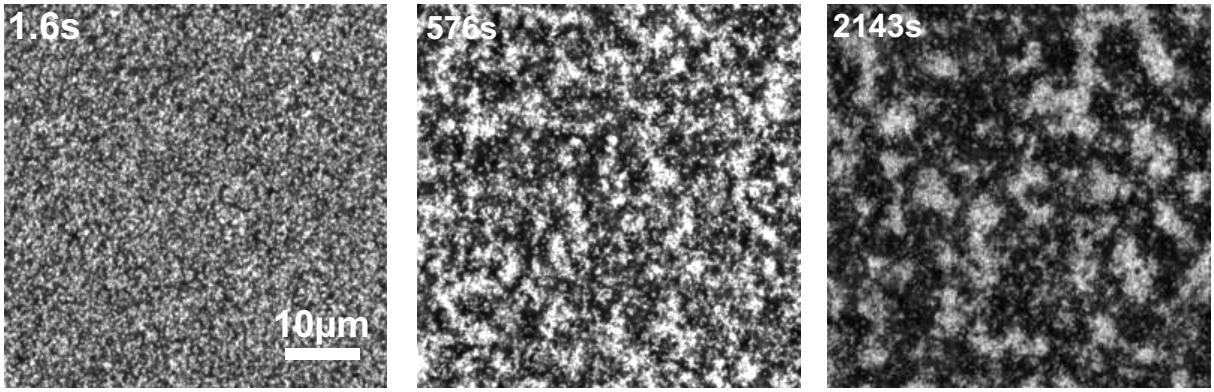


Figure 5.5: CSLM images of the early time phase separation of sample 2 at high magnification.

extremely diffuse interfaces observed in figure 5.3 are expected as equilibrium concentrations in the liquid and gas phases are not formed until the end of the diffusive regime. The change of solvent to glycerol is observed to reduce the interfacial tension in the system and thus the interfaces appear rough even as the structures are ripped apart by gravity.

Figure 5.5 shows the phase separation of sample 2 at very early times using a 63x magnification lens. The colloids are slightly smaller than the resolution of the microscope. The first image shows a reasonably well homogenised sample however there is still some structure present. We see the system coarsens, and distinct domains form. The images are analysed using a 2 dimensional FFT as previously - in figure 5.6 (a) we present a plot of L vs t. The data is taken over such a short time interval that the curvature expected from the

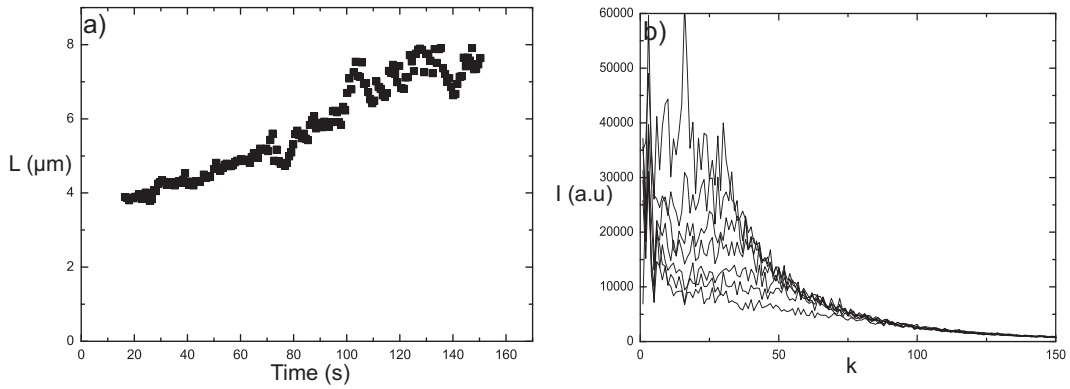


Figure 5.6: (a) Characteristic length scale L against time at early times for sample 2. (b) Structure factors at 1.6s, 5.4s, 10.1s, 20.4s, 30.5s, 60.2s and 140s.

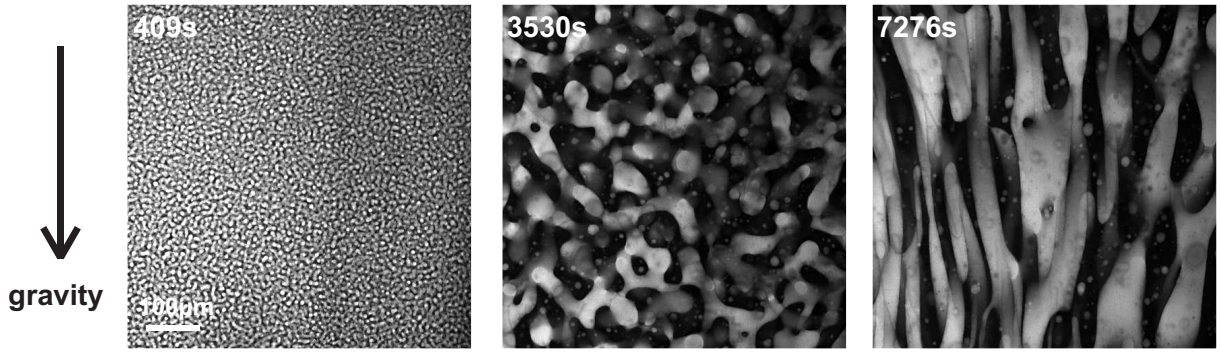


Figure 5.7: CSLM images of the phase separation of sample 3: solvent and colloids are approximately density matched.

$t^{1/3}$ power law is very small, and the plot appears linear. The structure factors (5.6 (b)) are extremely broad, consequently it is difficult to precisely define the position of k_{max} and therefore L, particularly in the very initial stages. It is not clear if we are able to access the linear Cahn-Hilliard regime, in any case the initial shearing effects in the sample due to homogenisation and injecting the sample onto the slide may well distort the phase separation at small lengthscales. It is suggested that for these reasons the width of the structure factors is unexpectedly large. The emerging wavevector corresponds to a wavelength of around 18 particle diameters; such lengthscales during this regime have been previously documented in [128] and indicate that we are in close proximity to the critical point. The FFT analysis becomes unreliable after around 140s as the small field of view of the 63x lens leads to a lack of resolution in the structure factor at small wavevectors.

For sample 3, we minimise the density difference between colloids and the solvent, greatly increasing the capillary length in the system. We continue to observe coarsening via spinodal decomposition (figure 5.7 409s), but the structures are able to grow to an increased size (3530s) before they collapse under the effects of gravity. It is observed that during the gravity driven regime (in this case the liquid still sediments downwards) neither phase forms the mushroom-like heads characteristic of the Rayleigh-Taylor instability, as the densities of the two phases are very similar.

The results from the FFT analysis are quantified in figure 5.8. The spinodal structures are observed to coarsen in the linear regime - the viscosity of the solvent is not sufficient to access the diffusive regime. The discontinuities in the data occur when the microscope

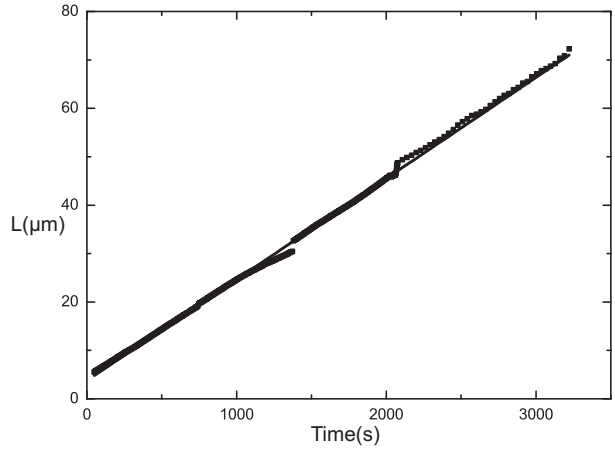


Figure 5.8: Characteristic length scale L against time for sample 3. The full line represents a linear fit to the full dataset.

is refocussed during the phase separation. After the sample reaches around 75 μm in size it is no longer possible to analyse the structures using the FFT analysis due to the lack of resolution at small wavevectors. It can be deduced by eye that the structures continue to coarsen a little further and then collapse under gravity. Due to scattering it is not possible to image deep into the sample, thus it is possible that at large lengthscales the presence of the wall may affect the coarsening of this sample.

The growth of such symmetrical networks suggests that the coarsening of the domains in all samples undergoing spinodal decomposition can be described by a single lengthscale (in this case L) and it has been predicted by Binder and Schauffer [73] that the structure factor should scale dynamically as: $I(k,t) = k_{max}^{-3} F(k/k_{max})$ where F is a universal scaling function. There is some difficulty in the practical application of this theory; following the treatment explained by Verhaegh [127], dynamic scaling has been experimentally observed in the demixing of colloid-polymer mixtures using light scattering [127, 128] and in real space [7]. The shapes of the scaling functions are described by Furukawa's theory [137] for critical mixtures:

$$I = I_{max} \left(\frac{4(k/k_{max})^2}{3 + (k/k_{max})^8} \right), \tag{5.3}$$

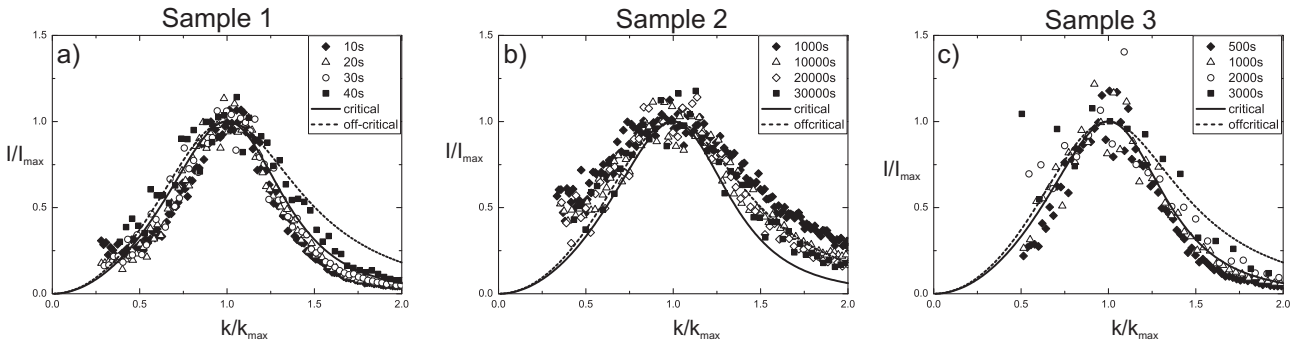


Figure 5.9: Dynamical scaling of the structure factor for each sample. The scatterplots represent experimental data at the stated times, and the full and dashed lines denote scaling functions for critical and off-critical demixing as proposed by Furukawa. [137]

and off-critical mixtures:

$$I = I_{max}\left(\frac{3(k/k_{max})^2}{2+(k/k_{max})^6}\right). \tag{5.4}$$

The structure factors for each sample are dynamically scaled in figure 5.9. For sample 1 we see the structure factors collapse onto a curve well described by Furukawa's critical scaling function. Sample 3 (figure 5.9(c)) also scales to the function for critical demixing; the curve is broad due to noise in the data. The lack of resolution in the structure factor at small wavevectors is magnified in the dynamical scaling as the domains become large. Finally we consider sample 2 (figure 5.9 (b)) where we access early time regimes. The scaled curves are too broad at early times, but the scaling improves as time progresses, and by around 20000s the scaled curves are well described by the off-critical function. It is unsurprising that this sample follows the prediction for off-critical demixing as there is a very low liquid content at this statepoint. It is speculated that the lack of dynamic scaling could to be due to the fact that the equilibrium concentrations of components are not well established in the initial stages [138].

5.5 Conclusion

We have shown that we can access the various regimes in the spinodal decomposition of a colloid-polymer mixture by tuning the properties of the dispersing solvent, in particular its

viscosity and density. By increasing the viscosity we are able to observe the initial stage of spinodal decomposition, where the system coarsens in the diffusive hydrodynamic regime with $\alpha \sim 1/3$. We do not observe the linear Cahn-Hilliard regime (LCH, $\alpha = 0$), despite having slowed down the system so drastically and having large initial lengths. The linear Cahn-Hilliard regime has been observed by Bhat *et al.* in a mixture of casein micelles (acting as the colloids) and xanthan polymer in water [128], very similar to the xanthan used in this work. The authors speculate that their observation of the LCH regime may partially be due to the screening of hydrodynamic interactions by the polymers, with the underlying thought that the polymers form a network at these high polymer concentrations. However, they also note that in similar experiments on colloidal teflon spheres and xanthan polymer in water no evidence of the LCH regime had been found [71]. Bhat *et al.* further indicate that the observation of this regime may be due to the high polydispersity and low surface charge of the casein micelles or the low density mismatch between the colloids and the solvent. In this work, where the density difference is very small, and in experiments done at the International Space Station (ISS), where gravitational effects are extremely small, the LCH regime is not observed [138]. We thus believe that a microscopic explanation, such as the surface charge or the polydispersity, may be the reason for the absence/presence of the LCH regime. This is something which may be easier to explore in simulations. Furthermore, the distance to the critical point must play a role here as well.

By tuning the density mismatch we observe that the gravity driven flow regime can be postponed considerably, such that we can follow the scaling regimes for almost four decades in time, which becomes comparable to experiments performed on the International Space Station [138]. Previous work by Beysens *et al.* had already shown that density matching can reproduce experiments performed in microgravity [139–141]. In line with recent experiments on colloid-polymer mixtures made at the ISS, and with earlier experiments on density matched binary liquids [141], the crossover from the diffusive hydrodynamic to the linear growth regime seems very slow. Although at low and intermediate viscosities the diffusive hydrodynamic regime has not been detected, the linear growth regime can still be followed over three decades in time. Moreover, we can tune the buoyancy such that the colloidal rich phase can either be at the bottom or at the top of the cell. This feature will

turn useful when studying fluctuations at wetting layers (see [142] and chapter 6), since a standard inverted laser scanning microscopy setup can be used. Furthermore, the capillary length, which is the parallel correlation length of the height-height interface fluctuations, can be systematically varied and confined, and insights into the intrinsic profile might thus be obtained [143].

Acknowledgment: It is our pleasure to thank Peter Holmqvist for performing dynamic light scattering experiments on our dispersions.

Chapter 6

Surface effects on the demixing of colloid-polymer systems

ABSTRACT

We study the effect of a solid surface upon the fluid-fluid phase separation of a colloid-polymer mixture in real space, exploring demixing from both the unstable and metastable regions of the phase diagram. The presence of wall breaks the symmetry of the phase separation morphology in the direction perpendicular to the surface, influencing the coarsening behaviour of domains. We analyse the thickening of the wetting layer, and demonstrate that hydrodynamic transport processes can significantly increase the rate of wetting layer growth. We also discuss the effect of a crossover in the demixing regime of bulk domains upon the growth of this layer. To our knowledge, these observations are the first in colloid-polymer mixtures, and we compare our findings to previous results from experiment and simulation.

6.1 Introduction

The demixing of fluids has been extensively studied by both experimentalists and theoreticians for the past four decades. The decomposition of a homogenised mixture leads to the development of complex patterns, which coarsen as the system moves towards equilibrium. If these fluids are brought in the vicinity of a solid wall, it is likely that the surface will have a preference for one of the phases over the other, leading to a build up of a layer of

the preferred phase on the surface. On equilibration the strength of the interactions between the fluid phases and the surface are characterised by the contact angle between the fluid-fluid interface and the wall [109]. When an unstable mixture decomposes in contact with a wetting surface, two different processes occur: bulk phase separation and wetting layer growth. The surface field can have a dramatic effect on the evolving morphology [144], and results in different coarsening behaviour in the directions parallel and perpendicular to the wall, breaking the symmetry of the phase separation [145–147]. This phenomenon is known as surface directed spinodal decomposition (SDSD), and is of considerable interest as a demixing sample shall never be entirely free of surface effects, for example due to the walls of its container, or its interface with air.

6.2 Background

The morphology and dynamics of bulk phase separation, which occurs when a system is quenched into the unstable or metastable regions of its phase diagram is already well established. There are two differing methods of decomposition: generally a system demixing from the unstable region will exhibit a spinodal network morphology, whereas a quench from the metastable region will lead to demixing via the nucleation and growth mechanism [24]. The two regions are separated by the spinodal, the exact position of which can be difficult to locate [148]. The dynamics of phase separation can be characterised by growth of domains of size L, described by power laws of the form $L(t) \sim t^{\alpha}$. The growth exponent α, differs depending on the coarsening regime.

In the very early stages of spinodal decomposition, density fluctuations are governed by the free energy landscape; the most unstable wavelength grows in amplitude without actually coarsening in what is known as the Linear Cahn-Hilliard regime [24, 130]. This is followed firstly by a diffusive regime where $\alpha \sim 1/3$, then a viscous hydrodynamic regime where $\alpha = 1$ [78]. This may be followed by an inertial regime [131], or the effect of buoyancy forces may rip apart the network structure and the system will continue to separate driven by gravity [78]. The exact growth exponents may depend on the precise role of hydrodynamic interactions [25]. The condition for a bicontinuous network has been derived by Onuki [76]

to be $\phi_1/\eta_1 \sim \phi_2/\eta_2$, where ϕ and η are the volume fractions and viscosities of the two components respectively. Should this condition be violated as the decomposition progresses, interconnecting tubes in the spinodal network may disconnect; the phase which breaks into droplets is determined by the relative viscosities and volume fractions in the system. A more detailed theoretical description of spinodal decomposition is provided in the previous chapter.

A system quenched into the metastable region of the phase diagram shall demix via the nucleation and growth of droplets or bubbles of the minority phase. Once again the initial stages of coarsening are determined by the free energy landscape, however only density fluctuations of sufficient size will be energetically favourable. The low probability of a suitably high amplitude fluctuations leads to an induction time before phase separation commences [24]. Once nuclei of the minority phase form, they can then coarsen by coalescence [73] or Ostwald ripening [74]. The growth of droplets is characterised by the exponent $\alpha \sim 1/3$ known as the Lifshitz-Slyozov (L-S) growth law [74], until buoyancy forces become dominant, and the separation becomes gravity driven [78].

During the phase separation process, the preferential attraction of one of the phases to a solid wall can cause a significant alteration of the phase separation morphology and dynamics [144]. There is no theoretical framework for the evolution of complex patterns and domain growth of a system undergoing SDSD as for the bulk, however there has been considerable progress in experiments and simulations, see for example the reviews by Geoghegan and Krausch [149], and Puri [150]. Previous results have proved dependent on specificities of the system studied, for example the relevance of hydrodynamics, quench depth, as well as the range and depth of the attraction of the surface field, which characterises the interaction between the fluids and the surface.

It has been well established that should a two phase system demix in contact with a wetting surface, this surface shall become the origin of an oscillating density wave which propagates perpendicular to the surface into the bulk, breaking the symmetry of the domains [145]. These waves were extensively explored experimentally in the early 90s in polymer blends [145, 151] and via simulation [146, 152, 153]. For fluid-fluid phase separations this morphology consists of a wetting layer of the preferred phase on the surface, then a further

(depletion) layer of the non preferred phase [154], possibly followed by additional alternating layers. In the proximity of the surface, the wavelength of the density oscillations coarsens with a power law; its amplitude decreasing at distances further away from the surface where the wave is destroyed by isotropic bulk fluctuations [145, 146, 155]. The distance that the wave penetrates the bulk is dependent on the strength of the surface field and the depth of the quench [147, 155–157]. Should the system separate via the nucleation and growth mechanism, a similar layered morphology is observed, however the timescales of coarsening are expected to be slower than a system demixing via spinodal decomposition. In addition, whether the minority phase preferentially wets or dries the surface leads to differences in the competition between the demixing and wetting processes, and therefore different potential gradients drive the phase separation process [158–160].

In the bulk, the demixing process is characterised by one lengthscale, the average domain size L. The break in symmetry of the phase separation due to the presence of the wetting surface means that average domain sizes in the directions parallel and perpendicular to the surface are likely to differ [146, 151, 153]. The work of Brown and Chakrabarti [146], demonstrated that although the physical lengthscales of domains parallel and perpendicular to the surface may differ, they coarsen by the same power law with different prefactors quantifying their difference in size. The average wetting layer thickness, often defined as the width of the first peak of the density profile, should be proportional to the wavelength of this oscillation, and therefore grow with the same growth exponent as the domains in the direction perpendicular to the surface. Brown and Chakrabarti [146] argued that even if domain sizes in different planes are different, if each of the lengthscales (domain size in the bulk, parallel and perpendicular directions and wetting layer thickness) all grow with the same exponent, then there is one dominating lengthscale describing coarsening behaviour close to the surface, and scaling behaviour should be observed. This was illustrated by showing that the density oscillations dynamically scale with the wetting layer thickness $l(t)$, a hypothesis experimentally verified by Krausch *et al.* [151] (see also further discussion in [147, 161]).

A variety of wetting layer growth laws have been observed in experiment and simulation for systems undergoing SDSD. A number of studies on systems in the diffusive regime [146,

151,156] have exhibited a $l(t) \sim t^{1/3}$ growth, notably the same growth exponent for domains of bulk systems in the diffusive spinodal regime. However the growth exponent is found to be dependent on the size and range of surface potential [162, 163] and slower growth laws have been observed [164, 165].

Should the tube structure of the spinodal network be connected to the wetting layer, faster growth laws have been observed. This is attributed to a hydrodynamic pumping mechanism which transports material to the wetting layer via connecting tubes to bulk domains [166,167]. A growth law of $l(t) \sim t^1$ has been observed in [168] and [155] - the same growth exponent for bulk domains coarsening in the hydrodynamic regime. A further faster growth law of $l(t) \sim t^{3/2}$ has been observed in the experiments of Wiltzuis and Cummings [169]. The mechanism behind this growth law is not understood, but is thought to be purely hydrodynamic in origin; suggestions for the underlying reasons have been considered in [153, 167]. A crossover between growth exponents of 1/3 to 1 has been observed in simulations [155, 170] and is explained with a phenomenological argument analogous to the crossover between the diffusive and hydrodynamic regimes in bulk phase separation.

For off-critical mixtures separating via the nucleation and growth mechanism, wetting layer growth is found to be dependent on whether the minority or majority phase is preferred by the surface, quench depth, surface field, and degree of off-criticality [149,159,160]. Should the minority phase wet the surface, both a logarithmic growth law, $l(t) \sim \ln(t)$, and the L-S growth law, $l(t) \sim t^{1/3}$, have been predicted, and the growth exponent may cross from a slower to a faster law at a time determined by the relative field strengths within the sample [158, 159]. For the case of the logarithmic growth law, dynamic scaling is expected to break down as the wetting layer coarsens with a different exponent to the bulk droplets, which coarsen via the L-S growth law [159]. Should the droplets formed be of the non-wetting phase, the competition between the surface and the bulk for the wetting phase leads to a slow growth of the wetting layer, $l(t) \sim t^{1/6}$ [158] or $l(t) \sim \ln(t)$ [159]. Dependant on the quench depth, surface induced nucleation phenomena [171] may also affect the wetting layer growth, however we shall not consider this situation here.

In this chapter we shall study the effects of a single wall upon the phase separation of a colloid-polymer mixture. We shall present evidence of the effect of the anisotropic surface

wave on our samples, determine the wetting layer growth in our system and compare our results to the findings above.

6.3 Experimental system and image analysis

6.3.1 Sample preparation

Sample	ϕ_c	ϕ_p	Glycerol:water ratio of solvent	Estimated $\Delta\rho_{(coll.-sol.)}$ (g/cm^3)	Approximate phase composition, ϕ_L : ϕ_G	$n_{solvent}$ [135]
1	0.086	1.778	76:24	-0.01	1:3	1.44
2	0.038	3.063	51:49	0.06	1:10	1.40
3	0.078	2.326	75:25	-0.01	1:8	1.44

Table 6.1: Sample details

The stock solution of PMMA colloids in approximately 23% water and 77% glycerol prepared in the previous chapter was used with xanthan polymer to prepare samples as detailed in table 6.1. The addition of glycerol to the PMMA-xanthan-water system slows down the phase separation in the system by increasing the viscosity of the solvent. The change in solvent properties alters the phase diagram of the system, and it seems that when the solvent has a higher content of glycerol, only statepoints with a lower liquid to gas phase ratio are accessible. In this chapter, the sample compositions have been chosen to slow the phase separation sufficiently whilst still obtaining the desired ratio of liquid and gas phases. The colloid-polymer mixtures were prepared and allowed to equilibrate in their new solvents before study.

The samples were homogenised using a vortex. Bulk long-time phase separations were recorded in real space using the confocal microscope with a 10x magnification lens in the direction parallel to gravity and the cell wall. The samples were allowed to demix in glass cuvettes of minimal dimensions to avoid distortion due to solvent shear, but of sufficient

width that the cell walls should have a minimal effect on the bulk phase separation characteristics. The information from these images allows us to determine the morphology and timescales of the phase separation regimes, in particular the time before the domains begin to be affected by buoyancy forces.

The effects of a surface upon the decomposition of the sample were studied by pipetting a drop of sample onto a glass slide positioned perpendicular to gravity, and recording the phase separation with a 63x magnification lens. Demixing was imaged in both the xy plane (parallel to the glass surface) and in the xz plane (perpendicular to the surface). These experiments were run for a relatively short length of time to avoid any inconsistencies effects of the solvent drying, gravitational forces or finite droplet size.

6.3.2 Image analysis

The coarsening rate of the system in the xy direction was determined by performing 2-dimensional discrete Fourier transforms on the CSLM images, as described in [7, 125] and chapter 5. The Fourier transforms were radially averaged to obtain the structure factor $I(k,t)$, where I is the intensity of the image and k is the wavevector. The wavevector at the maximum intensity $I_{max} \equiv I(k_{max}, t)$ was obtained using a Gaussian fit. The correlation length in the system corresponds to $L = L_{image}/k_{max}$ where L_{image} is the image width and the coarsening rate in the system was obtained by plotting L against time.

Intensity profiles were constructed by taking the average intensity of each row in the image. Although this is indicative of the density distribution in the sample, the fluorescence detector in the microscope is known not to be linearly responsive to colloid density. In addition the intensity profile will become distorted in the z direction due to scattering by the colloids. This averaging is demonstrated in figure 6.1 (a) in both the xz (full line) and xy directions (dotted line).

The position of the wall was located by first binarising the image, then taking the average intensity profile in the xz direction. The position of the wall was then determined by finding the location of the steepest gradient in the first peak of the profile. In figure 6.1 (b) we see the binarised image, the xz intensity profile of this image (green) and the calculated position of the wall (red).

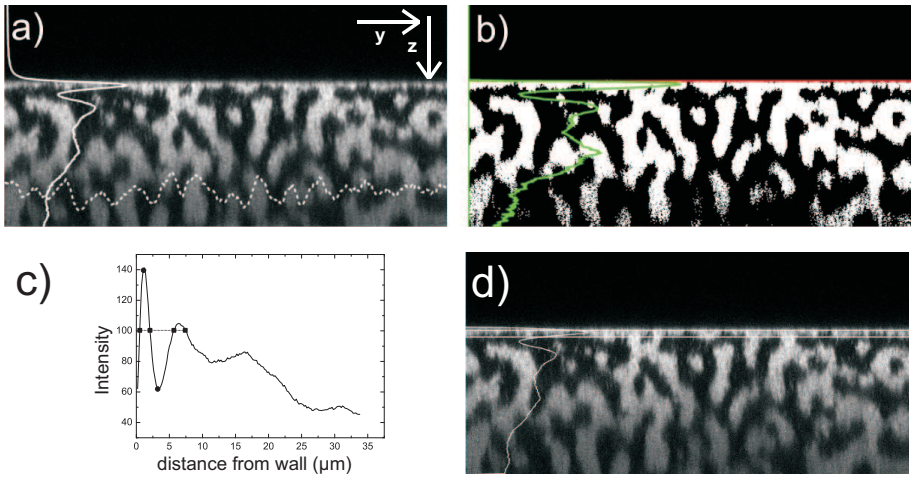


Figure 6.1: (a) Intensity profiles in the xy (dashed) and xz (full) directions. (b) Binarised image, the green line denotes the intensity profile in the xz direction of the binarised image, and the red line the located position of the wall. (c) Intensity profile showing position of relevant turning points (circles) and crossing points at half peak height (squares). (d) The intensity profile in the xz direction and the width of the average wetting layer.

The wetting layer thickness was calculated by locating the x positions of the peaks in the xz intensity profile by numerical differentiation. The intensities associated with these x coordinates were extrapolated using the positions of the two neighbouring points. The located positions of these peaks can be seen in figure 6.1 (c) and are marked as circles on the intensity profile. The intensity value halfway between the first peak and trough was calculated, and is denoted on the graph by a dashed line; the positions where the dashed line crosses the intensity profile is marked by squares. The distance between the first two crossing points has been taken to be the average width of the wetting layer and the distance between the second and third points the average width of the depletion layer. The positions of the first two crossing points and thus the average wetting layer width has been marked on the image in figure 6.1 (d). It was not always possible to calculate the width of the depletion layer if the intensity of the second peak in the xz profile was too low due to scattering by the colloidal particles, and this effect leads to an overestimation of the depletion layer width. Additional distortion of the intensity profile is caused by the refractive index mismatch between the sample (see table 6.1), and the immersion medium of the lens ($n_{oil} = 1.51$, Zeiss

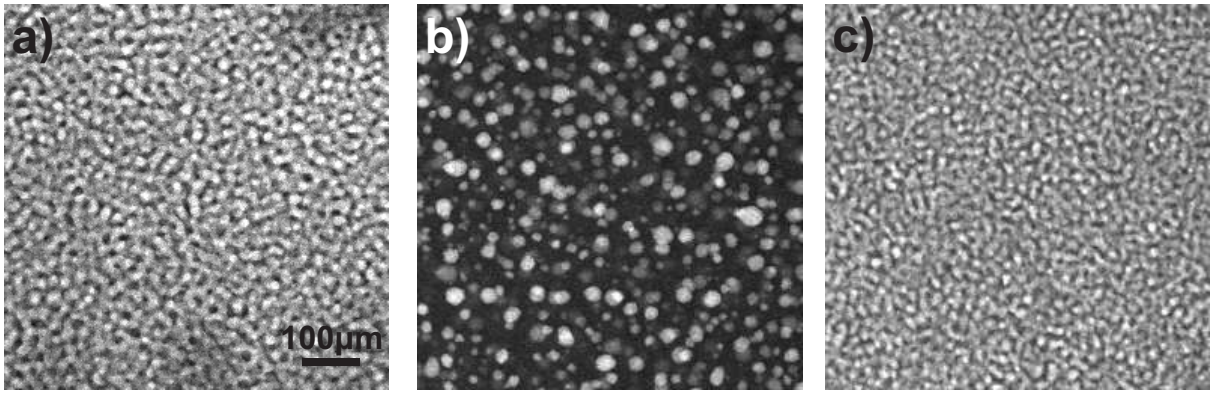


Figure 6.2: Bulk phase separations in the xy plane of (a) sample 1, (b) sample 2, (c) sample 3.

'Immersol') leading to an elongation of the image. The image is stretched by a factor of n_{oil}/n_{sample} leading to a lengthening of 6-8% of the direction in the z axis [172], where we approximate the refractive index of the solvent as a representation of the refractive index of the sample. We correct for this distortion of the z-axis when constructing our intensity profiles in the direction perpendicular to the surface.

6.4 Results

6.4.1 Bulk phase separation

Before we consider the effect of a surface upon the demixing of our sample, we first establish the dynamics of demixing in the bulk. The morphology of samples 1-3 are shown in figure 6.2. We can see that samples 1 and 3 exhibit the classic network structure associated with spinodal decomposition, however on equilibration, sample 3 is seen to contain less of the liquid phase (see table 6.1). The statepoint of sample 2 is within the metastable region of the phase diagram and demixing proceeds via the nucleation and growth of droplets, which coarsen by coalescence on one another. The images were analysed by 2 dimensional FFT analysis as described above, and we plot the characteristic lengthscale of the structures against time in figure 6.3. We can see that domains in each of the spinodal samples grow in the linear regime although some curvature at early measurement times suggests that the crossover between the diffusive and hydrodynamic regimes may not be completed within the

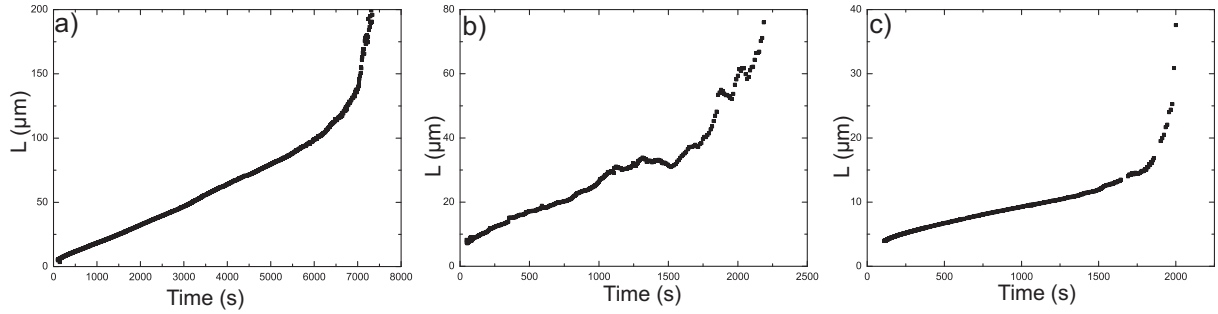


Figure 6.3: Growth of characteristic length scale with time in samples 1 (a), 2 (b) and 3 (c).

timescale of our SDSD experiments. The lengthscale diverges as the domains are ripped apart by buoyancy forces after around 6000s in the case of sample 1 and around 1500s in samples 2 and 3. In samples 1 and 3 the density difference between the phases is such that the liquid phase rises, where as in sample 2 it sinks to the bottom of the container. We shall now consider how the presence of a surface affects the phase separation for each of these cases.

6.4.2 Surface directed spinodal decomposition

In figure 6.4 we see the development of spinodal decomposition in the vicinity of a single wall. The left hand image sequence is taken in the xy plane (parallel to the surface), and the right hand image sequence in the xz plane (perpendicular to the surface). In the xy images (recorded at a depth of approximately 40 μm) we see the domains coarsen in a symmetrical

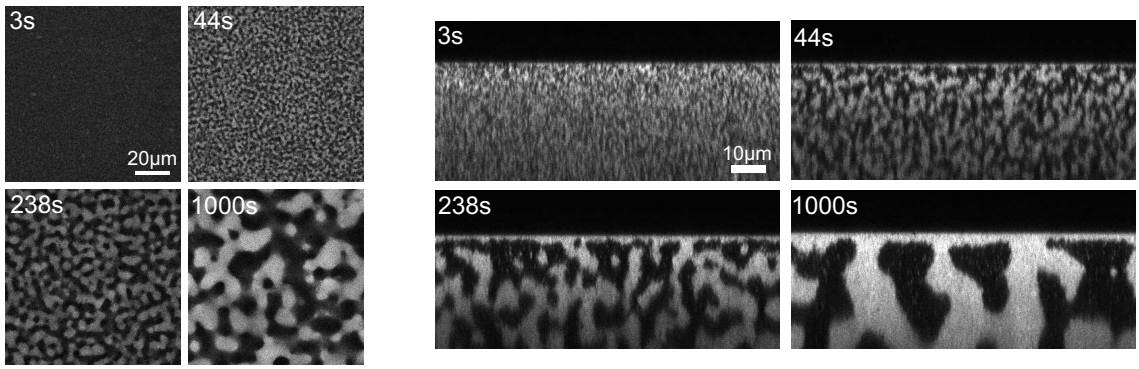


Figure 6.4: CSLM images at 63x magnification of sample 1 in the xy plane (left hand sequence) and xz plane (right hand sequence.)

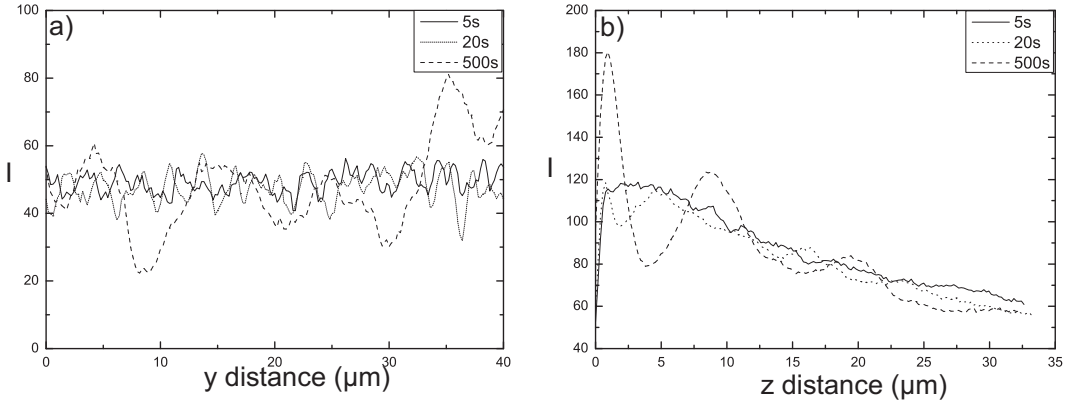


Figure 6.5: Average intensity per row vs distance in the (a) y and (b) z directions for sample 1.

network. It is clear from the xz images that the liquid (bright) phase preferentially wets the wall, breaking the symmetry of the phase separation perpendicular to the surface. Immediately after homogenisation, the sample is reasonably uniform and little coarsening has occurred (3s). As the sample begins to phase separate, we see the formation of a wetting layer on the wall as domains coarsen throughout the sample. As the domains grow larger, the wetting layer thickens (238s). We see that bulk domains remain connected to the wetting layer, allowing material to be transported to the surface via the spinodal network. As the spinodal structures coarsen, the connecting tubes thicken in both the directions parallel and perpendicular to the surface. By the final image (1000s) the domains are large in size, the wetting layer is thick and there are large tube structures connecting the bulk liquid phase to the wetting layer.

We can quantify these observations with average intensity plots in the xy and xz planes. In the z direction the 0 value represents the solid surface as located by image analysis. As the average intensity values are not necessarily an accurate representation of the colloidal density in the sample, and the plots in figures 6.5, 6.6, 6.8 and 6.10 should not be considered as density profiles, however they do provide useful information to quantify the developing morphologies. In figure 6.5 we see that in the xy direction the fluctuations remain similar in phase and amplitude across the area examined. In the xz direction, we observe the growth of an oscillating wave originating from the surface. Although the signal becomes more noisy with increasing z, we see the wave break down as we move towards bulk domains. A more

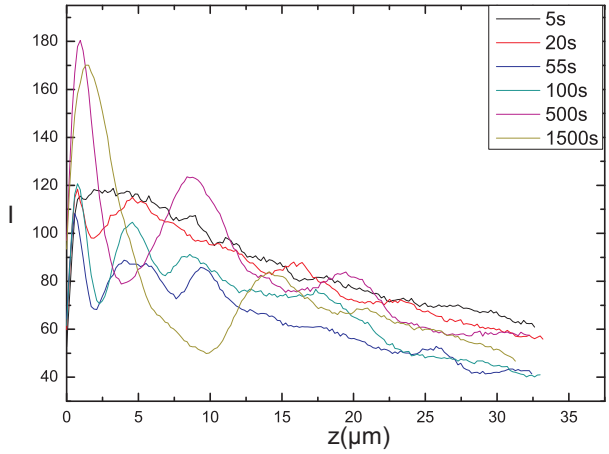


Figure 6.6: A more detailed plot of average intensity vs distance from the surface for sample 1.

detailed representation of the development of the wave can be seen in figure 6.6. We observe a peak close to the surface representing the wetting layer, followed by a trough corresponding to the depletion layer. At early times, these are small, and become more distinct as the SDSD progresses and the wetting and depletion layers grow.

In figure 6.7 we observe the phase separation of a system similarly affected by a solid surface, but demixing via the nucleation and growth mechanism. Initially the system is homogeneous, but due the preferential wetting of the surface by the liquid phase, we quickly see the formation of both a wetting layer and a depletion layer (9s). The wetting layer is visible much earlier than for sample 1, however the low colloid concentration in this sample gives a much better contrast between the wetting layer and the bulk. The material

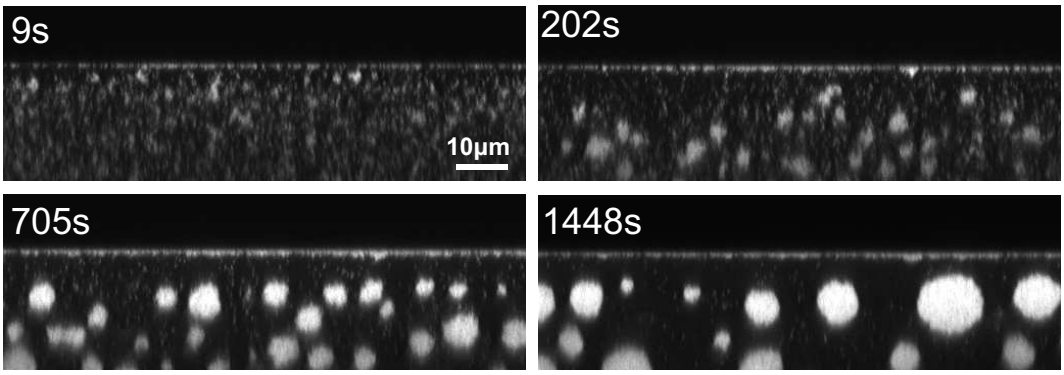


Figure 6.7: CSLM images showing the progression of the demixing of sample 2.

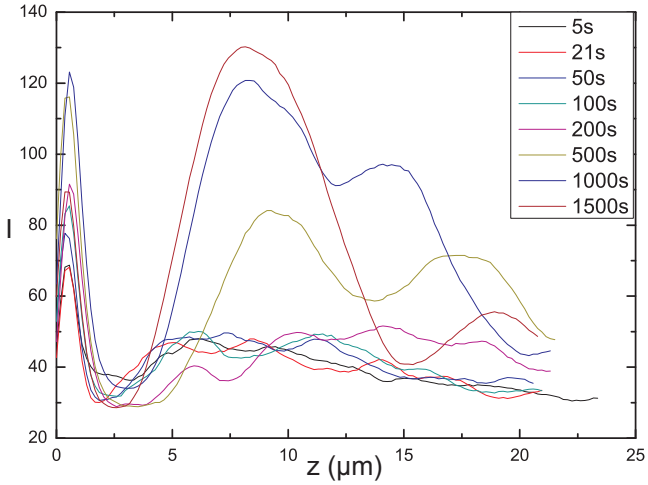


Figure 6.8: Average intensity per row vs distance from the surface for sample 2.

outwith the vicinity of the surface forms droplets, which coarsen generally by coalescence as observed in bulk demixing. There is no connection between the liquid phase in the bulk and the wetting layer on the wall, so the growth of the wetting layer is limited by the droplets diffusing across the depletion layer and coalescing on its surface. These droplets then spread out across the whole wetting layer.

We quantify these observations in a detailed plot of the evolution of the average intensity profile in figure 6.8. From the outset there is a clear peak and trough in the intensity profile associated with the wetting and depletion layers, which grow in width as demixing progresses. After a time we notice that the wetting layer stops thickening, and only the depletion layer widens.

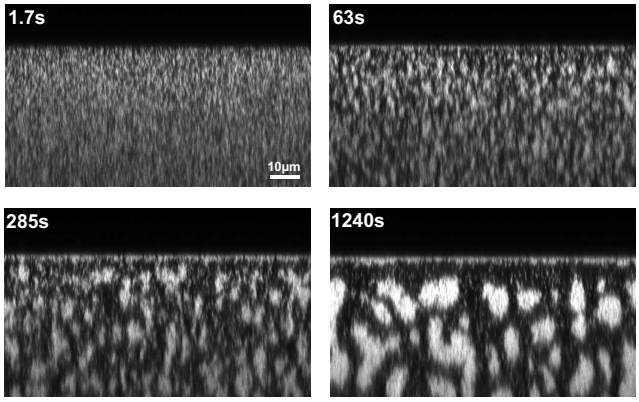


Figure 6.9: CSLM images of the phase separation of sample 3 in the xz plane.

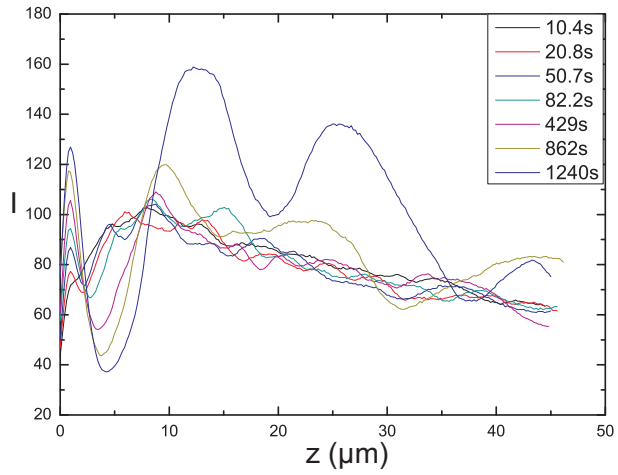


Figure 6.10: Average intensity per row vs distance from the surface for sample 3.

Finally we consider a third sample which also demixes via spinodal decomposition, however in this case there is significantly less liquid phase within the system. Similarly to sample 1, initially we see a homogenised mixture and little domain growth (figure 6.9 1.7s). The wetting layer is established quickly, the bulk system coarsens via spinodal decomposition, and the wetting layer is connected to bulk domains (63s). However due to the lower ratio of the liquid phase in this sample, as the domains grow, and the wetting and depletion layers widen, the domains connecting the bulk to the wetting layer snap (285s, 1240s). This behaviour significantly differs from the bulk phase separation which holds a bicontinuous network structure until it crosses into the gravity driven regime (figure 6.2). Once the connection between bulk domains and the wetting layer is broken, the wetting layer can only grow by the diffusion of liquid phase across the depletion layer. Again in figure 6.10, we show plots of average intensity in the z direction for various time intervals to demonstrate the evolution of the wetting and depletion layers. Both layers grow in size as the SDSD process progresses.

Wetting layer growth

We now analyse the wetting layer width as described in section 6.3.2, and show plots of the wetting layer growth in figure 6.11. As we would expect, the wetting layer grows fastest in sample 1, where liquid material may be transported to the wetting layer by the connection

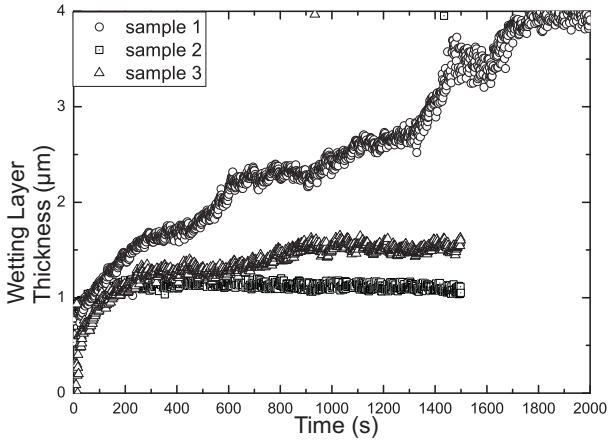


Figure 6.11: Plot of wetting layer thickness vs time for samples 1-3.

to bulk domains. The measurement of its thickness becomes unreliable at later times, as the breadth the connections to the wetting layer become significant compared to the image width. For all samples the wetting layer thickness is difficult to obtain at early times when it is comparable to the size of one pixel (0.2 μm).

The wetting layer in sample 2 thickens much more slowly, as growth is limited by the diffusion of droplets across the depletion region, and reaches what we assume to be its equilibrium thickness after around 300s. The slow growth of the wetting layer in this sample is magnified by the fact that the solvent in sample 2 is of a significantly lower viscosity than sample 1 (and sample 3), therefore we would expect diffusion to proceed more quickly. The viscosity of sample 2 was lowered to ensure that the phase separation and wetting layer growth, which evolves via a slower mechanism, had progressed sufficiently before the sample began to dry. In addition, in a higher viscosity solvent, the equilibrium wetting layer thickness was considerably thinner for a system demixing via the nucleation and growth mechanism, making its development more difficult to study.

In sample 3, although the initial layer of liquid wetting the surface is thinner, the wetting layer appears to grow at a similar rate to that of sample 1 for around 200s. After this time, the growth of the wetting layer slows considerably. Although our CSLM images in figure 6.9 only represent a small number of the domains within the vicinity of the surface, after around 200s we see the tubes connecting the bulk network to the wetting layer are beginning to snap off. This means that the wetting layer is unable to thicken via the faster hydrodynamic

mechanism, and tends towards the slower diffusion limited mechanism exhibited by sample 2.

6.5 Discussion

The morphology exhibited by our phase separating colloid-polymer mixtures in the presence of a solid surface is in reasonably good agreement with previous predictions by simulation [150, 155, 164] and experiment [145, 149, 151] for quenches from both the unstable and metastable regions of the phase diagram. We observe the development of wetting and depletion layers as domains coarsen, breaking the symmetry of the phase separation process. For sample 3, we see that the surface field modifies the bicontinuous structure. Tubes connecting bulk domains to the wetting layer snap off as the lack of liquid phase in the depletion region violates the bicontinutiy condition, but the spinodal network remains interconnected in the bulk.

In our experiments, we observe only one clear oscillation of our intensity profiles in the direction perpendicular to the surface, corresponding to the wetting and depletion layers. A higher degree of layering has been observed in previous experiments (e.g. [145, 173]) using scattering techniques, where a true representation of the density oscillations may be constructed. Although our intensity profiles become extremely distorted due to colloidal scattering at reasonably short distances, we can see by eye that domains not in direct contact with the wetting layer line up behind the depletion layer, suggesting the density profile would show further oscillations. In some simulatory work, the layered structure induced by the surface field has resembled stripes, a phenomenon not observed here (see for example [155, 164]). This could be due to the differing importance of quench depth, critical composition, or strength of the surface field within our system [157,162]. This highly ordered layering appears in the early stages of demixing whilst the system is in the diffusive spinodal regime, which occurs too quickly to observe in these samples. The phase diagram of this colloid-polymer system is such that we cannot access this regime by increasing the quantity of glycerol in the solvent, and still locate a statepoint containing a high enough fraction of the liquid phase that the bulk spinodal network remains connected to the wetting layer. In

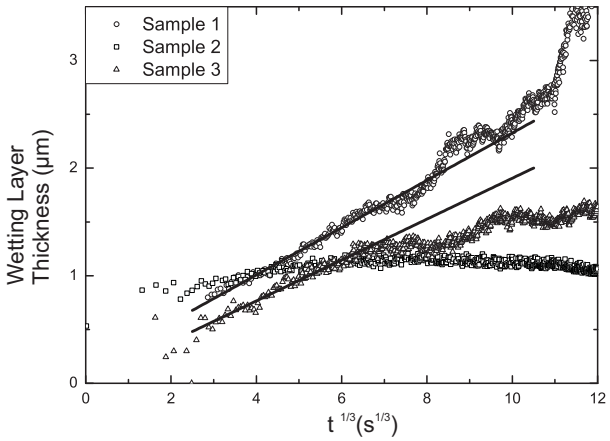


Figure 6.12: Wetting layer growth for each sample vs $t^{1/3}$. The thick black lines represent linear fits to the data.

any case, during diffusive coarsening, we would not expect the composition of the two phases to have reached equilibrium concentrations, or sharp interfaces to have been formed, thus it is unlikely that such a clearly visible pattern would be reproduced in our microscopy images.

A variety of power laws have been proposed for the growth of wetting layers at a surface in contact with a demixing system. It is not reasonable to obtain power laws from double log plots due to the short timescales over which we obtain our data, however in figure 6.12, we plot the wetting layer growth of each sample against $t^{1/3}$. For sample 1, we obtain a relatively straight line as indicated, demonstrating that the wetting layer growth proceeds with an approximate power law of $l(t) \propto t^{1/3}$. The growth in sample 2 clearly does not follow this power law. In sample 3, initially the wetting layer growth appears to obey the power law $l(t) \propto t^{1/3}$, however around 200s the growth rate reduces, a time corresponding to the snap off of connecting domains.

The exponents characterising the growth of the wetting layer in samples 1 and 3 which separate by spinodal decomposition, are smaller than expected. Images of sample 1 and sample 3 at early times (see figure 6.4 and 6.9) show tubes with sharp interfaces connecting the bulk domains to the wetting layer, suggesting that wetting layer growth should be in a hydrodynamic regime. This would lead to a power law of $l(t) \sim t^1$ [155, 170] or possibly faster [169, 174]. The growth exhibited by our samples is closer to $l(t) \sim t^{1/3}$, as observed in systems where the wetting layer grows via a diffusive mechanism. An examination of bulk

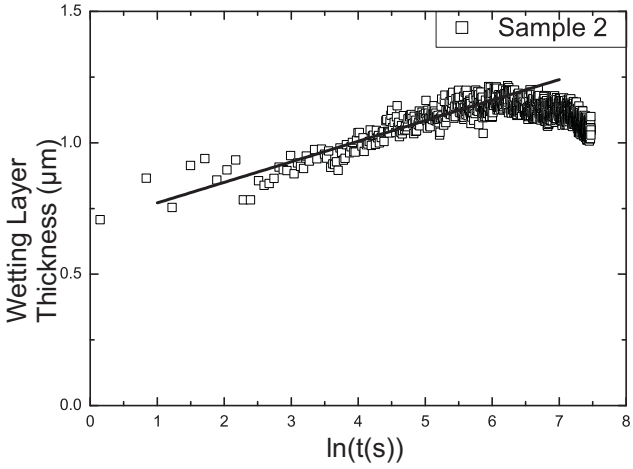


Figure 6.13: Plot of wetting layer growth vs $\ln(t)$ for sample 2. The thick black line represents a linear fit to the data.

domain growth at early times suggests that the growth exponent within the timescale of the SDSD experiments is around 0.8, indicating that the bulk system is likely to be crossing over between diffusive and hydrodynamic coarsening. This is supported by the observation in the previous chapter that our systems with a higher viscosity solvent exhibit a slow crossover between these regimes. The crossover between the diffusive and hydrodynamic regimes of systems demixing via spinodal decomposition in the vicinity of a wall has been explored in simulations [155, 170], however we have no indication of how the time and lengthscales related to this crossover in the bulk will correspond to these domains under the influence of a surface field, or the growth of the wetting layer. Here, although the wetting layer seems to be growing via a mechanism which is still partially diffusive, it would appear that hydrodynamic transport does also play a role, which we would expect to become dominant as the system moves into a fully hydrodynamic regime. At later times, although the width of the wetting layer becomes more difficult to measure, growth appears to accelerate, consistent with this expectation. The wetting layer of sample 3 thickens significantly faster at early times whilst it is still connected to bulk domains. This clearly illustrates the ability of the spinodal network to transport matter to the surface, and highlights the importance of hydrodynamic effects when considering the growth of a wetting layer.

The wetting layer in sample 2 grows much more slowly as it is limited by the diffusion of

liquid droplets across the depletion layer. After around 400s it stops growing as it reaches its equilibrium thickness, determined by the interplay between gravitational forces and the depletion interaction [175, 176]. Due to the relative densities of the liquid and gas phases, once bulk demixing moves into the gravity driven regime, we expect liquid droplets to fall onto the wetting layer and a macroscopic interface will form [7, 78]. Our experiment is stopped before this regime is observed in the bulk and we expect that the droplets studied in this experiment are too small to have been affected by sedimentation. From the numerical simulations of Puri and Binder [160], and Yan and Xie [159] the predicted growth laws are dependent on both the order parameter and the strength of surface potential, values difficult to evaluate in practical experiment. It is difficult to reliably determine a power law for our data due to the short timescale over which the wetting layer grows, however from figure 6.13, it appears that a logarithmic growth law may apply before the equilibrium thickness is attained.

For sample 3 we observe initially, whilst the bulk domains remain connected to the wetting layer, that it grows with a power law of approximately $l(t) \sim t^{1/3}$ (figure 6.12). Once the domains snap off after around 200s, the growth of the wetting layer becomes limited by the diffusion of the liquid phase across the depletion layer, the growth mechanism observed for sample 2. In this case, we would expect the growth of sample 3 to cross over to the same power law as observed in sample 2. In figure 6.14 (a) we plot the wetting layer growth for sample 3 against $\ln(t)$. Again it is difficult to reliably obtain power laws due to the short timescales involved, however it appears that a logarithmic growth law applies to the majority of the data, although at early times (prior to 200s) it seems that growth is faster. We summarise this crossover between regimes in figure 6.14 (b). At early times the wetting layer thickens via a faster growth mechanism whilst liquid matter may be transported to the surface through the spinodal network. When this connection is severed, the wetting layer growth becomes limited by the diffusion of liquid droplets across the depletion region and the growth rate slows. It is unclear in the long term how the diffusion of the at least partially interconnected bulk domains in the vicinity of the surface will differ from the spherical droplets observed when the bulk system is demixing via nucleation and growth.

We are unable to test the scaling arguments of Brown and Chakrabarti [146] as we cannot

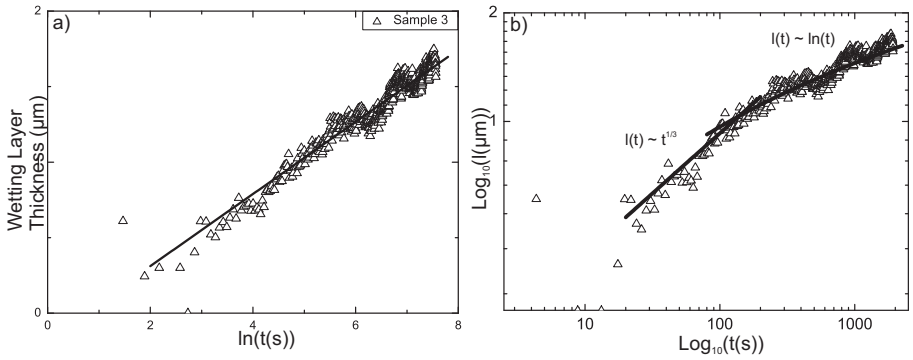


Figure 6.14: (a) Plot of wetting layer thickness vs $\ln(t)$ for sample 3. (b) Double logarithmic plot of wetting layer thickness vs time for sample 3.

construct composition waves for reasons already discussed. It is unclear for which of our systems we expect dynamic scaling of the composition wave with the wetting layer thickness to apply, as this is dependent on the wetting layer growing with the same power law as the coarsening of bulk domains. In sample 1 and sample 3 at early times, the system is crossing over from diffusive spinodal to hydrodynamic coarsening, and it is uncertain whether this transition will occur at the same time in the bulk and at the surface. This may well vary considerably depending on the type of system considered, in colloid-polymer systems the large size of the colloids and polymers may well have a significant effect on the interplay between phase separation and wetting behaviour. For sample 2 and sample 3 at later times, dynamic scaling is not expected to apply, as the wetting layer thickens with a different growth exponent to the domain size in the bulk.

6.6 Conclusion

In this chapter we have investigated the effect of a solid surface upon the fluid-fluid demixing of a colloid-polymer mixture, to our knowledge the first time this has been explored. Using the technique of CSLM we show real space images of the phase separation in the directions parallel and perpendicular to the surface, showing the surface field breaking the symmetry of the phase separating morphology, and influencing the coarsening behaviour of domains. We have studied the growth of the wetting layer for systems of differing composition, obtaining

results consistent with previous experiment and simulation. The prediction of a growth law for a particular experimental system remains challenging due to the involvement of a high number of competing influences. The role of hydrodynamics in wetting layer evolution has been widely discussed (see [170] in particular), and we illustrate that the hydrodynamic transport of the wetting phase from bulk domains to the surface leads to an accelerated growth of the wetting layer. Should this connection be severed its thickening shall become limited by the diffusion of droplets across the depletion region, and the growth rate slows. The transition of the bulk system between demixing regimes determines the coarsening rate of bulk domains, but will also affect domains under the influence of a surface field, and the growth of the wetting layer. The effect of these crossovers on the interplay between wetting and phase separation remains a subject of investigation.

Chapter 7

Demixing of colloid-polymer systems confined between two parallel plates

ABSTRACT

We observe the demixing of colloid-polymer mixtures confined between two parallel plates in real space using Confocal Scanning Laser Microscopy. We study samples of differing phase composition separating via both the nucleation and growth and spinodal decomposition mechanisms. The material in the central region between the plates coarsens in a similar manner to the bulk, until domains grow to a size such that the presence of the surfaces limits their growth. As domains get larger, the dimensionality of demixing transfers from three to two dimensions, and further coarsening of the system strongly depends on the interaction of the domains in the centre of the plates with the wetting layers. Dependent on the phase composition of the system, hydrodynamic processes may play an important role in both the growth of the wetting layers, and the coarsening regimes observed. We discuss our findings in the light of a large number of previous experimental and theoretical studies.

7.1 Introduction

The phase behaviour of fluids confined between two or more surfaces is of fundamental scientific interest due to the complexities of the phenomena involved. In addition to the interaction between the effects of phase separation and the preferential wetting of a surface

by one component in the system, [145–147], finite size effects (e.g. capillary condensation) due to the finite width of the confinement geometry [19, 177, 178] may also play a role. The combination of surface geometry and interfacial tension in the system may create new stable or metastable structures such as capillary bridges [109, 179], and the presence of the confining walls may cause phase transitions not seen in the bulk [20, 171, 180], or change the dimensionality of the phase separation [181]. An understanding of these phenomena has a considerable number of practical applications, for instance in the geophysical industries, where the porous construction found in rocks and soils confines fluids on very small lengthscales [182]. The rapidly evolving field of microfluidics involves the flow of picolitres of fluid in extremely small channels [183], and such systems are being developed for use in, for example, sensing technology [184] and separation and analysis procedures in molecular biology [67,185]. The subdiscipline of multiphase microfluidics has attracted recent attention due to its varied applications including drug delivery and microreaction systems [186–188].

The study of molecular fluids restricted to nanoscopic dimensions can prove extremely difficult due to the small lengthscales involved. As well as the requirement for a well characterised system, wall roughness of even an atomic scale can cause additional unwanted effects [22,189]. The larger lengthscales of soft matter systems such as colloid polymer mixtures or polymer blends offer an opportunity to test the many hypotheses from theoretical or simulation work [2]. Here we shall use our colloid-polymer mixture to conduct a real-space study of demixing in a simple two plate geometry.

We begin by reviewing the extensive literature associated with this topic, from experiment, theory and simulation. We shall then detail our experimental method, and categorise our samples according to their demixing morphologies in the bulk. We then present and discuss the results of our confinement experiments in two sections, firstly considering extremely off-critical phase separation from the metastable region of the phase diagram, and secondly studying more symmetrically composed samples demixing via spinodal decomposition. In both cases we shall quantify our findings by analysis of the phase separation in the directions both perpendicular and parallel to the plates, and compare our results to the previous findings outlined above. We finish with a general discussion and some concluding remarks on all types of morphologies.

7.2 Background

The previous chapter considered the influence of a single wall upon the demixing of a colloid polymer system. We established that the preferential wetting of the surface by one phase in the system results in differing coarsening behaviour in the directions parallel and perpendicular to the wall. This creates an anisotropic density oscillation which propagates perpendicular to the surface into the bulk, breaking the symmetry of the phase separation. A layer of the wetting phase forms on the surface, which is followed by a layer (know as the depletion layer) of the non-wetting phase. Further layering may occur; the degree to which the wave penetrates the bulk is dependent on the depth of the quench and the strength of the affinity of the wall for its preferred phase (see chapter 6 and for example [145] and [147]).

We shall now extend our arguments to the phase separation of a fluid-fluid system between two parallel plates, confined by two walls in one dimension, but unrestricted in the other two. As the system phase separates, density oscillations shall propagate perpendicular to each surface towards each other in the confined dimension. If the slit width is sufficiently small, these waves will overlap and interfere, creating patterns of constructive and destructive interference [190], further altering the phase separation morphology from the semi-infinite single-wall case. This interference model breaks down if the system is confined to a plate spacing smaller than the time-independent characteristic wavelength associated with the very early stages of spinodal decomposition [130, 190], and the system decomposes with a wavelength determined by the dimensions of the confinement [190, 191].

Here we shall only consider the limiting case where both of the confining surfaces are completely wet by the same phase. As the system demixes it moves towards an equilibrium bilayer structure where a layer of the non-wetting phase is sandwiched between the two wetting layers [192, 193]. The symmetry of the wetting layer thickness may be disrupted by gravity, the effects of which are expected to become significant when the distance between the slits exceeds the capillary length (L_c) in the system [194].

The extensive experimental work of Tanaka (see [193] and references therein) has shown the behaviour of a system demixing in confinement is dependent on its domain geometry. Samples from the stable and metastable areas of the phase diagram separate via different

mechanisms, as already discussed in the preceding chapters. Extremely off-critical samples from the metastable region will demix via the nucleation and growth morphology. Droplets of the minority phase with lengthscale $L(t)$ will nucleate after an induction time, and will then coarsen with an expected growth law of $L(t) \sim t^{1/3}$, either by the evaporation-condensation (Ostwald ripening) mechanism [74], or by diffusion and coalescence [73]. Critical samples will separate via spinodal decomposition; immediately density fluctuations governed by the free energy landscape grow in amplitude at a time independent wavelength in what is known as the Linear Cahn Hilliard regime [130]. The system then moves into a diffusive regime where domains coarsen with an expected power law of $L(t) \sim t^{1/3}$ [78] followed by a viscous hydrodynamic regime where $L(t) \sim t^{1}$ [78]. This may be followed by an intertial regime [131]. For both mechanisms, when the domain size becomes comparable to the capillary length of the system, buoyancy forces will rip apart the structures and the phase separation will become driven by gravity [78]. When considering how a particular sample will behave in confinement, it should be noted that a narrow slit has been shown to alter the statepoint of the demixing system due to capillary condensation [20] and can result in a shift of the phase separation from critical to off critical [189,195], or result in phase transitions that would not be seen in bulk [196].

Following the route of Tanaka, we shall consider the demixing of a system into phases A and B, where phase A completely wets the walls. We consider 3 cases: off-critical demixing where the wetting phase is in the minority ($\phi_A << 1/2$), off-critical demixing where the wetting phase is in the majority ($\phi_A >> 1/2$)), and the critical demixing of a sample with a reasonably symmetric composition ($\phi_A \sim 1/2$). We shall now discuss the morphological behavior of the phase separation of such a system when confined between two plates spaced a distance d apart.

Droplets - Minority of the wetting phase, $\phi_A << 1/2$

When the more wettable phase is in the minority, a layer of the wetting phase will form on each surface immediately, as the dynamics of surface enrichment are faster than those in demixing [178], and droplets (radius a) of the wetting phase will form in the central region between the plates. As the system coarsens, the droplets will grow in size either via Ostwald

ripening or coalescence [73, 74], and the wetting layer (width $l(t)$) will thicken as droplets coalesce on its surface [166]. As the droplets grow in size, they line up along the central plane between the plates, and as their size becomes comparable to the plate spacing, they deform from spherical to disk shaped. The droplets gradually diffuse towards the walls and coalesce on the surfaces. After a time all the droplets disappear and the system approaches an equilibrium where a layer of less wettable phase is sandwiched between two layers wetting the walls [193]. The unconfined growth of droplets is governed by the Lifshitz-Slyozov growth law, thus the droplets are initially expected to coarsen as $a \sim t^{1/3}$ [74]. The wetting layer growth is limited by the diffusion of droplets across the depletion layer - for the semi infinite geometry discussed in the previous chapter wetting layer growth of $l(t) \sim t^{1/3}$ or $l(t) \sim \ln(t)$ is predicted [158, 159]. However the parallel plate geometry leads to a limitation on the amount of wetting phase available [197], and may further slow growth.

Droplets - Majority of the wetting phase, $\phi_A >> 1/2$)

In the case where the preferentially wetting phase is in the majority, there will be a coating of this phase over the wall from the outset. Droplets of the minority phase will form and coarsen in the centre of the plates via Ostwald ripening or coalescence, leading to a predicted coarsening of the drop radius as $a \sim t^{1/3}$ [73, 74, 198]. When the droplet diameter becomes comparable to the slit spacing, the droplets will change from spherical to disk shaped [193]. We would expect these disks of the non-wetting phase to become greater in width in the confined plane than those of the wetting phase in the situation where $\phi_A << 1$, as there is a lower degree of layering in the system. Once the transition from spherical to disk like droplets occurs, the droplets continue to grow by diffusion and coalescence. The mechanism for further coarsening has not been determined. In previous experiments the droplet size has been found to continue to grow as $a \sim t^{1/3}$ [166, 181] consistent with L-S growth, while the droplet diffusion-coalescence mechanism in 2 dimensions predicts growth based on Stokes law of $a \sim t^{1/2}$ [73, 178]. Additionally it has been suggested that concentration fields may induce a convective flow around droplets moving them hydrodynamically, making a droplet involved in one collision more likely to experience subsequent collision, and increasing the coarsening rate of the system [199, 200]. Due to the large spacing between the droplets it is

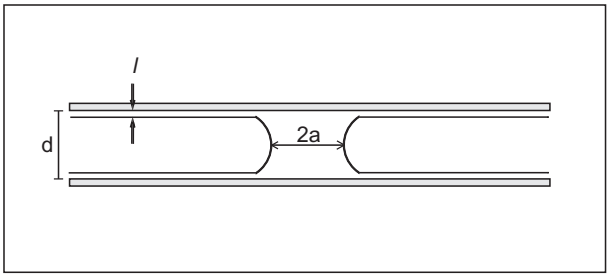


Figure 7.1: Schematic diagram of a bridging droplet of radius a between two plates of spacing d. The wetting layer thickness is denoted by l. [193]

unlikely that there is any interaction between them through the wetting layer [181], as will be discussed in the next section.

Spinodal decomposition of an approximately symmetric mixture, $\phi_A \sim 1/2$

The spinodal decomposition of an approximately symmetric mixture between two plates can be divided into 3 stages characterised by the dimensionality of the phase separation [156, 181, 201]. Spinodal decomposition takes place initially, the system progresses through the early stage regimes into the hydrodynamic regime, and a 3 dimensional interconnected network structure with sharp interfaces is formed [78]. The wetting layer on the surfaces will form quickly via a hydrodynamic process as it is connected to the spinodal domains by interconnecting tubes, allowing the transport of the wetting phase to the surface. The growth of the domain lengthscale $L(t)$ and the wetting layer $l(t)$ are dominated by hydrodynamic processes, thus their lengthscales grow linearly in time [78, 155, 168]. The domains coarsen, the wetting layers grow thicker, and the morphology changes from a network structure to bridging tubes connecting the wetting layers on each plates. Thus we see the system change from a 3 dimensional spinodal network to a system of 2 dimensional bridging droplets of radius a [156, 181, 201]. Figure 7.1 illustrates a cross section in the confined plane of such a bridging droplet. The diameter of the bridge is $2a$, between two plates with wetting layer thickness l, separated by distance d.

The subsequent behaviour of the droplet is dependent on its size. Following the outline by Tanaka, the Laplace pressure within the bridging droplet is given by $\Delta p = \gamma(1/R_1 + 1/R_2)$, where the transverse curvature is $R_1 \sim 1/a$ and the longitudinal curvature $R_2 \sim 2/d$ [109].

When the diameter of the bridge is greater than the plate spacing ($2a > d$), the pressure gradient will cause material from the wetting layer to flow into the tube, and the diameter of the bridge will increase. Should the bridge diameter be smaller than the plate spacing ($2a < d$), the pressure gradient shall be in the opposite direction, transporting matter into the wetting layer. The bridge will shrink, eventually running out of material and the connection between the two layers will break [166, 181]. An argument involving surface energies and the conservation of matter by Bodensohn and Goldberg yields a similar prediction [194]. Both these works indicate a critical radius for the expansion of a bridging tube of $2a \sim d$, a condition independent of system properties and dependent on the plate spacing d.

For bridges wider than this critical radius, the diameter of the circular droplet is predicted to grow linearly in time, as the transportation of matter from the wetting layer to the bridging tube is via a hydrodynamic process [153, 166]. After a time their growth has been observed to slow considerably, as these bridging droplets collide and the morphology converts to an interconnected 2 dimensional network [156, 166, 194, 201]. There is currently no defined model for the growth of these domains, and various mechanisms are likely to contribute simultaneously [201]. Tanaka proposes that as the circular bridges widen, their growth becomes limited by an interaction between domains due to the finite amount of material in the wetting layers. There will be an attraction between the droplets as they feed on the same material from the wetting layers and expand, which also reduces the surface energy of the tube of non wettable phase separating the bridges [166]. Through an analysis based on the Navier-Stokes equations, Tanaka predicts 2 dimensional domains characterised by the lengthscale L grow as $L \propto t^{1/3}$ when the interfaces of neighbouring droplets are separated by a distance greater than d, and a growth law of $L \propto t^1$ for a separation less than d [181]. Wang and Composto [201] highlight the significance of the changing wetting layer thickness, as the longitudinal curvature of a droplet is strictly $R_2 = 2/(d - 2l)$. The wetting layer thins as the droplets expand, meaning the longitudinal curvature grows, and the pressure difference driving the domain growth decreases. Their work suggests the 2 dimensional domains may be characterised by a logarithmic growth law across the whole regime as opposed to a crossing from t^1 to $t^{1/3}$ growth as proposed by Tanaka. In addition to the back flow from the wetting layers via these domain interaction or capillary pressure

mechanisms, growth may also be driven by diffusion, or by phase coarsening as coexistence compositions are reached [201]. The relative importance of these factors in domain growth kinetics are likely to be dependent on the subtleties of the system studied. Whether through coarsening, diffusion or a backflow mechanism, the droplets will collide and the pattern will change to an interconnected network in 2 dimensions [181]. This network coarsens, and the system eventually reaches its equilibrium layered structure [193, 201].

7.3 Experimental details and analysis

7.3.1 Experimental details

To fully explore the effects of confinement between two parallel plates on our colloid-polymer system, we need to create samples corresponding to each of the cases of domain geometry described in the previous section. To allow us to fully observe the demixing process, we increase the viscosity of the solvent of our colloid polymer system (see chapter 5). In addition to slowing down the phase separation, we observed that by partially changing the solvent of the PMMA-xanthan water system described in chapter 2 to glycerol, we alter the position of both the spinodal and binodal. The modification of the phase diagram is such that we are unable to access statepoints containing a high fraction of the liquid phase in a viscous solvent. Moreover, should the viscosity of the sample be particularly high, it becomes difficult to fill the narrow confinement cell quickly. With these concerns in mind, samples were prepared as detailed in table 7.1.

Sample	ϕ_c	ϕ_p	Glycerol:water ratio of solvent	$\phi_L : \phi_G$	Bulk Morphology	$n_{solvent}$ [135]
1	0.051	4.988	37:62	15:85	Liquid droplets	1.38
2	0.081	3.484	41:59	25:75	Spinodal	1.39
3	0.135	2.330	32:68	70:30	Spinodal	1.37
4	0.201	1.018	7:93	10:90	Gas bubbles	1.34

Table 7.1: Sample details

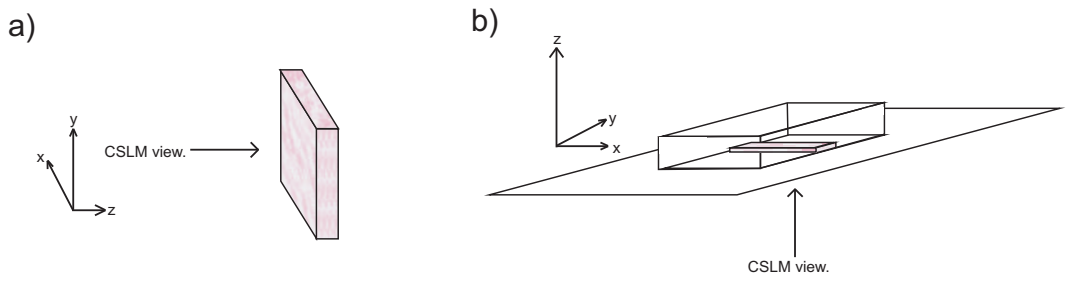


Figure 7.2: Schematic diagrams of the experimental setups for a) bulk phase separations, and b) confined phase separations. Dimensions are not to scale.

In a similar manner to previous chapters, samples were homogenised using a vortex, and phase separations were recorded in real space using Confocal Scanning Laser Microscopy. Bulk phase separations were imaged using a 10x magnification lens in the direction parallel to both gravity and the cell wall, in glass containers of suitable dimensions to minimise solvent flow, but not confine the system (figure 7.2 (a)). Particularly in systems of higher glycerol content, the homogenisation process can cause the formation of air bubbles in the solvent which destroy the structure of domains, which in addition can be distorted by any flow of the solvent.

The confined phase separations took place in open ended PDMS microfluidic channels, the construction of which is described in chapter 2. These were approximately 18 μm in height and the other two dimensions were greater than 1 mm such that the system is only confined in one plane. The cells were placed on the microscope stage in the direction perpendicular to gravity (see figure 7.2 (b)). The sample was homogenised, then the cell filled by capillary action. The demixing of each sample was imaged in both the xz and xy planes. In the xz plane we use a 63x magnification lens to study a slice a distance away from any vertical confining edge, and in the xy images we focus to a central plane between the walls using a 10x magnification lens. Unfortunately it is not possible to observe the sample until full equilibrium is attained, as after a time which is dependent on the composition of the solvent, the sample will begin to dry through the open ends of the cell. Once the cell has filled, the flow of the sample slows down dramatically, but does not stop flowing completely in all cases. This is likely to be due to a slight unevenness of the microscope stage, or remaining small pressure differences between either end of the cell. Residual flow is more prevalent in

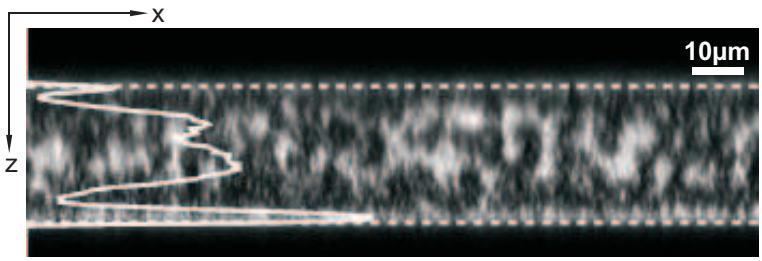


Figure 7.3: Example of image analysis in the xz plane. The full white line represents a plot of the average intensity per row. The dashed white lines represent the walls as located by the analysis explained in section 7.3.2.

samples of lower viscosity, and is a sufficiently large problem for sample 4 that we are unable to obtain a representative timeseries in the xz plane.

7.3.2 Analysis

The coarsening rates in the bulk and in the xy plane of the confined systems were determined by performing 2-dimensional discrete Fourier transforms (FFT) on each of the images [7,125]. The structure factors, $I(k,t)$, where I is the intensity of the image and k is the wavevector, were obtained by radially averaging the Fourier transforms. The wavevector at the maximum intensity $I_{max} \equiv I(k_{max},t)$ was obtained by fitting a Gaussian curve to the data. The correlation length in the system corresponds to $L = L_{image}/k_{max}$ where L_{image} is the image width and the coarsening rate in the system is obtained by plotting L against time (see chapter 5 for more details).

Analysis in the xz plane was performed in a similar manner to our analysis of phase separation at a single wall in chapter 6. Average intensity plots in the z direction were created by averaging the intensity across each row in the xz image (for example that in figure 7.3). As the fluorescence detector in the microscope does not respond linearly to the colloid density, the intensity profile provides an indication of the density distribution of the sample, but is not a true representation. The position of each wall was located by first binarising the images, then creating average intensity plots of the binarised images in the xz plane. These were numerically differentiated, and the locations of the walls identified as the positions of the steepest gradients in the positive and negative directions. An example

snapshot showing the positioning of the walls located by this analysis is shown in figure 7.3. To calculate the thicknesses of the wetting layers, the turning points of the unbinarised xz intensity profiles were located by numerical differentiation. Traveling into the sample, the wetting layer thickness was taken as the width of the intensity peak at the height halfway between the first two stationary points. The lower wetting layer is considerably less distorted due to scattering, thus we have used this data to explore growth patterns. The refractive index mismatch between the immersion oil and the sample causes an elongation of the image which we correct for as described in [172], where we use the estimated refractive index of the solvent as a representation of the refractive index of the sample.

The correlation length of the system obtained from FFT analysis does not correspond to the size of domains, rather the gaps between them [202], as we have confirmed by thorough exploration. When a sample is asymmetric in composition, the correlation lengthscale is not representative of the diameter of drops; to obtain this information, we process the images using the freely available '*ImageJ*' software [203, 204]. First the images were binarised, then the 'analyse particles' feature used to identify and outline domains. The software provides information about the centre of mass, area, and perimeter of each object located, in addition to the total number and area fraction of all domains combined. The diameter of circular domains may be calculated using the basic $A = \pi(d/2)^2$ formula. This type of image processing only provides representative information about the phase separation process when there is sufficient contrast between the two phases such that domains may be clearly and correctly identified. It also follows that the analysis is only satisfactory when domains are confined to two dimensions, such that there is no overlap, and sizing is performed through the same plane of every droplet.

7.4 Bulk phase separations

In figure 7.4 we observe the phase separation of each sample in an unconfined geometry. Sample 1 separates by the nucleation and growth mechanism; the liquid phase is in the minority and forms droplets. Samples 2 and 3 demix via spinodal decomposition and exhibit the characteristic interconnected network morphology. The composition of the samples is

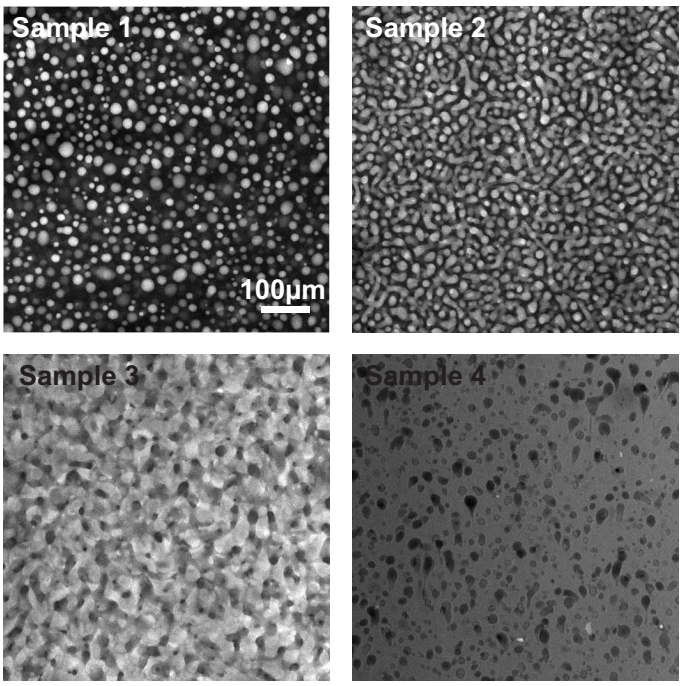


Figure 7.4: CSLM images of the bulk phase separation of samples 1-4.

such that sample 3 has a much higher content of the liquid phase than sample 2. Sample 4 separates by the nucleation and growth mechanism similar to sample 1, but here the gas rather than liquid phase is in the minority, and forms bubbles. In both samples 1 and 4, the system coarsens by the diffusion and coalescence of droplets, rather than Ostwald ripening. In all cases once the domains reach a size approximately equal to $2\pi L_c$ [7, 78], buoyancy forces become dominant and the denser liquid phase sinks to the bottom of the container.

In figure 7.5 we quantify the coarsening rates of these bulk phase separations by plotting the characteristic lengthscale of domains (L) against time. The separation of samples 3 and 4 is significantly quicker than that of samples 1 and 2 due to the lower viscosities of the solvents. We observe that the demixing of samples 2 and 3 proceeds in the linear regime of spinodal decomposition, and perform a linear fit on the data as denoted by the black full lines. Samples 1 and 4 coarsen via diffusion and coalescence, roughly according to the power law $L \sim t^{1/3}$. For all samples we see the lengthscale of the system diverge around 40-60 μm, as structures are ripped apart by buoyancy forces and separation becomes driven by gravity. This indicates that by confining a sample between plates 18 μm apart, we restrict it to a dimension 2-3 times its capillary length.

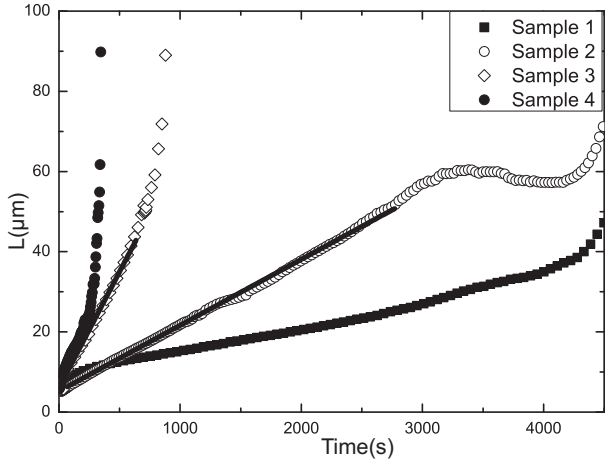


Figure 7.5: Characteristic lengthscale L plotted against time for samples 1-4. The black lines denote linear fits to the data of samples 2 and 3.

7.5 Confined systems

We now consider the confined demixing of samples 1-4 in two sections. ϕ_L represents the equilibrium composition of the liquid phase, and ϕ_G the composition of the gas phase, see table 7.1. We shall first explore the separation of samples from the metastable region of the phase diagram demixing via the nucleation and growth mechanism, sample 1 where the wetting phase is in the minority, and sample 4 where it is in the majority. We will then study samples 2 and 3 which demix by spinodal decomposition. Sample 2 contains significantly less of the liquid phase than sample 3. In all cases it is clear from the CSLM images in the following sections that the bright liquid phase completely wets the walls.

7.5.1 Metastable systems

Sample 1 - Wetting phase is in the minority $\phi_L << 1/2$

In figure 7.6 we observe the demixing of sample 1 confined between two parallel plates 18 μm apart. In figure 7.6 (a) we observe the phase separation in the central plane parallel to the cell wall (xy plane), and in figure 7.6 (b) we study the phase separation perpendicular to the surfaces (xz plane).

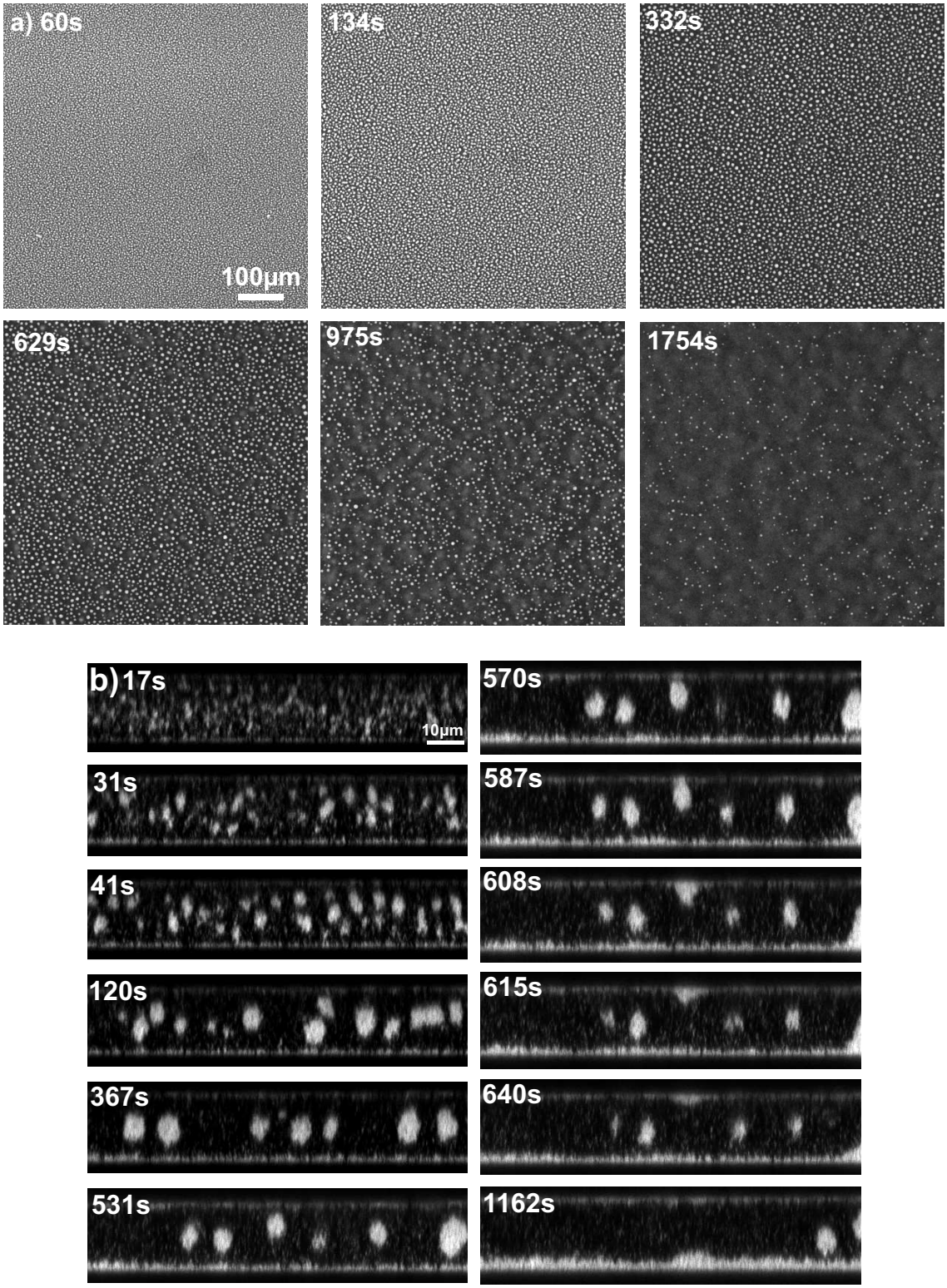


Figure 7.6: CSLM images of the phase separation of sample 1 in an 18 μm wide cell. The upper images are in the xy plane, and the lower images are in the xz plane.

Immediately after the cell is filled, we see a thin wetting layer of the liquid phase form on both surfaces (figure 7.6 (b) 17s), and the material in the centre of the cell demixes via the nucleation and growth mechanism (figure 7.6 (a) 60s, 134s, (b) 17-120s). As the phase separation progresses, the wetting layers thicken, and a layer depleted of the liquid phase forms adjacent to each surface (figure 7.6 (a) 134s, (b) 41s, 120s). The droplets grow generally by coalescence on each other, and as they increase in size they line up along the central axis between the plates (figure 7.6 (a) 332, (b) 367s, 531s). The distance between a droplet and the wetting layer becomes smaller than the interdroplet distance, and after around 300s, we observe that the droplets begin to disappear (figure 7.6 (a) 332-1754s, (b) 531 - 1162s). The droplets diffuse across the depletion layer and coalesce on the cell walls, and the liquid phase material spreads out over the whole wetting layer. We see a sequence of images showing the coalescence of a droplet upon the central region of the upper wall in the later images in figure 7.6 (b). As an increasing number of droplets coalesce on the wetting layer, very few droplets remain in the central region and almost all coalescence events become between droplets and the walls. The system moves towards its equilibrium state, where two liquid wetting layers sandwich a layer of the gas phase, and all remaining droplets in the centre of the plates have coalesced on the surfaces. We observe in the final xz image (figure 7.6 (b) 1162s) that the lower wetting layer is thicker than the upper one, indicating that gravity has slightly influenced the demixing of the system.

We quantify our observations in figure 7.7. In figure 7.7 (a) we compare the FFT analysis of bulk and the confined system in the xy plane. We see that at early times, both geometries follow a similar growth pattern. There is a small quantitative difference in correlation lengthscales, likely to be attributable to the 3 dimensionality of the droplet distribution in the bulk phase separation, compared to the confined case where the droplets line up along the central plane of the cell in 2 dimensions. After around 500s the correlation length in the confined geometry levels off as the growth of the droplets becomes restricted by the surfaces. This lengthscale then diverges as droplets coalesce on the walls, and remaining droplets become increasingly far apart. The bulk correlation length grows approximately as $L \sim t^{1/3}$ throughout.

We investigate the growth of the droplet diameter by analysing our xy plane images using

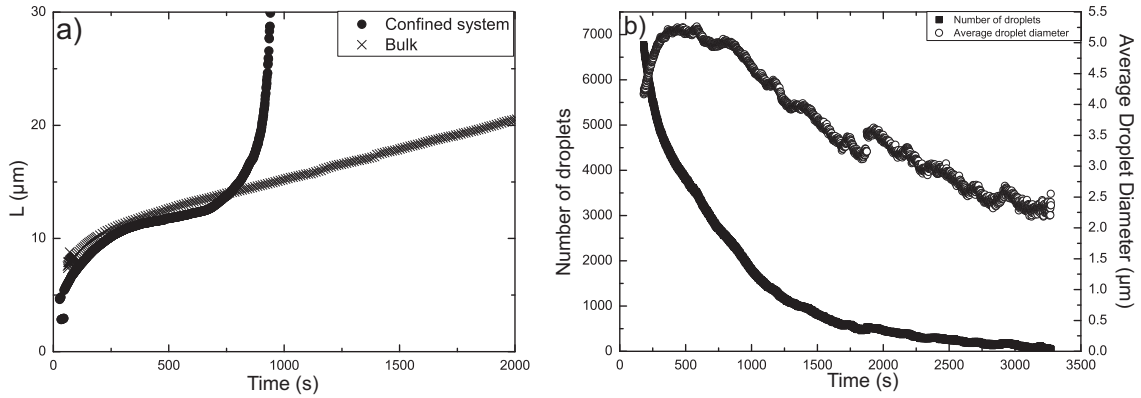


Figure 7.7: (a) Comparison of domain growth by FFT analysis of sample 1 in the xy plane in the bulk and confined systems. (b) Analysis of droplet size and number via the *ImageJ* software.

the *ImageJ* software. We plot the results of this analysis in figure 7.7 (b). In the initial stages of phase separation, there is a large number of small drops that overlap, therefore the software cannot identify individual domains. The droplets in the cell grow quickly to a maximum size of approximately 5μm at 500s. The time at which this peak diameter occurs roughly corresponds to the time at which the correlation lengthscales obtained from FFT analysis start to differ in value in confinement and the bulk. We are unable to obtain any indication of the growth law for the droplet diameter as they coarsen to their maximum size quickly. After 500s, the average droplet diameter decreases as the droplets diffuse out of the central plane between the plates (meaning the image plane is no longer through their centre), coalesce on the wetting layer and spread out. This corresponds to a rapid decrease in the number of droplets detected between the plates. After the initial formation of many droplets, the number of droplets detected between the plates decreases at a rate controlled by the number of coalescence events between droplets, and between droplets and the walls. The rate of coalescence between droplets decreases as they become far apart, and all coalescence becomes between the drops and the walls.

Figure 7.8 (a) shows the average intensity per row of the xz plane images, plotted as a function of the distance from the lower wall of the confinement cell. The degree to which this profile is influenced by scattering is dependent on the colloid distribution through the

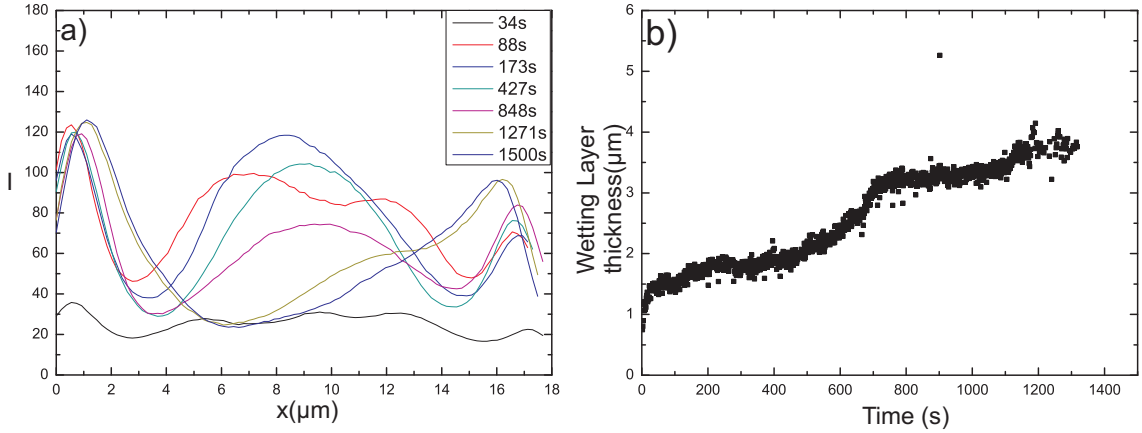


Figure 7.8: (a) Average intensity per row in the xz plane as a function of distance from the lower wall for sample 1. (b) Thickness of the lower wetting layer plotted against time.

sample, which changes as demixing progresses. The distortion of the intensity profile affects the accuracy of the location of the walls, which are found using the method described in section 7.3.2. The profile is cut off at the position of the upper wall.

At the start of measurement (7s), the profile shows a small peak and trough, indicating that the wetting and depletion layers form in the very early stages of demixing. Scattering effects mask these fluctuations close to the upper wall, however similar layers may be observed on this surface in the CSLM images. As phase separation progresses, the wetting and depletion layers at both walls thicken. A third peak in the centre of the cell emerges as the droplets grow in size and line up along the central plane of the cell (41-553s). As these droplets coalesce on the surfaces, we see the wetting layers continue to thicken and the central peak fades as the liquid phase relocates to the cell walls (893s).

We plot the thickness of the lower wetting layer as a function of time in figure 7.8 (b). We see the wetting layer grows quickly in the very initial stages as a layer of liquid phase completely coats the cell walls. Further growth appears reasonably constant but is not smooth. The collision of a single droplet with a particular part of the wetting layer in the image plane causes significant thickening in this region, which then thins again as the droplet spreads out over the whole surface. We shall further discuss the growth of the wetting layer in section 7.6.

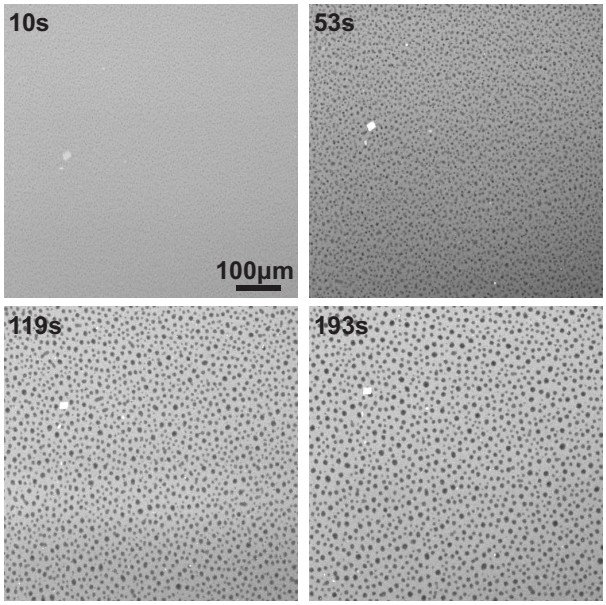


Figure 7.9: CSLM images in the xy plane of the phase separation of sample 4 in an 18μm wide cell.

Sample 4 - Wetting phase is in the majority, $\phi_L >> 1/2$

Next we consider the confined phase separation of a sample separating via the nucleation and growth mechanism, where the wetting phase is in the majority. Unfortunately, due to the nature of systems with a glycerol-water solvent, it was not possible to produce a sample with both a high viscosity solvent and a high composition of the liquid phase. Additionally there is a low concentration of polymer in this sample, meaning phase separation occurs extremely rapidly due to the low viscosity of the sample as a whole. This also has the implication that the residual flow in the cell after filling remains significant, and it was not possible to obtain useful images in the xz plane due to shear effects.

We show the confined demixing of sample 4 in the xy plane in figure 7.9. Initially, gas bubbles form and coarsen via the nucleation and growth mechanism, similarly to what is observed in the bulk (figure 7.9 10s, 53s). As the bubbles coalesce and expand, they line up along the central plane of the cell. Although we are unable to obtain images in the xz plane, we see that the bubbles are distributed over 3 dimensions in the bulk geometry (figure 7.4), but are forced into 2 dimensions in the confining cell (figure 7.9 119s). It is unclear whether the bubbles remain spherical or are flattened by the confining walls into elongated disks as

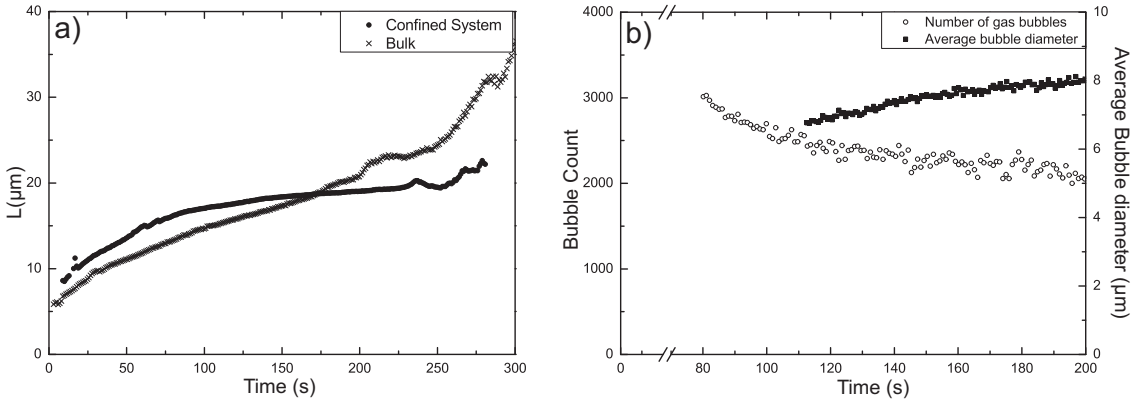


Figure 7.10: (a) Comparison of the correlation lengthscales obtained by the FFT analysis of sample 4 in the xy plane in the bulk and confined systems. (b) Analysis of the change in droplet diameter and number via analysis with the *ImageJ* software.

they expand. As the bubbles become larger, they also spread further apart. This means that the number of coalescence events decreases and the growth of the bubble diameter becomes very slow (193s). Unfortunately it is only possible to observe the confined phase separation for around 200s as this sample dries quickly, however we expect the bubbles would continue to diffuse and coalesce very slowly.

We quantify our results in figure 7.10. Plot (a) shows a comparison of the correlation lengthscale obtained by FFT analysis in the bulk and confined geometries. We see that although there is a quantitative difference between the two lengthscales, they coarsen at a similar rate for the first 50s. This mismatch could be due to the dimensionality difference of the droplet pattern in the two geometries, or could be due to the more significant effect of shear on this sample. The growth rate in the confined geometry slows considerably after around 100s as droplet coalescence becomes limited by the presence of the surfaces. In figure 7.10 (b) we use the *ImageJ* software to plot the number and diameter of droplets as a function of time, although we are unable to differentiate the droplets satisfactorily until around 80s. We observe that the number of bubbles decreases as coalescence occurs and the bubbles expand. As the bubbles become further apart, these coalescence events become less frequent.

Discussion - Demixing of off-critical samples 1 and 4, $\phi_L << 1/2$ and $\phi_L >> 1/2$

The behaviour of our confined samples separating via the nucleation and growth morphology is consistent with the previous experimental observations of Tanaka [193]. When the wetting phase is in the minority (sample 1), we expect the droplets to coarsen as $a \sim t^{1/3}$, until their diameter becomes restricted by the plate spacing [73, 74]. We are unable to comment on the growth of the droplet diameter due to the short timescale over which this is measured, however from the FFT analysis we see that initially, the correlation lengthscale of the material in the centre of the plates coarsens at a similar rate to that in the bulk (figure 7.7 (a)). This is consistent with the observation that at early times the system in the centre of the cell also coarsens by the coalescence of droplets with one another. As the droplets become larger, coalescence of the droplets on the wetting surface becomes more frequent as the interdroplet spacing becomes wider than the depletion layer. The rate of decrease in the number of droplets between the plates (figure 7.7 (b)) is dependent on two processes: the coalescence between droplets, and the coalescence of droplets with the walls. The rate of each of these is dependent on droplet size and distribution throughout the cell. In the early stages, coalescence between small droplets is frequent, where as at later times the coalescence of larger droplets on the walls is the dominant process.

When the non-wetting phase is in the minority (sample 4), we expect the gas bubbles to coarsen in a similar manner to their behaviour in the bulk until their diameter becomes limited by the plate spacing. Due to the wetting preference of the surface, none of the bubbles at the edge of the cell spread on the surface. As the bubbles grow, they become constricted by the plate spacing and the dimensionality of the coarsening droplets slowly crosses over from 3 dimensions to 2 dimensions. The rate of decrease in the number of bubbles is only dependent on the rate of their coalescence with each other. As we have no CSLM images for this sample in the xz plane, it is unclear if the bubbles remain spherical, or are further constricted into disk shapes as they expand. As the maximum bubble diameter is 8μm, it seems probable that the bubbles remain spherical.

Once the system has crossed to two dimensions, the bubbles continue to grow by diffusion and coalescence. The previous experiments of Tanaka on polymer blends [193] indicate further growth as $a \sim t^{1/3}$ consistent with the L-S growth law (for dimensions greater than

1) [74], whereas the diffusion coagulation mechanism predicts bubble growth as $a \sim t^{1/D}$ where D is the dimensionality of the system [73] (see further discussion in [178]). It has not been possible to determine a growth law for the diameter of our bubbles as they exhibit slow growth over the timescale that we are able to record (figure 7.10 (b)), although from the FFT analysis (figure 7.10 (a)) we clearly see the correlation lengthscale of the system affected by the surfaces. There is no indication of any attraction between bubbles, although this could be difficult to detect on the timescale of our observations. Such an effect has been proposed either through convection due to concentration gradients [166, 200], or through a backflow mechanism [181, 201]. It seems unlikely that a backflow interaction through the wetting layers would occur as the droplets are small and well spaced [193].

7.5.2 Spinodal decomposition

We shall now study two samples demixing via spinodal decomposition between two plates. We differentiate samples 2 and 3 by their equilibrium compositions of liquid and gas phases; sample 2 is composed of approximately 25% liquid phase, and sample 3 70% of the liquid phase (see table 7.1 for details). We refer the reader to section 7.2 for a review of previous observations of the demixing of similar systems.

Sample 2 - Spinodal decomposition, $\phi_L < 1/2$

We observe the confined demixing of sample 2 in figure 7.11. Immediately after the cell is filled, a thin layer of the liquid phase coats each of the walls (figure 7.11 (b), 5s). The material in the centre of the tube begins to separate into a spinodal network structure (figure 7.11 (a), 19s, (b)43-85s). It appears in the very early cross-sectional images that the thin spinodal tubes may be connected to the wetting layer, however as the wetting and depletion layers are established, these connections break. As the system coarsens, the network structure partially breaks up as there is not enough of the liquid phase present for domains to remain bicontinuous (figure 7.11 (a) 392s, (b) 186s). To reduce their interfacial area, these structures reshape to become 2 dimensional elongated disks, and line up on the central plane between the plates (figure 7.11 (a) 790s, (b) 432s). The droplets diffuse and coalesce on each other, or disappear as they coalesce on the wetting layer and spread out over the wetting surfaces

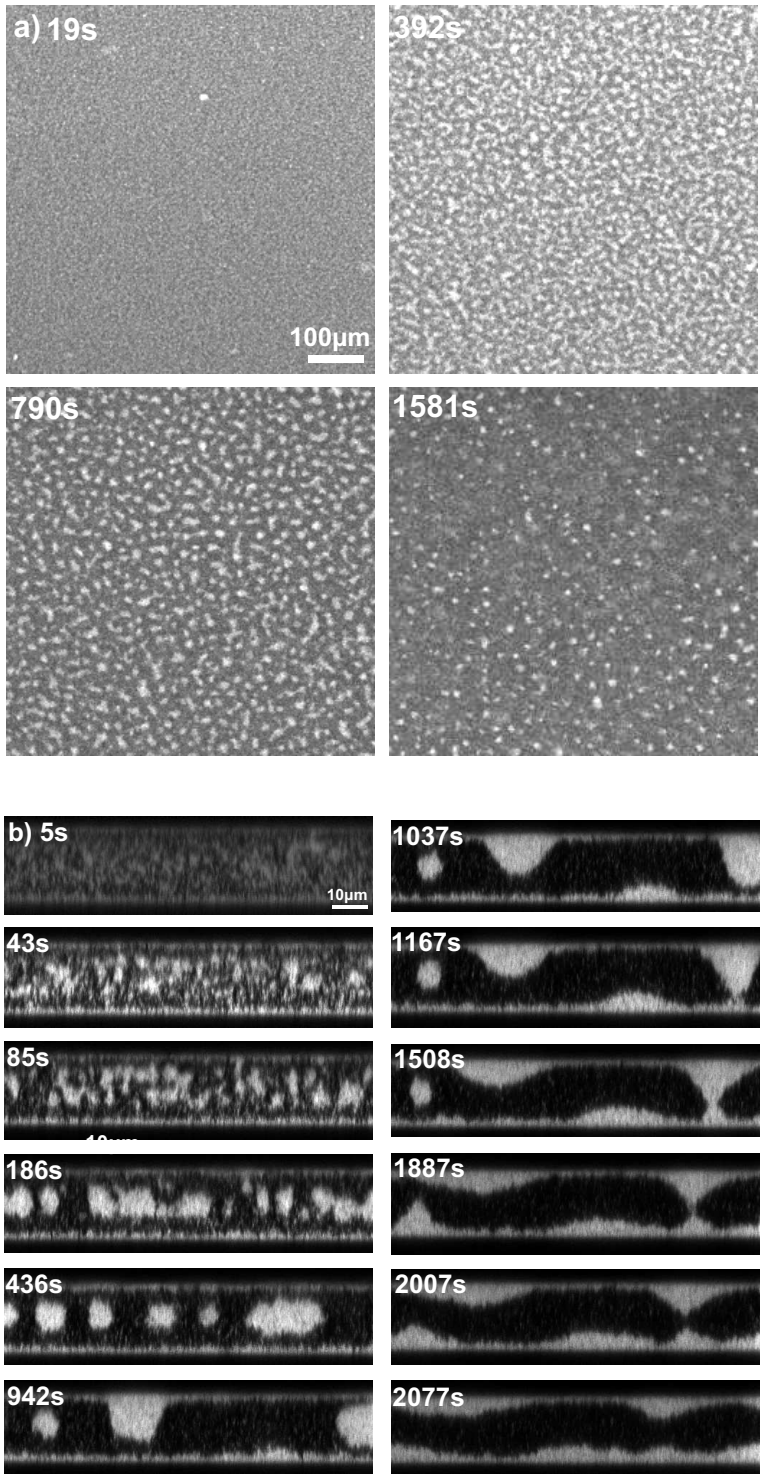


Figure 7.11: CSLM images of the phase separation of sample 2 in an 18 μm wide cell. The upper images are in the xy plane, and the lower images in the xz plane.

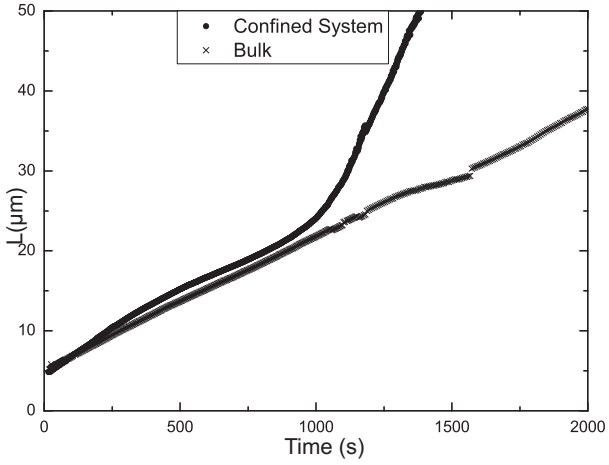


Figure 7.12: Comparison of domain growth by FFT analysis in the xy plane in the bulk and confined systems.

(figure 7.11 (a) 1591s, (b) 942-2077s). Once the domains break up, the morphology resembles that of sample 1, however in this case the size of the droplets is not uniform. Occasionally we observe the formation of a bridging tube connecting the wetting layers (see the right hand edge of figure 7.11(b) 1037-2077s). The width of this bridge is thinner than the plate spacing, therefore the pressure gradient pushes the liquid phase out of the tube and into the wetting layer. The tube runs out of material, and the connection severs. The formation of this bridge may be a result of a few central domains remaining connected to the wetting layers; as the system coarsens, these connected domains transform into a circular bridging droplet, as described in section 7.2. Alternatively both edges of a particularly large droplet may coalesce on the different surfaces simultaneously. In any case the system moves towards an equilibrium where the two wetting layers sandwich a layer of the gas phase, and all the droplets in the centre of the plates have coalesced.

In figure 7.12 we quantify our observations by comparing the correlation lengthscale of xy plane images in confinement and in the bulk. At very early times, the correlation length in both geometries is very similar - the still interconnected network in the central plane between the plates resembles the structure in the bulk. The lengthscales continue to grow at a similar but not identical rate, potentially due to the difference in coarsening behaviour between a full 3 dimensional network and a flatter network that begins to break up. After

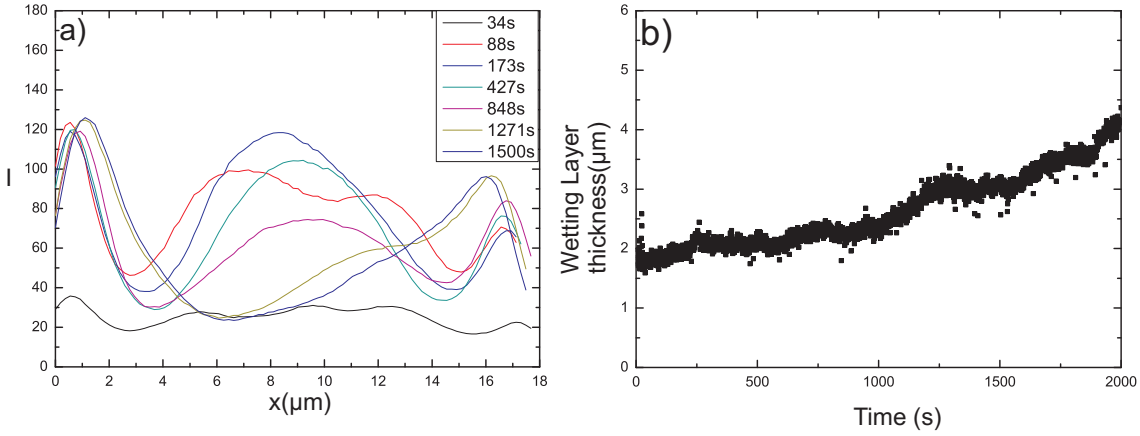


Figure 7.13: (a) Average intensity per row in the xz plane as a function of distance from the lower wall for sample 2. (b) Thickness of the lower wetting layer plotted against time.

1000s the correlation lengthscale in the confined sample diverges, as the droplets coalesce on the walls of the cell, and the remaining drops become increasingly far apart. We are unable to quantify the approximate sizes of domains using the *ImageJ* software due to the bicontinuous nature of the structure and the difficulty in identifying distinct domains.

Figure 7.13 (a) shows the development of the averaged intensity per row in the xz plane plotted as a function of the distance from the lower cell wall. Initially (34s), the profile does not show a great deal of structure, however the peaks and troughs associated with the wetting and depletion layers quickly develop and widen as the system coarsens (88-847s). A third peak emerges in the centre of the plates as the liquid domains line up on the central axis, which then flattens as the droplets coalesce on the cell walls (1271s, 1500s). In figure 7.13 (b) we plot the wetting layer width against time. This has significant thickness from the outset, as initially the liquid phase may be quickly transported to the surface via the spinodal network. These connections are rapidly severed, and the wetting layer appears to grow at a reasonably constant rate. There are some fluctuations as droplets in the image plane coalesce on the surface, then spread out across the whole wetting layer. We shall further discuss the growth of the wetting layer in section 7.6

Discussion - Demixing of sample 2, $\phi_L < 1/2$

The confinement of sample 2 has a distinct effect on the morphology of its phase separation. When demixing in the bulk, it forms a spinodal network structure, which remains bicontinuous as the system coarsens. This suggests that the system would be expected to follow the morphology of a critical sample when demixing between two plates as described in section 7.2, forming a 3 dimensional network structure which coarsens into a set of circular droplets bridging the two plates [166, 181, 201]. We observe that the initial loss of the liquid phase to the formation wetting layers alters the average composition of the material in the centre of the cell, and consequently alters the morphology of demixing. The low availability of the liquid phase in the depletion layers means the network in the centre of the cell is unable to remain connected to the wetting layers. This is a similar effect to that observed at a single wall in chapter 6 (case 3). Later, the lower volume of liquid phase available in the central region means that as the system coarsens, the liquid domains are unable to remain bicontinuous, and break up into droplets of varying size [76]. Such an effect has previously been observed in binary fluids, where the loss of wetting phase material to surfaces shifts the morphology of the demixing material between them from critical to off-critical [195].

In figure 7.13 (a) we plot the averaged intensity profile of sample 2 along the z direction, perpendicular to the plates. At early times small peaks and troughs are present, corresponding to the wetting and depletion layers. There is some evidence of further layered structure in the centre of the cell, however this is largely masked by scattering effects. As the system coarsens, the wetting and depletion layers next to each wall widen, and the liquid phase in the centre of the cell is pushed towards the central plane. This results in the emergence of a third peak in the centre of the intensity profile. Although demixing in samples 1 and 2 proceeds by different mechanisms, the disconnected liquid droplets observed in sample 2 behave in a similar manner to droplets which form via the nucleation and growth mechanism in sample 1. The intensity profiles form the same patterns, as can be seen by comparing figures 7.8 (a) and 7.13 (a). Presuming each surface has an equal preference for the wetting phase, once the liquid becomes concentrated in the centre of the cell, the depletion layers are unable to grow further as this would produce an unfavourable interaction of the liquid droplets with the opposite wall. Further coarsening of the system is governed by the diffusion

of the liquid phase droplets and their coalescence on the wetting layer.

The evolution of the intensity profiles bears a resemblance to the observations in [190,191], where oscillating density fluctuations originating from the two confining surfaces interact and create patterns of constructive and destructive interference. We take care with this comparison as our intensity profiles are not true composition waves, and it is not clear if our systems are in comparable demixing regimes.

Sample 3 - Spinodal decomposition, $\phi_L > 1/2$

We now consider demixing of sample 3 which decomposes via spinodal decomposition with the wetting phase in the majority. In the initial stages, we see a 3 dimensional spinodal network form between the plates, connecting the wetting layers. A thin layer of the liquid phase coats the walls from the outset (figure 7.14 (a) 105s, (b) 7-104s). As the system coarsens, the tube structure of the spinodal network becomes thicker, and the wetting layers grow as material is transported from the network to the surface. The presence of the wetting layers prevents the domains growing symmetrically in 3 dimensions, so the network structure transforms into a set of cylindrical tubes connecting the two wetting layers (figure 7.14 (a) 247s, (b) 56-180s). In the xy plane the cross sections of these bridging droplets appear as bright spots, and signify the transformation of the 3 dimensional spinodal network to a 2 dimensional bridging droplet morphology. As demixing progresses, the larger bridges grow in diameter, whereas the smaller ones shrink and the connection between the plates snaps (figure 7.14 (a) 247-973s). In the xz plane, we see that whilst the structure is a 3 dimensional network, the wetting layers thicken (figure 7.14 (b) 56-180s), but once the system becomes a set of bridging droplets expanding in the xy plane, the wetting layers thin again (figure 7.14 (b) 462-1943s). This illustrates the direction of the flow through the spinodal tubes. Whilst the wetting layer is connected to the spinodal network, the Laplace pressure directs the flow of the liquid phase into the wetting layers. Once large bridging droplets of size greater than the plate spacing have been established, the pressure gradient changes direction, and the droplets grow as they feed on the wetting layer. After around 1100s, the circular droplets begin to collide. The 2 domains attempt to regain a circular shape to minimise their interfacial area, however collisions are frequent and the morphology becomes partially

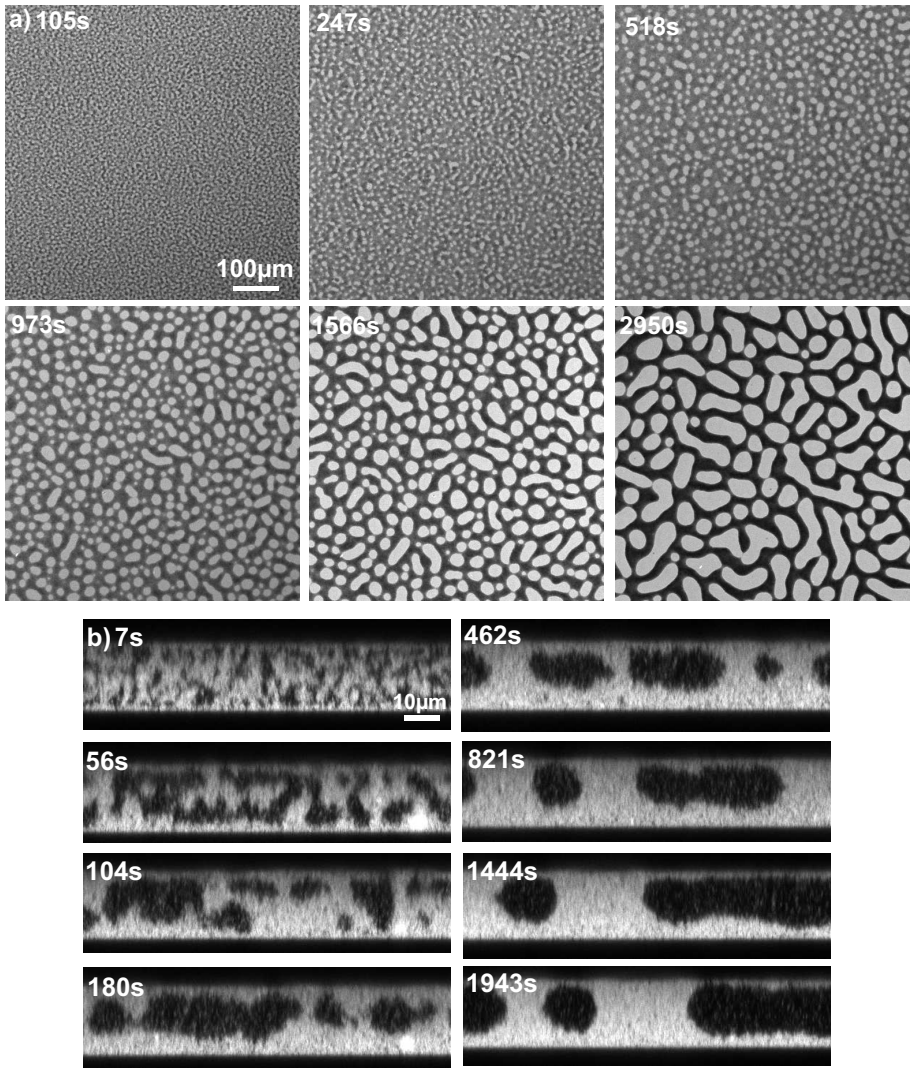


Figure 7.14: CSLM images of the phase separation of sample 3 in an 18 μm wide cell. The upper images are in the xy plane, and the lower images in the xz plane.

interconnected (figure 7.14 (a) 973-2950s). In the xz images (figure 7.14 (b) 180-1943s), we observe that the wetting layer on the lower surface is slightly thickened, and the curvature of the interface of the bridging droplets is slightly distorted from symmetrical. This illustrates a small effect of gravity on the demixing of the system.

We compare the correlation lengthscale obtained from FFT analysis in the bulk and confined geometries in figure 7.15 (a). Initially, the two lengthscales coarsen at a similar rate. After around 500s, by which time the system has clearly crossed over to the bridging droplet morphology, coarsening in the confined geometry slows. We are unable to quantify

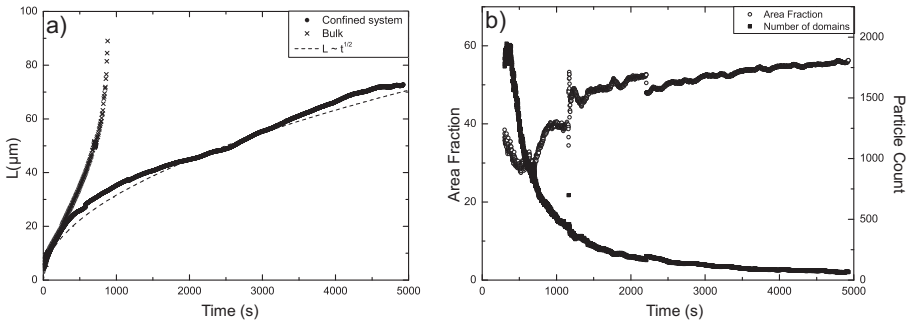


Figure 7.15: (a) Comparison of FFT analysis of bulk and confined samples in the xy plane for sample 3. The dashed line represents the function $L \sim t^{1/2}$ (b) *ImageJ* analysis of coarsening domains in the xy plane - plot of area fraction and particle count with time.

the wetting layer and intensity profile evolution in the xz plane except at very early times, as upon averaging the bridging droplets mask the wetting and depletion layer fluctuations.

Once the bridging droplet morphology becomes established, we are able to identify cross sections of the bridges in the xy plane, and use the *ImageJ* software to calculate the number and area fraction of these domains. In this case we do not use the software to obtain information about the domain diameter, as this relies on their being circular, which is not a valid assumption at later times. The discontinuities in this data correspond to the adjustment of the gain and offset settings on the microscope, which affects the binarising feature of the software.

In figure 7.15 (b) we plot the number of liquid domains and the domain area fraction against time. We observe the number of domains peaks around 500s. The number of domains then decreases rapidly as bridging droplets smaller than the critical radius shrink and disappear, and bridges of any size collide. The decrease in the number of domains slows down as the domains become further apart and collide less frequently.

The change in area fraction in the xy plane reflects the volume of liquid phase in the wetting layers. On equilibration, the sample is estimated to contain 70% of the liquid phase and 30% of the gas phase. In the absence of confinement, once the two phases have reached their equilibrium compositions we would expect the area fraction of liquid domains to reflect this ratio, whatever the correlation length in the system. Initially the area fraction of domains in the central plane is less than 40%, indicating that there is a significant amount of the liquid

phase present on the surfaces. The area fraction fluctuates until around 750s, presumably due to the competition between larger 2 dimensional droplets pulling the material into the central plane as they expand, and the material from the smaller droplets flowing into the wetting layers as they shrink and disappear. Once these thin connections have severed, the majority of the liquid phase is flowing from the wetting layers into the large bridging droplets. The wetting layer thins, and the area fraction of liquid domains in the centre of the plates increases. At later times, the area fraction stabilises as the wetting layer runs out of material to feed the droplets, although the fraction of liquid phase in the central plane never reaches its equilibrium composition due to the coatings on the walls.

Discussion - demixing of sample 3, $\phi_L > 1/2$

Our study of the demixing of sample 3 confined between two plates is consistent with previous predictions and experimental observations [166, 194, 201]. We observe 3 stages of phase separation: a 3 dimensional spinodal network, which coarsens into a system of 2 dimensional circular droplets bridging the two surfaces, then transforms into a partially interconnected network in 2 dimensions.

During the initial stages of demixing, we expect the spinodal network structure in the centre of the plates to coarsen as $L(t) \sim t^1$ [78]; the coarsening of the domains and the thickening of the wetting layer are driven by hydrodynamic processes [78, 168, 193]. Once the morphology transforms into a system of circular bridging droplets, droplets of diameter $2a > d$ are expected to grow with the same exponent. The correlation lengthscale of our confined system grows linearly in time until around 500s. We equate this lengthscale to the domain size at these early times, as the diameter of the liquid domains is roughly equal to their spacing [202]. It is difficult to pinpoint when the spinodal network transforms into a system of bridging droplets where growth is governed by gradients in the Laplace pressure. The images in figure 7.14 (b) suggest there may be some time between the 3 dimensional structure coarsening into bridging droplets, and the curvature of the interfaces being established.

By 500s the system clearly consists of 2 dimensional circular droplets bridging the two surfaces. Visual analysis indicates that droplets approximately wider than the plate spacing

grow, whilst those smaller shrink, however frequent collisions between the droplets make the critical radius for expansion hard to quantify. The droplets begin to collide reasonably soon after their formation, indicating that they feel an attraction by feeding on the same material from the wetting layers at an early stage. As the spacing between the droplets is not much greater than their diameter (see figure 7.14 (a) 247-516s), this is perhaps unsurprising as there is only a small area of wetting surface on which to store liquid phase material. The collisions between domains transforms the system into a partially interconnected network morphology. We note that we observe the presence of 3 dimensional spinodal network, 2 dimensional bridging droplet and 2 dimensional network morphologies (although our 2 dimensional network never becomes fully interconnected), but it is difficult to distinguish crossovers between regimes, suggesting there may be times when more than one coarsening mechanism plays a role.

After around 1000s all droplets smaller than the critical radius have disappeared, and we observe the growth of larger domains. As their lengthscale increases, the area fraction of liquid domains across the central plane parallel to the plates also increases. This indicates that the domains grow by feeding on material in the wetting layers, drawing the liquid phase back into the central plane [201]. If such a backflow mechanism did not play a role, and the growth of domains was driven by diffusion or phase coarsening, we would not expect the area fraction of domains to increase as they expand. It would be surprising if phase coarsening played any part in domain growth at this late stage, as we expect the phases in our colloid-polymer mixture to have reached their equilibrium compositions by the time the system is in the linear spinodal regime, and sharp interfaces have formed [7].

There is currently no consensus on the expected growth rate of the 2 dimensional interconnected network. Tanaka predicts that the circular bridging droplets should grow as $a(t) \sim t^1$, crossing over to $a(t) \sim t^{1/3}$ once they begin to interact [166, 181]. Wang and Composto observed logarithmic growth across the whole 2 dimensional regime [201], and comment that the data of Tanaka also fits this law [166,181,201]. An overlay of the function $L(t) \sim t^{1/2}$ in figure 7.15 (b) represents the growth of our domains reasonably well, although this coarsening is faster than previous experimental observations. We note that the 2 dimensional domains in our system never become fully interconnected, and quickly attempt

to recover a circular profile after a collision deforms their shapes. The faster growth may be due to a subtlety concerning the radius of curvature of domains, or may be due to the precise interpretation domain lengthscale. Additionally a small amount of flow remains in the cell during coarsening. Although our domains do not become distorted, it does appear that the number of collisions between bridging droplets in the direction of the flow has been enhanced, which would increase the rate of domain growth. The work of Derks *et al.* [52] demonstrates that shear may have a significant effect on demixing of colloid-polymer mixtures.

7.6 Wetting layer growth

In figure 7.16 (a), we compare the wetting layer growth of samples 1 and 2, and the initial growth of sample 3. We are unable to reliably calculate the wetting layer thickness of sample 3 once bridging droplets have formed, as upon averaging across the xz images, the presence of the bridges masks the fluctuations in the intensity profile. We observe that the wetting layers in sample 3 grow much more quickly than in samples 1 and 2, this is expected as in this case the spinodal network remains connected to the surfaces, allowing growth by a faster hydrodynamic process [153, 155, 168]. The layers in samples 1 and 2 develop much more slowly, as growth is limited by the rate of diffusion of liquid phase droplets across the depletion region. We observe some fluctuation in wetting layer growth as droplets coalesce on an area in the image plane, then spread out across the whole wetting surface. We only record the thickness of the lower wetting layer as we cannot reliably measure the width of the upper layer due to scattering effects, however we estimate that in both samples it generally follows the trend of the lower layer with a slightly smaller magnitude. This is likely due to a small effect of gravity on the demixing of our systems, but a small difference in the wetting preference of the liquid phase for the PDMS and glass surfaces may also contribute.

It is difficult to predict a growth law for the wetting layers in our confined systems from previously reported observations, as a large number of systems, in different demixing regimes, have been studied under a variety of degrees of confinement. In the semi-infinite geometry when growth is governed by the diffusion of wetting phase droplets, the wetting layer is predicted to grow as $l(t) \sim t^{1/3}$ or $l(t) \sim \ln(t)$, depending on quench depth and the

strength of the surface field [158, 159]. In chapter 6 we showed the wetting layer at a single wall in contact with a very similar colloid-polymer system to those considered here grew as $l(t) \sim \ln(t)$.

In figure 7.16 (b) we plot the wetting layer thickness of our samples confined between parallel plates against $\ln(t)$. It appears that a logarithmic growth law may apply at early times, although after around 400s in sample 1 and 1000s in sample 2, this function is no longer representative. We note that this corresponds approximately to the times at which the xy plane correlation lengthscales in the bulk and in confinement begin to diverge. It is possible that whilst wetting layer growth is driven by the surface field, it follows the growth law observed for the single wall geometry. The wetting layer grows by the diffusion and coalescence of coarsening droplets, and the depletion layer is free to widen. At some stage, the lengthscale of the droplets becomes restricted by the plate spacing, and they line up on the central plane of the cell. The depletion layer is unable to widen further, due to the presence of these droplets and the proximity of the depletion layer from the opposite surface. Wetting layer growth is now governed by the diffusion of size-limited droplets across a fixed width depletion layer. This is a subtly different mechanism to the early stages, where the wetting layer thickens by the diffusion and coalescence of coarsening droplets across a widening depletion layer, and may well be described by an alternative growth law. We note that at this time the size of the droplets becomes of the order of the capillary length in the system, thus the effect of gravity may begin to drive droplets towards the lower wetting layer. As the upper wetting layer develops with a similar growth pattern, we do not expect the sedimentation of droplets to have significantly affected this process.

7.7 Conclusion

In this chapter we investigated the demixing of our colloid polymer system confined between two parallel plates, both of which are completely wet by the colloidal liquid phase. We studied four samples from differing regions of the phase diagram demixing by both the nucleation and growth and spinodal decomposition mechanisms. We confined our systems to within 2-3 times their capillary length, such that the system is influenced by both surfaces, but is not

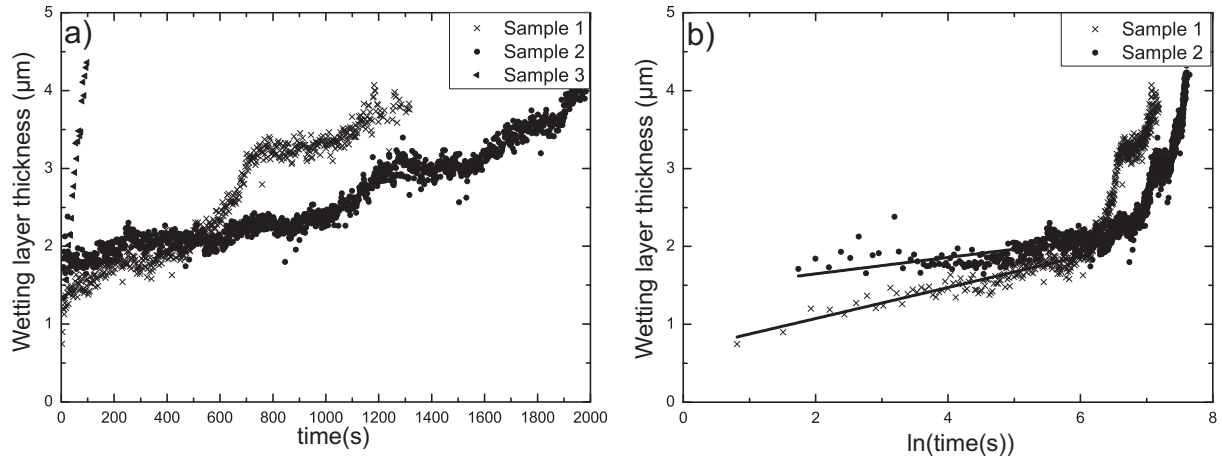


Figure 7.16: (a) Comparison of wetting layer growth in samples 1-3. (b) Plot of wetting layer growth in samples 1 and 2 against $\ln(t)$.

so restricted that we see any finite size effects or evidence of extreme confinement to within a few particle diameters [178,190]. We observe that domains in the centre of the cell coarsen in a similar manner to the bulk, until their size becomes large enough such that it is limited by the presence of the surfaces. After this time the coarsening of the system is determined by the interaction of central domains with the wetting layers, and the dimensionality of the system.

We investigate two samples from the metastable region of the phase diagram, separating via the nucleation and growth mechanism. In one case the liquid (wetting) phase is in the minority and forms drops, in the other bubbles of gas are formed. When the liquid phase is in the minority, we observe a thin layer of this material coats the surfaces at an early stage. The liquid droplets in the centre of the cell grow in size by coalescence with one another, and the wetting layer grows as these drops coalesce on the walls. As the droplets become larger, their diameter becomes limited by the presence of the surfaces, and they line up on the central plane. As an increasing number of droplets coalesce on the walls, the interdroplet spacing becomes larger than the width of the depletion layer, and the majority of coalescence events become between the drops and the surfaces. The system moves towards its equilibrium structure where the two liquid phase wetting layers sandwich a region of the gas phase.

When the gas (non-wetting) phase is in the minority, the liquid phase coats both surfaces from the outset. The gas bubbles nucleate and coarsen by coalescence with one another. As the bubbles become larger, their size becomes restricted by the surfaces, and the dimensionality of their diffusion and coalescence crosses over from 3 to 2 dimensions. As the bubbles are of the non-wetting phase, the only mechanism with which the system coarsens is by the coalescence of gas bubbles on each other.

We also study two systems demixing by spinodal decomposition. In the first case, there is a low fraction of the liquid phase present. As soon as the confinement cell is filled, we observe the formation of a wetting layer on each surface. The initial loss of liquid phase material to the wetting layer alters the average phase composition of the material in the centre of the cell. The reduction in volume of the liquid phase prevents liquid domains remaining bicontinuous as the system coarsens. The network structure in the centre of the cell disconnects from the wetting layers in the very early stages, and further breaks up into droplets as the system coarsens. These droplets then diffuse and coalesce on the wetting layer. We observe that the growth behaviour of the wetting layer may change depending on whether it is limited by the diffusion of coarsening droplets across a growing depletion layer, or by the diffusion of drops of fixed size across a fixed width depletion layer.

The final sample demixes via spinodal decomposition with the liquid phase in the majority. We observe three regimes of demixing. Initially a 3 dimensional spinodal network forms between the two surfaces, connecting the two wetting layers. This structure coarsens similarly to such a network in the bulk, and the wetting layer grows by the hydrodynamic transport of the liquid phase to the surface by spinodal tubes. As these tubes become wider, the network transforms into a system of circular droplets bridging the two plates. The behaviour of the bridging droplets is dependent on both their diameter and the plate spacing, as the relative sizes of the curvatures of the tubes determines the direction of pressure gradient. We see the smaller bridges shrink and the connection between the wetting layers severs, whilst the larger droplets expand. This is consistent with previous observations [193,194,201], however we are unable to obtain a value for the critical radius for which the bridging tubes expand.

Once the system has transformed from a spinodal network to a set of bridging droplets, we observe that the wetting layers start to thin, indicating that the liquid phase begins to

flow away from the surfaces back into the bridging tubes. These domains feel an attraction as they draw on the same material in the wetting layers. The domains begin to collide and the system becomes a partially interconnected network, coinciding with a slowing of the growth of the correlation lengthscale within the system. We observe our system exhibits 3 different morphologies, however we do not observe clear crossovers between them. This indicates there may be times where the system is coarsening with more than one mechanism.

Phase separation in confined geometries has been extensively studied in mixtures of polymers or binary fluids [193,194,201], or in thin films of polymers [190,191]. Our experimental observations are in generally good agreement with previous observations from theory and experiment (see for example the following reviews [149, 178, 193]), although in some cases we have been unable to corroborate the growth laws of domains. This may be due to the differing demixing regimes exhibited by different types of system (to our knowledge this is the first investigation of the colloid-polymer mixtures in this geometry) or the interpretation of the many lengthscales within the demixing systems.

This experimental system and cell construction provides a simple method to study confinement effects on fluid-fluid systems. It is hoped that by constructing more complicated cells, we can extend this method to study demixing, capillary condensation and wetting effects in more exotic geometries [20,205]. It may also be possible to modify one of the surface to alter its wetting preference allowing us to experimentally investigate phenomena such as the interface localisation transition, which has been studied extensively within simulation, but has not yet been observed experimentally [180].

Overview

In this thesis we investigate the interfacial behaviour of confined colloid-polymer mixtures. A colloidal system can be a useful tool to investigate phenomena that are too small or occur too quickly in molecular systems, allowing us to address some of the pertinent questions in statistical mechanics. We begin with a brief description of how the addition of a non-adsorbing polymer to a colloidal suspension can result in fluid-fluid phase demixing. The interfacial tension between these two phases is several orders of magnitude smaller than in molecular systems. We discuss the consequences of this for the static and dynamic properties of our interface.

In chapter 2 we explain how to fabricate simple PDMS microfluidic channels that can be used to confine our system. Previous experimental work exploring colloid-polymer mixtures has been based on systems in an organic solvent, which are incompatible with these cells. We outline the development of a new water based system which can be combined with these devices and the technique of Confocal Scanning Laser Microscopy to study confined colloid-polymer mixtures in real space. One effect of the ultra-low interfacial tension in a colloid-polymer system is that thermal fluctuations of the interface are on the order of microns, and may be observed by optical microscopy. We explain the analysis of these waves, from which we are able to obtain information about the interfacial properties of the system.

The significance of the sedimentation-diffusion gradient within a colloidal system is controlled by the ratio of the height of the suspension to the gravitational length of the colloids. In chapter 3 we studied the interfaces of phase separated colloid-polymer mixtures of identical composition, but varying suspension height. By increasing the suspension height, we increase the importance of the gravitational field, and show that the colloids (and consequently the

polymers) rearrange into an inhomogeneous sedimentation profile, systematically roughening the gas-liquid interface as if it were approaching the critical point. We illustrate how by manipulating the suspension height, we are able to control the distance of the interface from criticality.

In chapter 4 we investigate how such a sedimentation-diffusion gradient is established. The timescale of this process is considerably slower than that of fluid-fluid demixing. As the density profiles of the colloids and polymers rearrange, we observe the system pass through a series of local mechanical equilibria on the way to establishing the full sedimentation-diffusion equilibrium. We show that the beyond a certain height the system locally passes through the gas-liquid critical point, offering a new approach to the study critical phenomena.

In the remaining chapters we investigate the demixing of our colloid-polymer system. In chapter 5 we show that by tuning the properties of the solvent, we are able to access the various regimes of spinodal decomposition. By increasing the solvent viscosity we are able to slow down the demixing process, and observe the diffusive-hydrodynamic regime, which passes in a matter of seconds in the original system. When the densities of the colloids and solvent are closely matched, domains coarsen to large lengthscales before the onset of the gravity driven regime.

In chapter 6 we study the phase separation of our system in the vicinity of a wetting surface. The decelerated demixing process allows us to study the interplay between phase separation and wetting phenomena in detail. We investigate samples separating via the spinodal decomposition and nucleation and growth mechanisms, and demonstrate that the presence of this surface breaks the symmetry of the phase separation morphology in the direction perpendicular to the wall. We analyse the thickening of the wetting layer, and find that hydrodynamic transport processes can significantly enhance growth.

In chapter 7 we study samples of varying composition confined between two parallel plates. We find that domains in the centre of the plates coarsen in a similar manner to the bulk, until they reach a size such that further growth is limited by the surfaces. This restriction transforms the dimensionality of the phase separation from 3 to 2 dimensions. Further development is dependent on the interaction of domains with the wetting layers. Depending on the phase composition of the system, hydrodynamic processes may play an

important role in both the growth of the wetting layers, and the coarsening morphology of the system.

Bibliography

[1] J. Perrin. Atoms. 1916.

[2] W. C. K. Poon. *Science*, 304:830, 2004.

[3] A. van Blaaderen. *Progr. Colloid Polym. Sci*, 104:59, 1997.

[4] W. C. K. Poon, 2002.

[5] D. G. A. L. Aarts, M. Schmidt, and H. N. W. Lekkerkerker. *Science*, 304:807, 2004.

[6] R. Tuiner, J. Rieger, and C. G. deKruif. *Adv. Colloid Interface Sci.*, 103:1, 2003.

[7] D. G. A. L. Aarts, R. P. A Dullens, and H. N. W. Lekkerkerker. Interfacial dynamics in demixing systems with ultralow interfacial tension. *New. J. Phys*, 7(40), 2005.

[8] S. M. Illet, A. Orrock, W. C. K. Poon, and P. N. Pusey. *Phys. Rev. E*, 51:1344, 1995.

[9] S. Auer and D. Frenkel. *Nature*, 409:1020, 2000.

[10] P. Pieranski. *Contemp. Phys.*, 24:25, 1983.

[11] W. C. K. Poon, A. D. Pirie, and P. N. Pusey. *Faraday Discuss.*, 101:65, 1995.

[12] K. N. Pham, A. M. Puertas, J. Bergenholtz, S. U. Egelhaaf, A. Moussaïd, P. N. Pusey, A. B. Schofield, M. E. Cates, M. Fuchs, and W. C. K. Poon. *Science*, 296:104, 2002.

[13] P. N. Pusey and W. van Megaen. *Nature*, 320:340, 1986.

[14] F. Renth, W. C. K. Poon, and R. M. L. Evans. *Phys. Rev. E*, 64:031402, 2001.

[15] V. J. Anderson and H. N. W. Lekkerkerker. *Nature*, 416:811, 2002.

[16] D. G. A. L. Aarts, J. V. van der Wiel, and H. N. W. Lekkerkerker. *J. Phys.: Condens. Matter*, 15:S245–S250, 2003.

[17] W. K. Wijting, N. A. Besseling, and M. A. Stuart. *Phys. Rev. Lett.*, 90:196101, 2003.

[18] M. Dijkstra and R. van Roij. *Phys. Rev. Lett.*, 89:208303, 2002.

[19] R. Evans. *J Phys.:Condens. Matter*, 2:8989, 1990.

[20] M. Schmidt, A. Fortini, and M. Dijkstra. *J Phys.:Condens. Matter*, 15:S3411, 2003.

[21] S. Kluijtmans, G. H. Koenderink, and A. P. Philipse. *Phys. Rev. E*, 61:626, 2000.

[22] A. Patrykiejew, S. Sokolowski, and K. Binder. *Surf. Sci. Rep.*, 37:207, 2000.

[23] M. D. Haw. *J Phys.:Condens. Matter*, 14:7769–7779, 2002.

[24] J. K. Dhont. *An Introduction to Dynamics of Colloids: Studies in Interface Science*. Elsevier, 2003.

[25] J. K. G Dhont. *J. Chem. Phys*, 105:5112, 1996.

[26] R. J. Hunter. *Foundations of Colloid Science*. Oxford University Press, 2nd edition, 2001.

[27] A. Einstein. *Ann. Phys*, 17:549, 1905.

[28] B. M. Kubo. *Science*, 233:330, 1986.

[29] P. Atkins and J. de Paula. *Physical Chemistry*. Oxford University Press, 7th edition, 2002.

[30] B. V. Derjaguin and L. Landau. *Acta Physicochim (URSS)*, 14:633, 1941.

[31] E. J. Verwey and J. Th. G. Overbeek. *Theory of the stability of lyophobic colloids.* Elsevier, Amsterdam, 1948.

[32] S. Asakura and F. Oosawa. *J. Pol. Sci.*, 33:158, 1958.

[33] A. Vrij. *Pure Appl.Chem.*, 48:471, 1976.

[34] A. P. Gast, W. B. Russell, and C. K. Hall. *J. Coll. Inf. Sci*, 96:1977, 1983.

[35] A. P. Gast, W. B. Russell, and C. K. Hall. *J. Coll. Inf. Sci*, 109:161, 1986.

[36] B. Vincent. *Colloids Surf.*, 24:269, 1987.

[37] B. Vincent, J. Edwards, S. Emmett, and R. Croot. *Colloids Surf.*, 31:267, 1988.

[38] H. N. W. Lekkerkerker, W. C. K. Poon, P. N. Pusey, and A. Stroobants. *Europhys. Lett.*, 20:559, 1992.

[39] P. Lu, E. Zaccarelli, F. Ciulla, A. B. Schofield, F. Sciortino, and D. A. Weitz. *Nature*, 453:499, 2008.

[40] T. Eckert and E. Bartsch. *Phys. Rev. Lett.*, 89:125701, 2002.

[41] H. N. W. Lekkerkerker. *Colloids Surf.*, 51:419, 1990.

[42] E. J. Meijer and D. Frenkel. *J. Chem. Phys*, 100:6873, 1994.

[43] A. Moussaïd, W. C. K. Poon, P. N. Pusey, and M. F. Soliva. *Phys. Rev. Lett.*, 82:225, 1999.

[44] M. Fuchs and K. S. Schweizer. *J. Phys.:Condens. Matter*, 14:R239, 2002.

[45] J. S. Rowlinson and B. Widom. *Molecular Theory of Capillarity*. Dover Publications Inc., 1982.

[46] M. V. von Smoluchowski. *Ann. Phys.*, 25:205, 1908.

[47] L. Mandelstam. *Ann. Phys*, 41:609–24, 1913.

[48] E. M. Purcell. *American J. of Phys*, 45:3, 1977.

[49] J. Israelachvili. *Intermolecular and surface forces*. Academic Press, 2nd edition, 1991.

[50] D. G. A. L. Aarts. *The interface in demixed colloid-polymer systems: wetting, waves and droplets.* PhD thesis, 2005.

[51] D. G. A. L. Aarts. *J. Phys. Chem. B*, 109:7407, 2005.

[52] D. Derks, D. G. A. L. Aarts, D. Bonn, and A Imhof. *J. Phys.:Condens. Matter*, 20(20):404208, 2008.

[53] Y. Xia, J. J. McClelland, R. Gupta, D. Qin, X-M. Zhao, L. L. Sohn, R. J. Celotta, and G. M. Whitesides. *Adv. Mater.*, 9:147, 1997.

[54] D. Bartolo, G. Degré, P. Nghe, and V. Struder. *Lab. Chip.*, 8:274, 2007.

[55] A. R. Abate, D. Lee, T. Do, C. Holtze, and D. A. Weitz. *Lab. Chip.*, 8:516, 2008.

[56] E. A. G. Jamie, G. J. Davies, M. D. Howe, R. P. A. Dullens, and D. G. A. L. Aarts. *J Phys.:Condens. Matter*, 20:494231, 2008.

[57] M. D. Howe. *Synthesis of novel polymeric colloidal particles for use in confocal scanning laser microscopy.*, Part II Thesis, 2008.

[58] M. Minsky. *Scanning*, 10:128, 1988.

[59] T. Wilson. *Confocal Microscopy.* Academic Press, 1990.

[60] T. J. Fellers and M. W. Davidson. www.olympusmicro.com, 2010.

[61] R. H. Webb. *Rep. Prog. Phys.*, 59:427, 1996.

[62] E Hecht. *Optics.* Harlow, 3rd edition, 1998.

[63] V. Prasad, D. Semwogerere, and E. R. Weeks. *J Phys.:Condens. Matter*, 19:113102, 2007.

[64] D. Semwogerere and E. R. Weeks. *Encyclopedia of Biomaterials and Biomedical Engineering.* Confocal Microscopy. Taylor and Francis, 2005.

[65] D. R Sandison and W. W. Webb. *Appl. Opt*, 33(4):603, 1994.

[66] A. del Campo and C. Greiner. *J. Micromech. Microeng.*, 17:R81, 2007.

[67] G. M. Whitesides. *Nature*, 442:368, 2006.

[68] Microchem. *SU-8 2000.* Processing Guidelines, 2010.

[69] E. Kumacheva, O. Kalinina, and L. Lilge. *Adv Mater*, 11:231, 1999.

[70] G. Bosma, C. Pathmamanoharan, E. H. A. de Hoog, W. H. Kegel, A. van Blaaderen, and H. N. W. Lekkerkerker. *J. Coll. Inf. Sci*, 245:292, 2002.

[71] G. H. Koenderink, D. G. A. L. Aarts, V. W. A. De Villeneuve, A. P. Philipse, R. Tuiner, and H. N. W. Lekkerkerker. *Biomacromolecules*, 4:129, 2003.

[72] G. H. Koenderink, S. Sacanna, D. G. A. L. Aarts, and A. P. Philipse. *Phys. Rev. E*, 69:021804, 2004.

[73] K. Binder and D. Stauffer. *Phys. Rev. Lett.*, 33:1006, 1974.

[74] I. M. Lifshitz and V. V. Slyozov. *J. Phys. Chem. Solids*, 19:35, 1961.

[75] C. Wagner. *Z. Electrochem*, 65:581, 1961.

[76] A. Onuki. *Europhys. Lett.*, 28:175, 1994.

[77] K. Binder. *Phys. Rev. A*, 29:341, 1985.

[78] E. D. Siggia. *Physical Review A*, 20:595, 1979.

[79] D. Derks, D. G. A. L. Aarts, D. Bonn, H. N. W. Lekkerkerker, and A Imhof. *Phys. Rev. Lett.*, 97:038301, 2006.

[80] S. A. Safran. *Statistical Thermodynamics Of Surfaces, Interfaces, And Membranes (Frontiers in Physics)*. Westview Press, 2003.

[81] D. Derks, D. G. A. L. Aarts, D. Bonn, H. N. W. Lekkerkerker, and A Imhof. *Phys. Rev. Lett.*, 97:038301, 2006.

[82] A. Vrij. *Disscuss. Faraday Soc.*, 42:23, 1966.

[83] V. W. A. de Villeneuve, J. M. J. van Leeuwen, J. W. J. de Folter, D. G. A. L. Aarts, W. van Saarloos, and H. N. W. Lekkerkerker. *Europhys. Lett*, 81:60004, 2008.

[84] U. S. Jeng, L. Esibov, L. Crow, and A. Steyerl. *J. Phys.:Condens. Matter*, 10:4955, 1998.

[85] J. Meunier. *Experimental studies of liquids at interfaces: classical methods for studies of surface tension, surface wave propogation and sturface thermal modes for studies of viscoelasticity and bending elasticity.* Liquids and Interfaces. North-Holland, New York, 1988.

[86] S. Hachisu and K. Takano. *Adv. Colloid Interface Sci.*, 16:233, 1982.

[87] R. Piazza, T. Bellini, and V. Degiorgio. *Phys. Rev. Lett.*, 71:4267, 1993.

[88] H. H. Wensink and H. N. W. Lekkerkerker. *Europhys. Lett.*, 66:125, 2004.

[89] D. van der Beek, T. Schilling, and H. N. W. Lekkerkerker. *J. Chem. Phys.*, 121:11, 2004.

[90] M. Schmidt, M. Dijkstra, and J.P Hansen. *J Phys.:Condens. Matter*, 16:S4185, 2004.

[91] R. Evans. *Adv. Phys*, 28:143, 1979.

[92] D. G. A. L. Aarts, R. P. A. Dullens, H. N. W. Lekkerkerker, D. Bonn, and R. van Roij. *J. Chem. Phys.*, 120:1973, 2004.

[93] E. A. G. Jamie, H. H. Wensink, and D. G. A. L. Aarts. *J. Stat. Mech*, 11:P11008, 2010.

[94] I. Bodnár, J.K.G. Dhont, and H.N.W. Lekkerkerker. Pretransitional phenomena of a colloid polymer mixture studied with static and dynamic light scattering. *J. Phys. Chem.*, 100:19614, 1996.

[95] E. H. A. de Hoog and H. N. W. Lekkerkerker. *J. Phys. Chem. B*, 103:5274, 1999.

[96] B. H. Chen, B. Payandeh, and M. Robert. *Phys. Rev. E*, 62:2369, 2000.

[97] E. Scholten, R. Tuinier, R.H. Tromp, and H.N.W. Lekkerkerker. *Langmuir*, 18:2234, 2002.

[98] F. Lo Verso, R. L. C. Vink, D. Pini, and L. Reatto. *Phys. Rev. E*, 73:061407, 2006.

[99] C. P. Royall, D. G. A. L. Aarts, and H. Tanaka. *Nature Physics*, 3:636, 2007.

[100] M. Dijkstra, J-P. Hansen, and P. A. Madden. *Phys. Rev. Lett.*, 75:2236, 1995.

[101] M. Rasa and A. P. Philipse. *Nature*, 429:857, 2004.

[102] E. A. G. Jamie, H. H. Wensink, and D. G. A. L. Aarts. *Soft Matter*, 6:250, 2010.

[103] S. E. May and J. V. Maher. *Phys. Rev. Lett.*, 67:2013, 1991.

[104] P. Petitjeans. *C. R. Acad. Sci. Paris*, 322:673, 1996.

[105] D. H. Vlad and J. V. Maher. *Phys. Rev. E*, 59:476, 1999.

[106] P. Cicuta, A. Vailati, and M. Giglio. *Phys. Rev. E*, 62:4920, 2000.

[107] R. Tuiner, P. A. Smith, W. C. K. Poon, S. U. Egelhaaf, D. G. A. L. Aarts, H. N. W. Lekkerkerker, and G. U. Fleer. *Europhys. Lett.*, 82:68002, 2008.

[108] D. G. A. L. Aarts, M. Schmidt, H. N. W. Lekkerkerker, and K. R. Mecke. *Adv. Solid State Phys.*, 45:15, 2005.

[109] P. G. de Gennes, F. Brochard-Wyrat, and D. Quéré. *Capillarity and Wetting Phenomena: Drops, Bubbles, Pearls, Waves*. Springer, 2004.

[110] M. R. Moldover, J. V. Sengers, R. W. Gammon, and R. J. Hocken. *Rev. Mod. Phys.*, 51:79, 1979.

[111] J. M. J. van Leeuwen and J. V. Sengers. *Physica A*, 157:839, 1989.

[112] R. L. C. Vink and J. Horbach. *J. Chem. Phys*, 121:3253, 2004.

[113] R. L. C. Vink and J. Horbach. *J Phys.:Condens. Matter*, 16:S3807, 2004.

[114] R. L. C. Vink, J. Horbach, and K. Binder. *Phys. Rev. E*, 71:011401, 2005.

[115] J. Zausch, P. Virnau, K. Binder, J. Horbach, and R. L. C. Vink. *J. Chem. Phys*, 130:064906, 2009.

[116] B. H. Chen, B. Payandeh, and M. Robert. *Phys. Rev. E*, 64:042401, 2001.

[117] U. M. B. Marconi and P. Tarazona. *J. Chem. Phys*, 110:8032, 1999.

[118] A. J. Archer and R. Evans. *J. Chem. Phys*, 21:4246, 2004.

[119] A. J. Bray. *Coarsening dynamics of nonequilibrium phase transitions.* Soft and Fragile Matter: Nonequilibrium Dynamics, Metastability and Flow. SUSSP Publications, Instituite of Physics Publishing, 2000.

[120] P. Guenoun, P. Gastaud, F. Perrot, and D. Beysens. *Phys. Rev. A*, 36:10, 1987.

[121] J. W. Cahn. *Transactions Metallurgical Society AIME*, 242:166, 1968.

[122] J. E. Hilliard. Phase transformations, 1970.

[123] A Wysocki, C. Räth, A.V. Ivlev, K. R. Sutterlin, H. M. Thomas, S. Kharpak, S. Zhdanov, V. E. Fortov, A. M. Lipaev, V. I. Molotkov, O. F. Petrov, H. Löwen, and G. E. Morfill. *Phys. Rev. Lett.*, 105:045001, 2010.

[124] H. Tanaka. *J. Phys.:Condens. Matter*, 12:207, 2000.

[125] T Hashimoto, T Koga, H Jinnia, and Y Nishikawa. *Il nuovo cimento*, 20:1947, 1998.

[126] E. H. A. de Hoog and H. A. Tromp. *Colloids and Surfaces A: Physicochem. Eng. Aspects*, 213:221, 2002.

[127] N. A. M. Verhaegh, J. S. van Duijneveldt, J. K. Dhont, and H. N. W. Lekkerkerker. *Physica A*, 230:409, 1996.

[128] S. Bhat, R. Tuiner, and P. Schurtenberger. *J Phys.:Condens. Matter*, 18(26):L339, 2006.

[129] G. J. Fleer and R. Tuinier. *Adv. Colloid Interface Sci.*, 143:1, 2008.

[130] J. W. Cahn and J. E. Hilliard. *J. Chem. Phys*, 28:258, 1958.

[131] I. Pagonabarraga, J-C. Desplat, A. J. Wagner, and M. E. Cates. *New. J. Phys*, 3:9, 2001.

[132] J. W. Cahn. *J. Chem. Phys.*, 42:93, 1965.

[133] S. Chandrasekhar. *Hydrodynamic and hydromagnetic stability.* Dover, 1981.

[134] A. Wysocki and H. Löwen. *J. Phys.:Condens. Matter*, 16:7209, 2004.

[135] Dow Corning. http://www.dow.com/glycerine/resources/physicalprop.htm.

[136] R. P. A. Dullens, E. A. Claesson, and W. K. Kegel. *Langmuir*, 20:658, 2004.

[137] H. Furukawa. *Physica A*, 123:497, 1983.

[138] A. E. Bailey, W. C. K. Poon, R. J. Christainson, A. B. Scholfield, U. Gasser, V. Prasad, S. Manley, P. N. Segre, L. Cipelletti, W. V. Meyer, M. P. Doherty, S. Sankaran, A. L. Jankovsky, W. L. Shiley, J. P. Bowen, J. C. Eggers, C. Kurta, T. Lorik. Jr, P. N. Pusey, and D. A. Weitz. *Phys. Rev. Lett.*, 99:205701, 2007.

[139] C. Houessou, P. Guenoun, R. Gastaud, F. Perrot, and D. Beysens. *Phys. Rev. A*, 32:1818, 1985.

[140] P. Guenoun, R. Gastaud, F. Perrot, and D. Beysens. *Phys. Rev. A*, 36:4876, 1987.

[141] D. Beysens, P. Guenoun, and F. Perrot. *Phys. Rev. A*, 38:4173, 1988.

[142] Y. Hennequin, D. G. A. L. Aarts, J. O. Indekeu, H. N. W. Lekkerkerker, and D. Bonn. *Phys. Rev. Lett.*, 100:178305, 2008.

[143] J. S. Rowlinson and B. Widom. *Molecular Theory of Capillarity*. Dover Publications Inc., p122, 1982.

[144] R. C. Ball and R. L. H. Essery. *J Phys.:Condens. Matter*, 2:10303, 1990.

[145] R. A. L. Jones, L. J. Norton, E. J. Kramer, F. S. Bates, and P. Wiltzuis. *Phys. Rev. Lett.*, 66:1326, 1991.

[146] G. Brown and A. Chakrabarti. *Phys. Rev. A*, 46:4829, 1992.

[147] S. Puri and K. Binder. *Phys. Rev. E*, 49:5359, 1994.

[148] F. Schmid and R. Blossey. *J. Phys. II France*, 4:1195, 1994.

[149] M. Geoghegan and G. Krausch. *Prog. Polym. Sci*, 28:261, 2003.

[150] S. Puri. *J. Phys.:Condens. Matter*, 17:R101, 2005.

[151] G. Krausch, C-A Dai, E. J. Kramer, and F. S. Bates. *Phys. Rev. Lett.*, 71:3669, 1993.

[152] S. Puri and K. Binder. *Phys. Rev. A*, 46:4487, 1992.

[153] J. F. Marko. *Phys. Rev. E.*, 48:2861, 1993.

[154] M. Geoghegan, T. Nicolai, J. Penforld, and R. A. L. Jones. *Macromolecules*, 30:4220, 1997.

[155] H. Tanaka and T. Araki. *Europhys. Lett.*, 51:154, 2000.

[156] W. Straub, F. Bruder, R. Brenn, G. Krausch, H. Bielefeldt, A. Kirsch, O. Marti, J. L. Mlynek, and J. F. Marko. *Europhys. Lett.*, 29:353, 1995.

[157] L-T. Yan and X-M. Xie. *Macromolecules*, 39:2388, 2006.

[158] S. Puri and K. Binder. *Phys. Rev. E*, 66:061602, 2002.

[159] L-T. Yan and X-M. Xie. *J. Chem. Phys*, 126:064908, 2007.

[160] S. Puri and K. Binder. *Phys. Rev. Lett.*, 86:1797, 2001.

[161] M. Geoghegan, H. Ermer, G. Jüngst, G. Krausch, and R. Brenn. *Phys. Rev. E*, 62:940, 2000.

[162] L-T. Yan and X-M. Xie. *Polymer*, 47:6472, 2006.

[163] S. Puri and K. Binder. *Phys. Rev. E*, 49:6, 1993.

[164] L-T. Yan and X-M. Xie. *Polymer*, 46:7684, 2005.

[165] U. Steiner and J. Klien. *Phys. Rev. Lett.*, 77:2526, 1996.

[166] H. Tanaka. *Phys. Rev. Lett.*, 70:2770, 1993.

[167] H. Tanaka. *Phys. Rev. E*, 54:1709, 1996.

[168] P. Guenoun, D. Beysens, and M. Robert. *Physica A*, 172:137, 1991.

[169] P. Wiltzuis and A. Cumming. *Phys. Rev. Lett.*, 66:3000, 1991.

[170] P. K. Jaiswal, S. Puri, and S. K. Das. *Archive*, 2011.

[171] G. Brown, A. Chakrabarti, and J. F. Marko. *Phys. Rev. E*, 50:1674, 1994.

[172] S. Hell, G. Reiner, C. Cremer, and E. H. K. Stelzer. *Journal of Microscopy*, 169:391, 1993.

[173] A. Cumming, P. Wiltzuis, F. S. Bates, and J. H. Rosedale. *Physical Review A*, 45:885, 1992.

[174] B. Q. Shi, C. Harrison, and A. Cumming. *Phys. Rev. Lett.*, 70:206, 1993.

[175] H. K. Pak and B. M. Law. *Europhys. Lett.*, 31:19, 1995.

[176] J. O. Indekeu, D. G. A. L. Aarts, Y. Hennequin, H. N. W. Lekkerkerker, and D. Bonn. *Phys. Rev. E.*, 81:041604, 2010.

[177] K. Binder. *Ann. Rev. Phys. Chem.*, 42:33, 1992.

[178] K. Binder, S. Puri, S. K. Das, and J. Horbach. *J. Stat. Phys.*, 138:51, 2010.

[179] C. Gögelein, M. Brinkmann, M. Schröter, and S. Herminghaus. *Langmuir*, 26:17184, 2010.

[180] A. De Virgiliis, R. L. C. Vink, J. Horbach, and K. Binder. *Europhys. Lett.*, 77:60002, 2007.

[181] H. Tanaka. *Europhys. Lett.*, 24:665, 1993.

[182] L. D. Gelb, K. E. Gubbins, R. Radhakrishnan, and M Sliwinska-Bartowiak. *Rep. Prog. Phys.*, 62:1573, 1999.

[183] T. S. Squires and S. R. Quake. *Rev. Mod. Phys.*, 77:977, 2005.

[184] J. Wang, A. Ibáñez, and M. P. Chatrathi. *J. Am. Chem. Soc.*, 125:8444, 2003.

[185] N. Pamme. *Lab. Chip.*, 7:1644, 2007.

[186] S-Y. The, R. Lin, L-H. Hung, and A. P. Lee. *Lab. Chip.*, 8:198, 2007.

[187] O. Castell, C. J. Allender, and D. A. Barrow. *Lab. Chip.*, 9:388, 2008.

[188] K. F. Jensen. *Chem. Eng. Sci*, 56:293, 2001.

[189] R. L. C. Vink, A. De Virgiliis, J. Horbach, and K. Binder. *Phys. Rev. E*, 74:031601, 2006.

[190] G. Krausch, C-A. Dai, E. J. Kramer, J. F. Marko, and F. S. Bates. *Macromolecules*, 26:5566, 1993.

[191] M. Geoghegan, R. A. L. Jones, and A. S. Clough. *J. Chem. Phys*, 103:2719, 1995.

[192] F. Bruder and R. Brenn. *Phys. Rev. Lett.*, 69:624, 1992.

[193] H. Tanaka. *J. Phys.:Condens. Matter*, 13:4637, 2001.

[194] J. Bodensohn and W. I. Goldberg. *Phys. Rev. A*, 46:5084, 1992.

[195] B.J. Frisken, F. Ferri, and D.S. Cannell. *Phys. Rev. Lett.*, 66:2754, 1991.

[196] K. Binder, J. Horbach, R. L. C. Vink, and A. De Virgiliis. *Soft Matter*, 4:1555, 2008.

[197] S. K. Das, S. Puri, J. Horbach, and K. Binder. *Phys. Rev. E*, 72:061603, 2005.

[198] T. Ohta. *Ann. Phys. NY*, 158:31, 1984.

[199] H. Tanaka. *J. Chem. Phys*, 105:10099, 1996.

[200] V. Kumaran. *J. Chem. Phys*, 112:10984, 2000.

[201] H. Wang and R. J. Composto. *J. Chem. Phys.*, 113:10386, 2000.

[202] J. H. J. Thijssen and P. S. Clegg. *J. Phys.:Condens. Matter*, 22:455102, 2010.

[203] W. S. Rasband. Imagej, 1997-2009.

[204] M. D. Abramoff, P.J. Magelhaes, and S.J. Ram. Image processing with imagej. *Biophotonics International*, 11:36, 2004.

[205] A. O. Parry and C. Rascon. *Nature*, 407:986, 2004.

List of publications

To date the following publications have been submitted based upon the work in this thesis:

E. A. G. Jamie, G. J. Davies, M. D. Howe, R. P. A. Dullens, D. G. A. L. Aarts, *Thermal capillary waves in colloid-polymer mixtures in water*, J. Phys.: Condens. Matter, **20** 494231 (2008). (Chapter 2).

E. A. G. Jamie, H. H. Wensink, D. G. A. L. Aarts, *Probing the critical behavior of colloidal interfaces by gravity*, Soft Matter, **6** 250 (2010). (Chapter 3).

E. A. G. Jamie, H. H. Wensink, D. G. A. L. Aarts, *Sedimentation-diffusion dynamics in colloid-polymer mixtures*, J. Stat. Mech, **11** P11008. (Chapter 4).

E. A. G. Jamie, R. P. A. Dullens, D. G. A. L. Aarts, *Tuning the demixing of colloid-polymer systems through the dispersing solvent*, J. Phys.: Condens. Matter, **23** 194115 (2011). (Chapter 5).

E. A. G. Jamie, R. P. A. Dullens, D. G. A. L. Aarts, *Surface effects on the demixing of colloid-polymer systems*, J. Phys. Chem. B, Submitted. (Chapter 6).

E. A. G. Jamie, R. P. A. Dullens, D. G. A. L. Aarts, *Spinodal decomposition of a confined colloid-polymer system*, Submitted. (Chapter 7).

E. A. G. Jamie, R. P. A. Dullens, D. G. A. L. Aarts, *Phase separation of off-critical colloid-polymer mixtures*, J. Phys.: Condens. Matter, Submitted. (Chapter 7).

Acknowledgements

I would like to thank Dirk for all his help and ideas in the last 3.5 years (exactly, with no spare minutes), and Roel for his extra encouragement. I'd like to thank all the past and present members of the Aarts and Dullens groups for their scientific assistance but mostly for making the last few years so much fun. Sam for being an amazing proof reader, but also providing the first female voice of reason in the upstairs office and (at least) 12 glasses of wine. Tom for not being too scathing of my writing ability, and putting up with me through some very stressed talks, and May Day type situations. Oli for keeping my productivity upstairs always low, and my chair never dry. Mike for being my lunch secretary, and understanding the need for headphones. Min, Paola (for the sofa especially), Alice, Julia (best figure spot ever), Harry, Ellie, Seb, Nina for the PTCL parties, cakes and various lab socials. Adam, Adam and Fenix,(and Oli) your part II year was definitely memorable. Michael and Gareth for being there right at the beginning when the lab was empty. Lastly I especially thank Ellie, Vanessa, Sam, Sandra and my parents for all their support in the last few months, and making sure that Harold didn't get to me too much.